TUM School of Natural Sciences

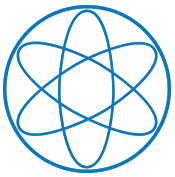

Fakultät für Physik

Master's Thesis

Characterizing the Particle Emitting Source in pp Collisions at 13.6 TeV with ALICE: Insights from p–p and p–Λ Correlations

Jaime González González

TECHNISCHE UNIVERSITÄT MÜNCHEN

TUM School of Natural Sciences

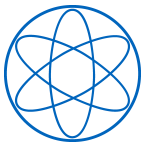

Fakultät für Physik

Characterizing the Particle Emitting Source in pp Collisions at 13.6 TeV with ALICE: Insights from p–p and p–Λ Correlations

Charakterisierung der Teilchenemissionsquelle in pp Kollisionen bei 13,6 TeV mit ALICE: Erkenntnisse aus p–p und p–Λ Korrelationen.

Master's Thesis

Author: Jaime González González
Supervisor: Prof. Dr. Laura Fabbietti
Advisor: Anton Riedel

Date: 04.08.2025

I confirm that the results presented in this master's thesis is my own work and I have documented all sources and materials used.

Ich versichere, dass ich diese Masterarbeit selbstständig verfasst und nur die angegebenen Quellen und Hilfsmittel verwendet habe.

Munich, 04.08.2025 Jaime González González

Abstract

This work presents a study of particle correlations with the formalism of femtoscopy. Within this field the kinematic geometries of the emission source of particles in a collider event can be interpreted by means of studying the characteristics of two-particle correlations, thereby providing insight into the underlying forces that dictate the space-time evolution of the system. Furthermore, this method offers greater access to unstable hadrons less accessible by traditional scattering experiments, such as hyperons.

Previous studies of the source with high-multiplicity data taken in the second operational run (2015–2018) of the Large Hadron Collider (LHC) concluded in a common baryonic source from which primordial particles are emitted. The foundation of which was laid by correlations between proton-proton (p–p) and proton-lambda (p–Λ) pairs. This finding was subsequently endorsed by further studies with a plethora of particle pairs, ranging from mesons to hyperons.

The aim of this thesis is to further investigate the common source with the newly acquired data from the third run of the LHC. During the Long Shutdown 2 of the LHC several upgrades to its systems were introduced that now offer unprecedented high luminosity capabilities and unmatched counts of events. Accordingly, a first of its time multi-differential analysis in transverse mass (m_{T}) and multiplicity of the source is presented for the systems of p–p and p–Λ pairs. Additionally, a comparison with different potentials for the p–p interaction is provided to set a precedent for future studies.

Contents

1 Introduction

One of the main ambitions of high-energy particle physics is to understand the behaviour of strongly interacting matter under conditions of extreme temperatures and densities. Heavy-ion collisions at accelerators like the Large Hadron Collider (LHC) and the Relativistic Heavy Ion Collider (RHIC) provide adequate conditions to produce quark-gluon plasma (QGP), a phase of deconfined quarks and gluons that is thought to have existed microseconds after the Big Bang. However, as the QGP and its dynamics cannot be directly observed, experimental physicists are forced to use indirect probes that are able to reconstruct data regarding its space-time evolution on a femtometer (10^{-15} m) scale.

Femtoscopy is the study of the space-time geometries relevant to the particle-emitting source through two-particle correlations at small relative momenta, thus offering a femtometer-scale viewpoint to assess the final moments of the evolution of the system before freeze-out. This is a direct application of photon intensity interferometry in particle physics, where quantum statistical correlations are employed for indistinguishable particles created in high-energy collisions. The use of femtoscopy allows access to important constraints regarding the system size, time duration, expansion dynamics, and collective properties of the created system. This, in turn, provides immediate input to the equation of state (EoS) for strongly interacting matter.

Femtoscopy is based on the Hanbury Brown–Twiss effect, initially used in astronomical applications for the determination of the angular diameters of stars by the study of intensity correlations between photons measured by two independent receivers [1]. The main discovery was that quantum statistical correlations between indistinguishable bosons lead to an enhancement of the measured correlation function at low relative momentum, which is inherently connected with the spatial sizes of the emitting source.

In the late 1950s and early 1960s, Gerson Goldhaber, Sulamith Goldhaber, Won-Yong Lee, and Abraham Pais used an analogous method to examine pions produced in high-energy proton-proton (pp) collisions [2]. They observed an enhancement in the production of identical pions at low relative momenta, which they interpreted as an interference effect due to the symmetry in the wave function and showed that identical pions are subject to Bose-Einstein correlations. Furthermore, they presumed that those might be connected to the space-time separation of the origin of emission. However, the theoretical framework was not complete then, and experimental resolution constrained the extraction of precise spatial sizes.

It was only after the 1980s that the rise of relativistic heavy-ion experiments made the potential of studying hot and dense matter a reality, thus opening the door to examining the formation and evolution of QGP. In this context, femtoscopy allowed to inquire and compare these measurements with transport and hydrodynamic models, which subsequently unlocked a possible path to help understand and constrain the EoS.

Eventually, with the advent of the LHC and RHIC enough precision was achieved to provide evidence for strong collective flow in heavy-ion collisions [3]. The culmination of effort such as these is the phase diagram for matter bound by the laws of QCD, as shown in figure 1.1, where the temperature is plotted against the baryon density and the phases are separated by the transition boundaries.

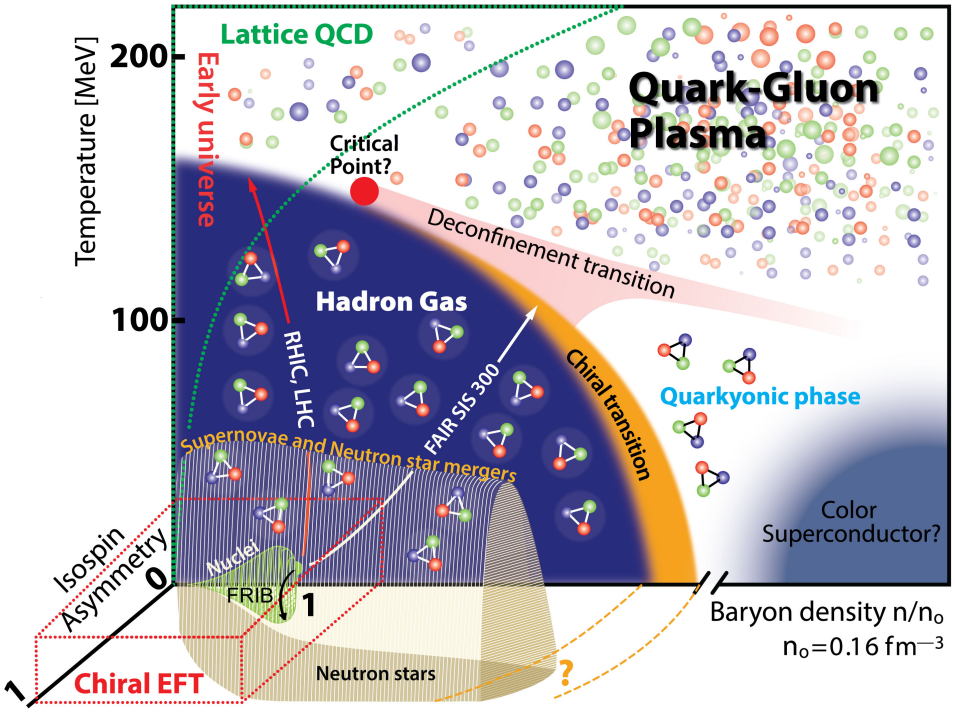

Figure 1.1: Schematic representation of the QCD phase diagram, taken from [4].

One of the constituents in the realm of extremely dense matter are neutrons stars, the remnants of the collapsed core of a supergiant stars that are riddled with many open questions. Recent measurements of their masses have shown an upper limit exceeding two solar masses [5, 6]. However, theoretical calculations are in conflict with these values as the densities reached by such neutron stars far exceed the required to produce hyperons [7]. The existence of which softens the EoS, i.e. reduces the pressure excluded by the given density, as they act as a further degree of freedom and reduce the number of neutrons, consequently diminishing the Fermi pressure exerted by close indistinguishable particles. Thus, their presence makes such masses unviable; this is known as the hyperon puzzle.

From Stars to Particles

Modern femtoscopy offers an alternative experimental approach to solve the puzzle to the conventional adjusting of effective theoretical models. One of the proposed solutions for it is by reevaluating the interactions of nucleons and hyperons in dense

matter, as for example a repulsive hyperonic three-body interaction could help stiffen the EoS. To this end, the accurate description of two-body forces is a must.

In recent times, measurements from small collision systems, such as pp collisions from the first and second data-taking periods of the LHC, have been used to undertake this ordeal by means of profiling the particle-emitting source, as the production mechanism for particles is expected to be similar between species. The simpler pp system offers the platform to evaluate the correlations between individual particles without pollution from collective effects seen in heavy-ion collisions. Additionally, the reduced size of the system provides an increased sensitivity to smaller-range forces acting on the emitted particles. These attributes were used in the analysis of proton-proton (p–p), proton-lambda (p–Λ) and lambda-lambda (Λ–Λ) pairs with the ALICE detector at the LHC to study the correlations between the particles at an energy of $\sqrt{s} = 7\,\text{TeV}$ during the first run [8]. The second run presented the opportunity to study the interactions in high-multiplicity events at an energy of $\sqrt{s} = 13\,\text{TeV}$ and resulted in measurements of the particle emitting source as a function of the transverse mass, defined as

$$m_{\text{T}} = \sqrt{k_{\text{T}}^2 + \overline{m}^2}\,, \tag{1.1}$$

where $\overline{m}$ is the average mass and k_{T} the average transverse momentum of the particle pair [9]. The collection of values were perceived as a scaling in m_{T}, which is typically attributed to the collective expansion of the system. Furthermore, the comparison of the different pairs and the consideration of their origin, i.e. primordial particles or decays from resonances for example, delivered evidence for a common particle emitting source. Following this hypothesis various other systems were studied to further strengthen its validity [10]. Further improvements were proposed by studying the multiplicity dependence and characteristics of the source.

This analysis aims to bridge the gap with the newly acquired data in the third data-taking run of the LHC by the upgraded ALICE detector. The unprecedented number of collected events surpassing the 500 billion mark at an energy of $\sqrt{s} = 13\,\text{TeV}$ offers for the first time the precision and statistics to investigate the particle-emitting source and its size in a multi-differential environment. In this analysis the method of reconstruction and event selection to partitioning of the data in multiplicity percentiles and m_{T} intervals will be shown. Subsequently, the processed data will be used to obtain a measurement of the source for p–p, $\overline{\text{p}}$–$\overline{\text{p}}$ and p–Λ, $\overline{\text{p}}$–$\overline{\Lambda}$ pairs. Additionally, the size for the p–p and $\overline{\text{p}}$–$\overline{\text{p}}$ correlations will be compared to those obtained by modelling the interaction with different potentials. Finally, the extent of the primordial source will be reported.

2 Femtoscopy

Inspired by intensity interferometry observations in astronomy, femtoscopy aims to relate correlations from measured particles to their origin. To this end, the correlation function is used as an observable, since it represents the most direct link to the pairwise particle correlations. This follows as a consequence of its definition as the ratio of the two-particle to the single-particle inclusive spectra

$$C(\mathbf{p}_1, \mathbf{p}_2) = \frac{P(\mathbf{p}_1, \mathbf{p}_2)}{P(\mathbf{p}_1)P(\mathbf{p}_2)} = \frac{E_1 E_2 dN/d^3p_1 d^3p_2}{(E_1 dN/d^3p_1)(E_2 dN/d^3p_2)}, \tag{2.1}$$

where in absence of any correlations, the probability $P(\mathbf{p}_1, \mathbf{p}_2)$ of finding a particle with momentum $\mathbf{p}_1$ and a second with $\mathbf{p}_2$ in a collision should be equal to the individual probabilities, $P(\mathbf{p}_1)$ and $P(\mathbf{p}_2)$, independent of their origin [11].

This however is not the case due to final state interactions that occur after the freeze-out of a collision is reached. Attractive forces between particles result in an increased likelihood of finding pairs closer in phase-space, while a repulsive interaction decreases it. Consequently, an enhancement or depletion in the two-particle spectra will be present, respectively, which translates to a ratio above or below unity.

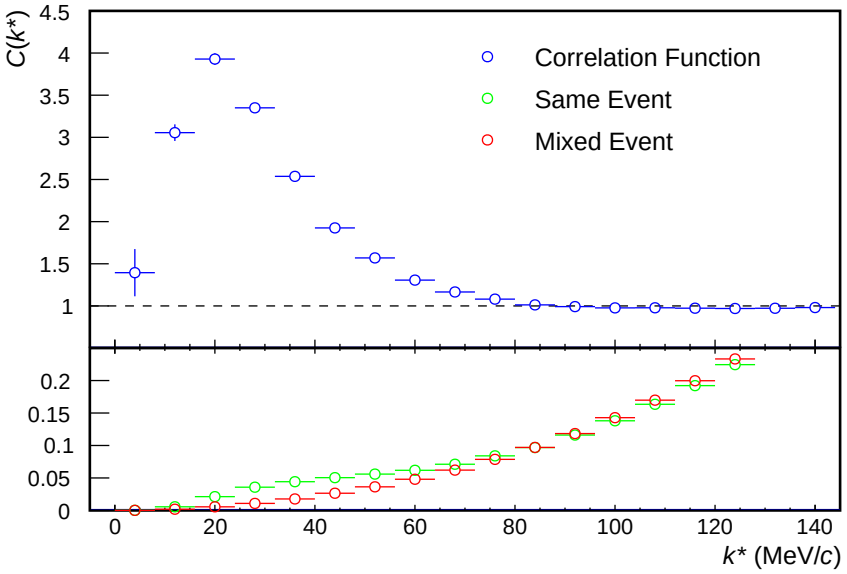

Figure 2.1: Example correlation function resulting from the ratio of the shown normalized same event and mixed event distributions of proton pairs.

The correlated signal is experimentally obtained by directly taking the distribution

of relative momentum, $k^* = \frac{1}{2}|\mathbf{p}_1 - \mathbf{p}_2|$, of particle pairs from a single event, while the uncorrelated signal has to be generated by applying event mixing techniques; the idea being that particles stemming from different events should not be correlated. Thus, the correlation function reads

$$C_{\text{exp}}(k^*) = \mathcal{N} \cdot \frac{N_{\text{same}}(k^*)}{N_{\text{mixed}}(k^*)}, \tag{2.2}$$

for which the additional factor $\mathcal{N}$ is introduced to normalize the function in a regime where no femtoscopic signal is expected; this usually is the case above 200 MeV/c. Unfortunately, care must be taken for the long range regime, as non-femtoscopic correlations contribute to spurious effects and drive the correlation function away from unity; therefore, a restriction of the normalization region is necessary.

As an example, figure 2.1 shows the normalized same event and mixed event distributions for proton pairs in the femtoscopic region of interest, and the resulting correlation function. In this case, there is an enhancement of the same event distribution in the low k^* region, due to the strong force, that translates into a very pronounced peak.

2.1 Theoretical Correlation Function

In order to associate the experimentally available data to the governing underlying forces, ample work has been performed on the theory side over the past decades. The culmination of which is the Koonin-Pratt equation

$$C(k^*) = \int d^3r^* S(\boldsymbol{r}^*)|\psi_{k^*}(\boldsymbol{r}^*)|^2, \tag{2.3}$$

which forms the basis of most femtoscopic analyses [11]. In a nutshell, it links the interaction between particle pairs to the spatiotemporal geometry of the collision. This is achieved through the combination of two components: the two-particle wave function $\psi_{k^*}(\mathbf{r}^*)$, which obviously incorporates the potential between the pair of constituent particles, and thus the interaction; and the two-body emission source function $S(\mathbf{r}^*)$, or commonly the source, which intends to parameterize the shape of the region of homogeneity from where particle with specific momenta are emitted.

Originally, the source function came to existence in an approximation of the two-proton inclusive cross-section that was split into the scattering wave functions multiplied by two space and time dependent distributions for the single particle spectra [13]. The two distributions were then combined to yield the two-body source function whose parameterization was akin to a gaussian profile, and as such, later assimilated in heavy-ion collisions to model the larger sources with space and time dependencies [11]. The function was thus comprised of

$$\mathcal{S}_{\mathbf{P}}(\mathbf{r}') \sim \exp\left\{-\frac{[r'_{\text{out}} - \bar{X}_{\text{out}}]^2}{4\gamma_\perp^2 R_{\text{out}}^2} - \frac{r'^2_{\text{side}}}{4R_{\text{side}}^2} - \frac{r'^2_{\text{long}}}{4R_{\text{long}}^2}\right\},$$

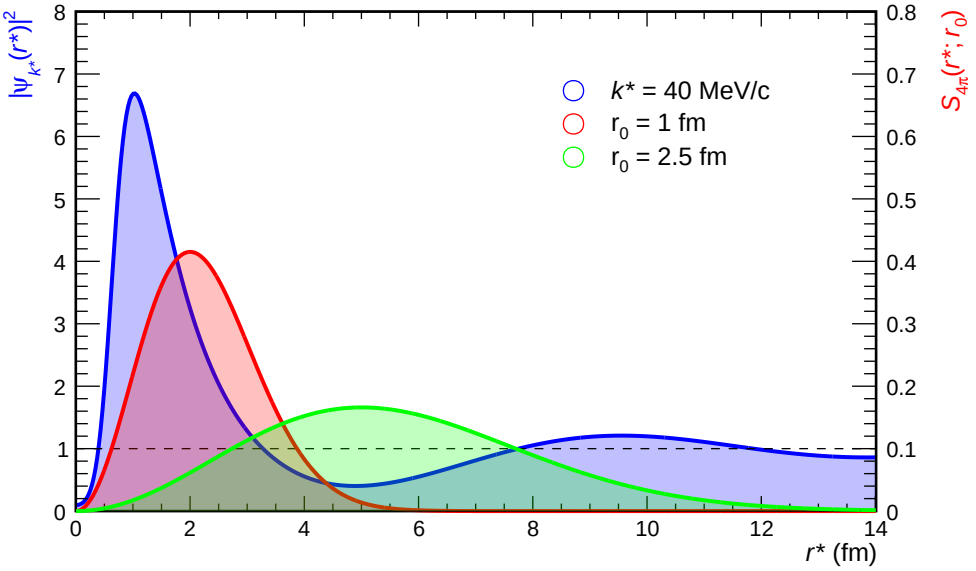

Figure 2.2: Example square of two-proton wave function for $k^* = 40$ MeV/c, modeled with the AV18 potential [12]; and two source functions $S_{4\pi}(r^*;\ r_0)$ of sizes $r_0 = 1$ fm and 2.5 fm, the scale of whom is drawn on the right side.

for which the out-side-long frame of reference is favoured: the longitudinal axis is defined by the beam direction; the outwards by the perpendicular direction of the momentum of the pair; the sideward by the axis perpendicular to the previous two. The main point of this function is its R_x parameters that can be thought of defining the axes of an ellipsoid. Fortunately, for smaller sources the assumption of isotropic emission can be made due to the fast freeze-out of the region of homogeneity. As a consequence, the function simplifies to a more accessible gaussian

$$S(\boldsymbol{r}^*;\ r_0) = \frac{1}{(4\pi r_0^2)^{3/2}}\ \exp\left(-\frac{\boldsymbol{r}^{*2}}{4r_0^2}\right) \tag{2.4}$$

with its width r_0, commonly referred to as the radius, as the sole parameter. A further dimensional reduction occurs due to the radial symmetry of the function; the integration over the angular part in the correlation function yields $4\pi r^{*2}$ and can be incorporated into one of the constituents. Thus, the source function becomes

$$S_{4\pi}(r^*;\ r_0) = \frac{4\pi r^{*2}}{(4\pi r_0^2)^{3/2}}\ \exp\left(-\frac{r^{*2}}{4r_0^2}\right). \tag{2.5}$$

In this case, the parameter r_0 acquires a new side effect compared to the width of a default gaussian distribution; increasing its value does not only broaden the distribution but also shift its mean to larger values. This behavior is illustrated in figure 2.2 where two source functions of widths 1 fm (red) and 2.5 fm (green) are superimposed with the square of a two-particle wave function (blue).

2.2 The Two-Particle Interaction

Returning to the Koonin-Pratt equation, the connection to the underlying physics is provided by the two-body interaction wave function. As such, it is of great importance to understand its meaning in the relation. Its dependency on not only space, through the relative distance r^*, but also momentum, through k^*, might seem contradictory to ordinary quantum mechanics; yet the answer lies in the Schrödinger equation and the classical kinetic energy $E_k = \frac{1}{2}mv^2 = \frac{p^2}{2m}$, which are linked through the de Broglie relations of matter waves. The momentum of a free particle of mass m is accordingly given by

$$p^2 = 2mE_k,$$

with which the relative momentum of two particles can easily be obtained. Therefore, the momentum dependence of the wave function should be understood as the energy between the two particles after the final state interactions have taken place. Consequently, the square of the two-particle wave function as the probability to find a pair with distance r^* for any given energy in the continuum.

2.3 The Source Function

The last hurdle to overcome is understanding the meaning and effect of the source on the correlation function. To this end, it is convenient to think about the convolution of the two elements. For proton collisions the region of homogeneity, and thus the size of the source, is in the range of 1-2 fm and small compared to heavy ion collisions, where the size is around 10 fm. This difference is imprinted into the characteristics of the particle emission, as the larger size equals a larger area from where particles can originate. Consequently, the probability of finding close pairs in phase-space decreases and the contribution of the short ranged strong force is smaller. It is for this reason that the source acquires the meaning of a probability density function, as it represents the likelihood to find pairs of particles with a specific relative distance for a given spatial configuration.

Taking figure 2.2 as a reference, the smaller source (red), i.e. the distribution with the smaller radius r_0, is much more localized and encompasses a larger area of the squared two-proton wave function; while the broader (green) source covers with its shifted mean a less populated region. This translates to a bigger or smaller contribution to the correlation function; therefore, allowing the probing of the interaction for longer or shorter ranged forces by means of adjusting the size of the source.

2.4 Features of the Correlation Function

On a final note, the correlation function is very sensitive to different effects of the dynamics and the composition of the particles observed. The raw, unfiltered $C(k^*)$ obtained from measurements is a mixture of the primordial particles, originating from the event, and those stemming from decays; referred to as feed-down. For example, protons can originate from the collision itself or result from the weak decay

of a Λ (uds) into a proton (uud) and a π^- ($\mathrm{d\bar{u}}$). A more in depth analysis of these contributions is provided in chapter 5. Additionally, for proton pairs, i.e. identical and indistinguishable particles, another effect that has to be taken into consideration is that of the symmetrization of the wave function. In terms of the two-body wave function, some channels might not be accessible due to this constrain.

A further effect that might have an impact, albeit not for proton pairs, is that of coupled-channel dynamics; this plays a role in the analysis of proton-lambda (p–Λ) pairs. When a system shares the same quantum numbers as another, its wave function is no longer an independent solution of the Schrödinger equation and can thus transition, as given by quantum mechanics, into each other. This coupling results in an enhancement, a cusp, in the correlation function at the point where the external system has enough energy to transition into the particles of interest. This behaviour can be observed in chapter 7 where fits of the p–Λ correlation function are shown. The cusp appears at around 290 MeV/c, where the Λ (uds, isospin 0) couples to Σ^0 (uds, isospin 1).

3 Experimental Setup

The Large Hadron Collider, known globally as the LHC, is to date the largest and most powerful particle accelerator in the world. Situated over 100 m beneath Geneva in the 27 km long tunnel from its predecessor, the Large Electron-Positron Collider (LEP), it reaches collision energies up to 13.6 TeV; more than enough to dissolve the boundaries of matter. Around its circumference four major experiments can be found: ATLAS, CMS, ALICE, and LHCb; each of which is located at one of the four interaction points. It is at these points were bunches of protons or heavy ions, such as lead nuclei, are made to collide. In the case of the later, the exotic state of matter known as QGP, were quarks and gluons are deconfined, can be created and studied, for example, in A Large Ion Collider Experiment (ALICE).

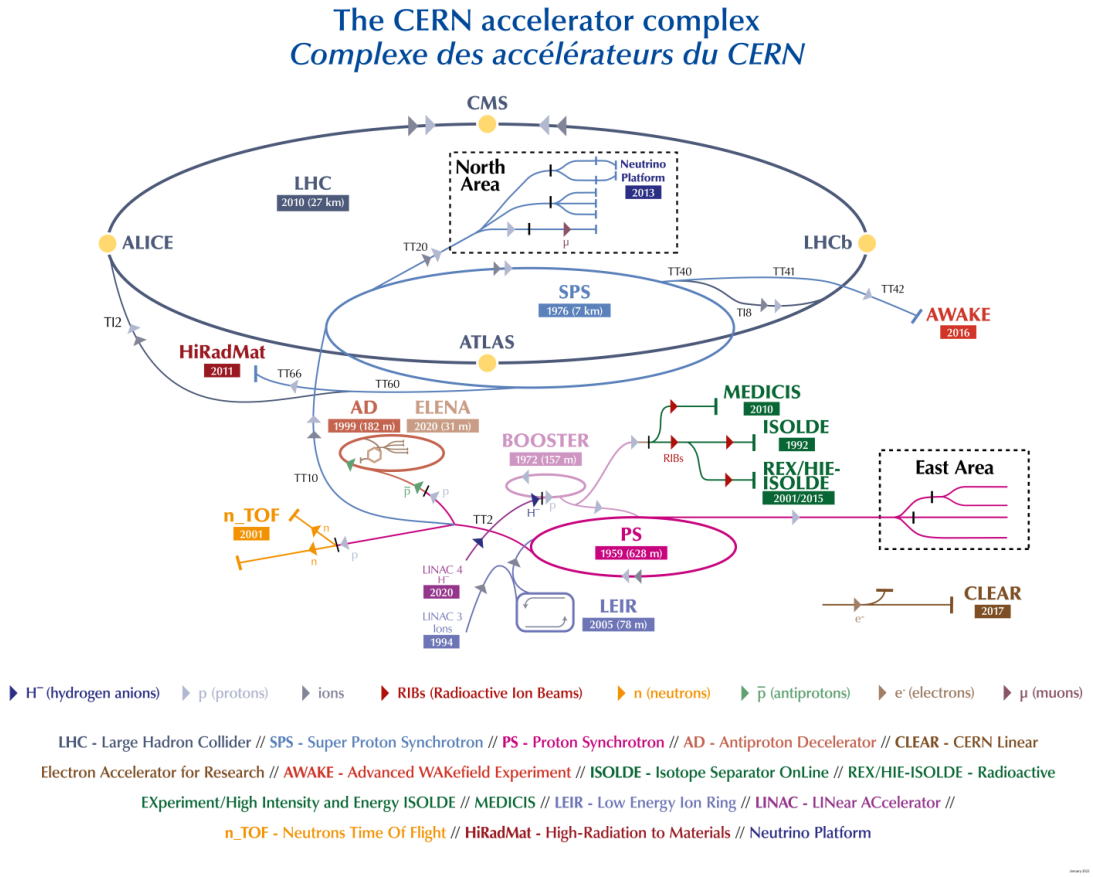

Figure 3.1: The CERN complex, taken from [14].

The LHC underwent a big upgrade during the Long Shutdown 2 (2019-2022) were

all experiments improved their capabilities to comply with the higher luminosity aspirations of its planned third data taking period, which successfully began on July of 2022 and is planed to last until 2026.

In the following sections an overview of the ALICE detector and a detailed description of the more important subsystems needed for this analysis is provided, both of which heavily rely on the following references for details [15, 16].

3.1 ALICE Detector

A Large Ion Collider Experiment is one of the four major experiments located at CERN and focuses on heavy-ions, matter at extreme temperatures, and more generally, physics of strongly interacting matter. To this end, the detector specializes on Particle IDentification (PID) which is an essential requirement for many of the observables, as they tend to depend on the mass or flavour. Despite the vast amount of particles in the order of 10000 created in heavy-ion collisions, this goal is achieved and reflected in the layout and construction of the experiment, which can be found in the schematic representation in figure 3.2.

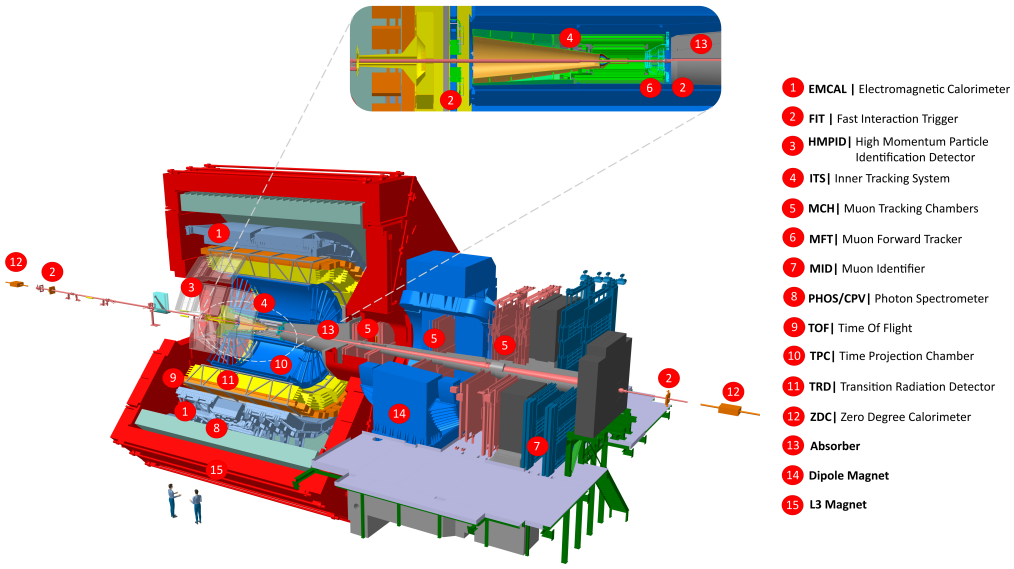

Figure 3.2: The ALICE 2 detector, taken from [16].

The core of the detector is comprised of the central barrel detector system; a cylindrical structure housing high precision instruments to track particles and assess the origin of the collision. Particles emitted from the collision point, the primary vertex, first encounter in transversal direction the Inner Tracking System (ITS), which was purpose

build to determine not only the primary but also reconstruct secondary vertices from the decays of hyperons and other particles. Tracks measured in the ITS are extrapolated to their origin and can later be matched with the succeeding layers for increased precision. Longitudinally, the muon forward tracker is found, which assists the outer tracking chambers extending the capabilities of muon spectrometry. To accomplish the goal of particle identification, the former L3 experiment magnet of the LEP collider envelops the whole structure and provides a magnetic field of 0.5 T; the resulting effect is a curvature of charged particles that is used to determine their mass and charge. Another key piece of the central barrel are the two fast interaction triggers that enclose the ITS in beam direction and act as a measurement of the moment in time and a counter for forward multiplicity of an event.

The next stage of the experiment is made out of a number of different detectors that are build as layers on top of each other. The first of which is the Time Projection Chamber (TPC) whose purpose is to assist in the task of tracking along with identifying particles via their energy loss. Measured signals in the TPC are matched to the outgoing tracks of the ITS resulting in better identification and a reduction of the error from effects such as track splitting and merging. Additionally, due to its large width, it also provides the capabilities of achieving great $\mathrm{d}E/\mathrm{d}x$ resolution and is therefore used for particle identification. The Transition Radiation Detector (TRD) follows and is employed to single out electrons above 1 GeV/c, by detecting transition radiation, and lower the background of misidentified hadrons; electrons below this threshold can be distinguished in the TPC. The trifecta of ITS, TPC and TRD allows studies of light and heavy vector-meson resonance production. The final layer covering the full azimuth is the Time-Of-Flight (TOF) detector; its specialization is that of particle identification in the intermediate momentum range by measuring their travel time. Consisting of Multi-gap Resistive-Plate Chamber (MRPC) strip detectors, the TOF can discriminate pions, kaons and protons up to a few GeV/c and paired with the ITS and TPC aid in the reconstruction of tracks and vertices.

The last three detectors confined within the solenoid magnet are: the High-Momentum Particle Identification Detector (HMPID), a ring-imaging Cherenkov detector; the ElectroMagnetic Calorimeter (EMCal) composed of Pb-scintillator sampling calorimeters; and the Photon Spectrometer (PHOS) which uses PbWO4 crystals as scintillators with an Avalanche Photon Diode (APD) readout, same as the EMCal.

3.2 Inner Tracking System

As already stated, the purpose of the inner tracking system is to find the primary vertex by tracking particles at the early stages of an emission. Originally, the ITS was constructed out of three sets of two layers of detectors: the first employed Silicon Pixel Detectors (SPD); the next set was comprised of Silicon Drift Detectors (SDD); and the final was fitted with double-sided Silicon micro-Strip Detectors (SSD). During the LHC Long Shutdown 2 these detectors where replaced with Monolithic Active Pixel Sensors (MAPS) in the form of ALPIDE chips with the goal of reaching greater tracking precision.

The chips are built as a matrix of 152×1024 sensing pixels that individually measure

29.24 µm × 26.88 µm resulting in a total size of 15 mm by 30 mm and a higher granularity for all layers. The current iteration, the ITS2, consists of seven layers of MAPS, three for the inner barrel and four in the form of two sets of double layers for the outer barrel. The upgrade concludes in an improvement of the material budget per layer to 0.36% X_0 (radiation length) for the inner barrel and 1.10% X_0 for the outer, compared to the global 1.14% X_0 of the original. On a side note, the beam pipe was likewise reduced in

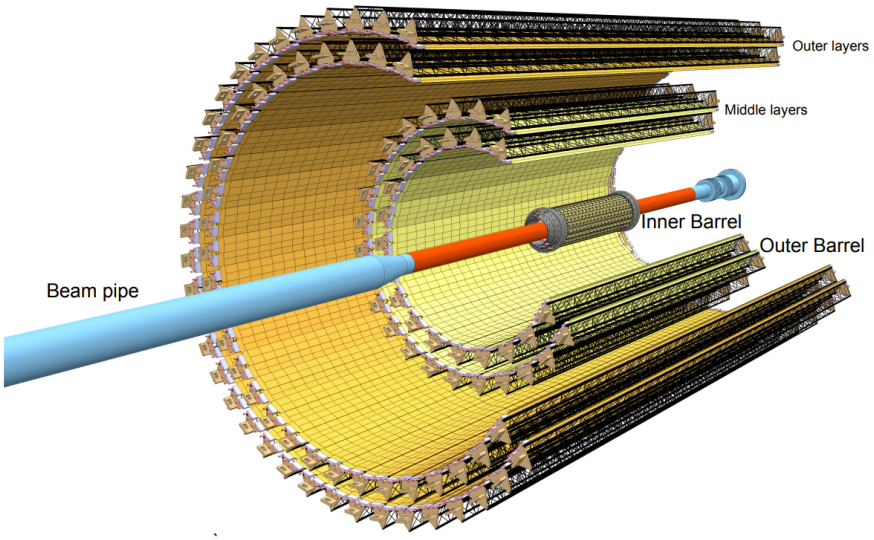

Figure 3.3: The ITS2 detector constructed out of 7 layers of MAPS, taken from [16].

size to 18 mm for the outer radius, which was achieved by replacing the segment with one made out of beryllium, and allowed to shrink the radial dimension of the ITS to 22-395 mm. Compared to its predecessor which extended from 39 mm to 430 mm, the innermost layer now sits 17 mm closer to the interaction point and thus helps achieve greater precision in the task of finding the primary vertex. Additionally, pseudorapidity coverage increased by 0.4 units to $|\eta| \leq 1.3$. Overall, the spatial resolution saw a major increase from 12 µm × 100 µm (rφ × z) to 5 µm × 5 µm.

3.3 Time Projection Chamber

The time projection chamber is a large hollow cylindrical detector that covers the entire azimuth around the interaction point and a symmetrical pseudorapidity range of $|\eta| < 0.9$. Its radial dimensions of around 85 cm to 250 cm and a length of 500 cm provide an active gas volume of 88 m^3. The cavity is filled with a mixture comprised of 90 parts Neon, 10 parts CO_2 and 5 parts N_2 wherein charged particles leave a trail of ionization when passing through. The released electrons are immediately directed by an electric field of 400 V/cm towards the outer readout planes that are divided into 18 trapezoidal segments on each side and create a projection of the taken path. Given that the chamber is split in half by a thin central electrode, the maximum drift length is 250 cm and the maximum electron drift time is 97 µs; ions take 214 ms to reach the edges.

The unavoidable drift time and, specifically, the memory time of the TPC acted as a restriction during the first two runs of the LHC and resulted in a pile-up from the merging of past tracks with more contemporary ones when an events were triggered. The maximum trigger rate limits were thus 300 Hz for Pb–Pb and 1 kHz for p–p. To mitigate these pile-up effects and improve upon the rate a new continuous readout strategy was adopted in ALICE for Run 3. However, to accommodate those ambitions the multiwire proportional chambers used until then were made obsolete and Gas Electron Multipliers (GEMs) were proposed, which could also be operated without an active ion gate unlike the former; the gate is necessary to mitigate space charge accumulation, due to ions from the amplification area, that lead to distortions of the path.

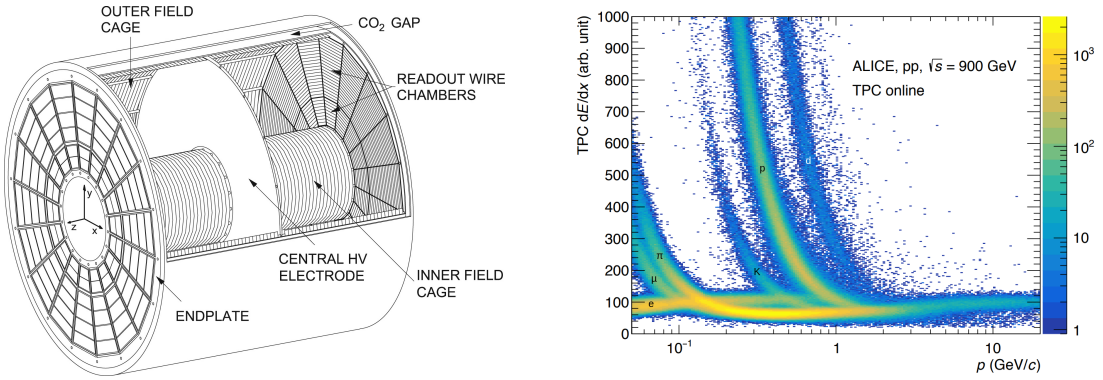

(a) ALICE TPC detector, taken from [17].

(b) $\mathrm{d}E/\mathrm{d}x$ plot, taken from [16].

Figure 3.4: A schematic view of the ALICE TPC detector and a $\mathrm{d}E/\mathrm{d}x$ plot from quality control during the pilot run in October 2021.

The improved TPC now utilizes stacks of four GEM foils that are arranged as a double layer of large-hole pitch (LP, 280 µm) foils sandwiched between foils of standard sized holes (S, 140 µm). Such S-LP-LP-S configuration enables a separation of amplification stages and a blockage of back-drifting ions that emerge from following layers, thus satisfying the requirement of below 2% backflow. The gas composition used remains Ne-CO_2-N_2 and was originally chosen for its high ion mobility, which compared to argon based mixtures halves space-charge distortions. These factors allow for a $\mathrm{d}E/\mathrm{d}x$ resolution of 5% for isolated tracks at an interaction rate for Pb–Pb of 50 kHz and for good momentum resolution in a large p_T range from a low value of 100 MeV/c up to 100 GeV/c. It is for those reasons that the TPC is the main tracking detector which also allows accurate identification of particles for low momenta. As an example, figure 3.4 (b) shows the energy loss recorded during the pilot run in 2021, which distinctly separates into the different species of particles.

3.4 Time-Of-Flight Detector

The time-of-flight detector is a subsystem of ALICE that is build as a ring of 18 segments and sits on top of the TRD. It is realized as a gas detector that employs a mixture

of $C_2H_2F_4$, i-C_4H_{10} and SF_6 in a composition of 90%, 5% and 5%. The inner radius of the ring is 3.7 m and the external 3.99 m. Each segment, which is referred to as a supermodule, contains 91 10-gap double-stack MRPC strips that are 13 cm wide and stretch for 1.22 m. The active width of the detector is 7.4 cm wherein two pads of 3.5×2.5 cm^2 fit. A total of 96 pads cover the active area which totals 120×7.4 cm^2. The detector covers 360° in azimuth and a pseudorapidity range of $|\eta| < 0.9$.

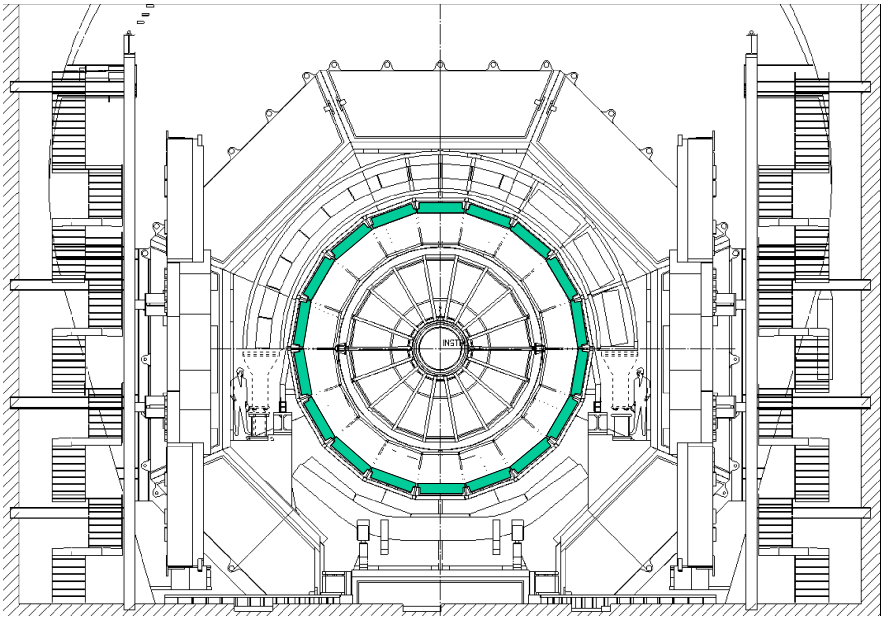

Figure 3.5: ALICE TOF detector highlighted in turquoise, taken from [18].

The TOF specializes in PID and for this reason a very high time resolution is required. This prerequisite can be realized with the MRPC technology which utilizes a high and uniform electric field throughout the gas volume. An avalanche of electrons is instantly induced when passing particles ionize the gas and, due to the size of the detector and strength of the field, the electrons are immediately absorbed which results in practically no drift time.

During the first data taking period of the LHC the detector showed a stable performance with a time resolution of 80 ps, while tests of the MRPC strips showed a time resolution below 40 ps with a very small intrinsic dead time of ∼10 ns and an efficiency close to 100% [19, 15]. The measured signals captured in one of the 18 supermodules was read by four custom VME (Versa Module Eurocard) crates that contained nine or ten Time-to-digital-converter Readout Module (TRM) boards, a single Local Trigger Module (LTM) and a Data Readout Module (DRM). The last of which was the limiting factor to accomplish the aspiration of an increased interaction rate in the next data taking period of Run 3, for which the goal of 50 kHz for Pb–Pb and 1 MHz for p–p was set. To this end, a newer Digital Readout Module 2 (DRM2) was designed and the previous modules were replaced; DRM2s offer enough bandwidth to realize the sought after continuous readout.

Returning to the workings of the TOF, signals captured in the detector are saved

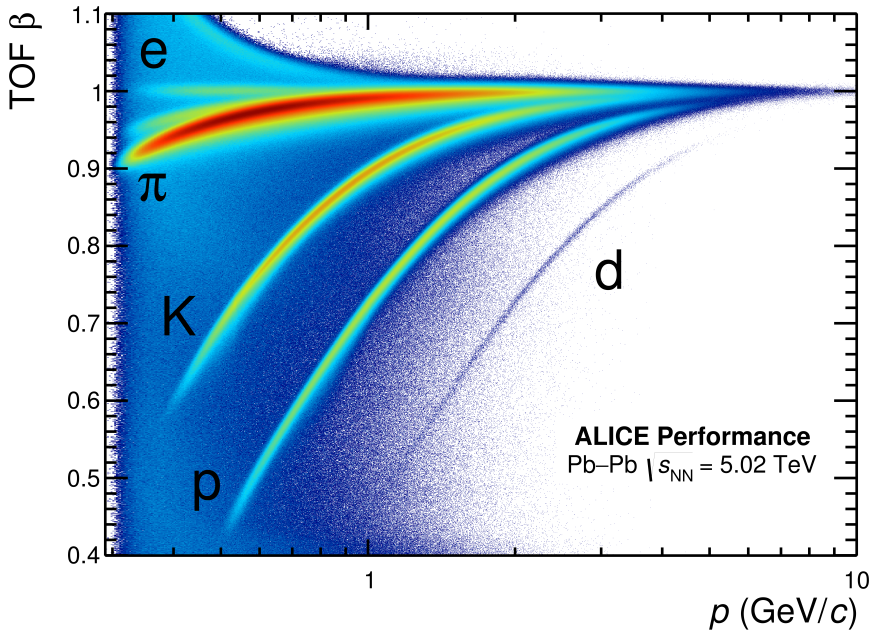

Figure 3.6: "TOF Beta vs Momentum performance in Pb-Pb at 5.02 TeV (LHC15o)", taken from the ALICE figure repository (ALI-PERF-106336).

as time stamps and used to determine the velocity of a particle. The complementary information from other detectors about the momentum enables the calculation of the mass, which is given by

$$m = p\sqrt{\beta^{-2} - 1}, \tag{3.1}$$

as a function of $\beta(p)$. This enables PID capabilities in the intermediate momentum range below 2.5 GeV/c for pions and kaons, and from 0.5 to 4 GeV/c for protons. An example of which can be found in figure 3.6 where a performance plot is shown of the $\beta(p)$ for Pb–Pb.

3.5 Fast Interaction Trigger

The fast interaction trigger is a system of four detector stations. Its purpose among other things is to signal when a bunch-crossing occurs and measure the number of collided bunches; in other words a luminometer. A single bunch contains over 10^{11} protons and intersects with a another in opposite direction roughly every 25 ns. Therefore, a dead time below 25 ns and even lower timing resolution is required to precisely assess the primary vertex. However, fluctuation around the real interaction point demand a reconstruction of the vertex which is performed offline with data from the tracking detectors. This means that a preliminary estimation is necessary for the triggering without delay and is realized by the time measurements of the time-zero (FT0) detector.

The FT0 detectors are found on each side of the interaction point, FT0-A at 3.3 m and FT0-C at 1 m on the opposite side; FT0-A is located on the left side of the detector in figure 3.2 and as can be seen in figure 3.7 in a station inside of the vertex-zero (FV0) detector. They are build as quartz Cherenkov radiators with a time resolution of $\sim$25 ps.

The FV0 is a circular detector build out of five rings of plastic scintillators. Each ring provides an equal pseudorapidity coverage and the detector achieves a time resolution of below 200 ps. This detector combined with the information of the others is used to evaluate the centrality and even plane resolution. Furthermore, pairing it up with the FT0 allows for the generation of minimum bias and multiplicity triggers.

The final detectors, the Forward Diffractive Detector (FDD), are again based on scintillators. Both of them are build with two layers of four scintillator counters and achieve a sensitivity to a single minimum ionizing particle. Its use case is among other things to provide an independent measurement of centrality and selection of ultra-peripheral collisions.

The layout of these detectors and their pseudorapidity range is shown in figure 3.7.

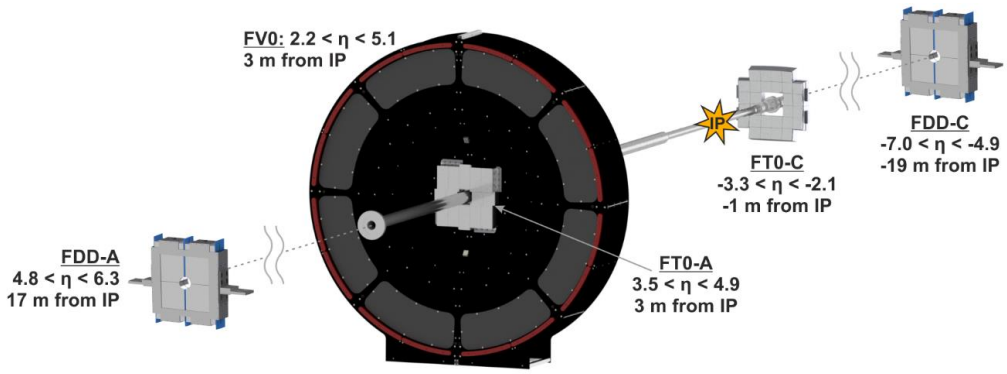

Figure 3.7: Layout of the FIT detectors, taken from [20].

4 Experimental Data

In this chapter a summary of the steps taken for the acquisition of the data will be presented. This topic is not the main focus of the thesis and was primarily performed by my colleagues with whom I worked alongside to complete the broader analysis. Nevertheless, it is as much needed to gain a deeper understanding as the rest.

4.1 O2 Physics

First, the ALICE Computing Model for the current Run 3 and future Run 4 is called the O^2 project [21] and receives its name from its Online-Offline approach.

The online aspect is represented in the readout and reconstruction tasks that have to deal with the vast amounts of data produced by the experiment. Data is accessed through the Common Readout Units (CRUs) that act as a front end interface to the individual detectors and whose task is to gather signals from the continuous readout. The bandwidth of the unfiltered signal reaches 3.5 TB/s and can be compressed by parsing the original time frames, named Heartbeat Frames (HBF), into Sub-Time Frames (STF) which amount to ≈ 20 ms and lower the bandwidth to 0.9 TB/s. This first compression allows for a manageable throughput and thus a viable first-hand quality control, in addition to any necessary calibrations. Thereafter, a further combination of the frames is performed by Event Processing Nodes (EPNs). Around 128 LHC orbits are merged into a Time Frame (TF) which represents the unit of precision to which tracks can be discriminated. Finally, the TFs are compressed into Compressed Time Frames (CTFs) and contain ≈ 20 ms of the processed data of all active detectors. CTFs are then saved into persistent memory for further offline analysis.

The offline element comes into play later in the asynchronous reconstruction of the tracks which require their full track information. For example, secondary track contributions from weak decays are taken into consideration in the TPC by performing an on-the-fly recalibration. Furthermore, it also represents the offline tasks necessary for retrieving data to perform an analysis.

More extensive information about the handling of the raw data can be found in the technical design report of the computing system [22].

4.1.1 The O2 Software Framework

The filtered and persistent data from the experiment is made accessible through Analysis Object Data stored in ROOT trees as AO2D files, from the ROOT data analysis framework [23]. These files constitute the basis of any analysis and store physical properties of collisions as columns with their respective rows characterizing analytical objects such as tracks. Instances of these matrices are called tables and can be filtered

and partitioned efficiently with the assistance of helper tasks, which are necessary since derived information such as the momentum of particles is calculated on-the-fly. Parsed tables can be saved or subsequently passed to further tasks to create new tables. This approach lowers the amount of data that needs to be saved persistently at a computational cost and with the additional benefit of turning an analysis into a chain of helper tasks.

Producer tasks similarly generate tables of data but are developed by groups of researchers that might specialize in certain physics; such tasks are made available to all members and can be used analogously to helper tasks. Furthermore, these tasks can be used to generate data models whose output is, unlike helper tasks, saved as derived datasets for future reference. Digital storage limitations require the area of applicability to be broad enough to justify saving. An example of a producer task is the FemtoDream framework that was used for this analysis to generate the same event and mixed event distributions for the correlation functions.

4.1.2 The FemtoDream Framework

The FemtoDream framework provides the best environment to generate the necessary distributions for the analysis of the p–p and p–Λ correlation functions and, more generally, for femtoscopic analyses. Its principle follows the general guidelines of attaining the maximum reduction in size while retaining the most information possible. The project can be found in the O^2 github repository under `/PWGCF/FemtoDream` [24].

The core of the framework lies in its producer task: `femtoDreamProducer`; whose combination with `femtoDreamPairTaskTrackTrack` and `femtoDreamPairTaskTrackV0` allows for selecting charged and neutral particles, respectively. The `Producer` is used to generate the derived dataset and save the most crucial properties from selected particles in two O^2 tables: `FDParticles` and `FDCollisions`. The structures of the tables are shown in table 4.1. `FDParticles` encompasses the characteristics of particles, as its name suggests, and starts off with the three necessary kinematic variables p_T, η and φ, needed for the computation of their momentum. The variable `PartType` is used to save the identity of the particle and defines the method to estimate the primary fraction of a candidate by setting the variable `TempFitVar` to either use the distance of closest approach (DCA) or for V0 candidates the cosine of the pointing angle (CPA). The DCA quantifies the proximity of a reconstructed trajectory of a particle to the primary vertex and the CPA gauges the alignment of the reconstructed momentum with the reconstructed decay path. For the later the invariant mass is saved to evaluate the mass hypothesis; in `MLambda` for particles and `MAntiLambda` for the antiparticles. Additionally, in case of a particle reconstructed from their decay products, such as a Λ, the daughters are linked to the mother through the `Children` variable. The final two, `Cut` and `PIDCut`, are used as bit masks internally to specify which selection criteria were passed and primarily concern detector specific variables. The combination of these few variables is already enough to only tag relevant particles and generate the derived dataset with a reduction factor of size of around 200. Moreover, for the purpose of reducing computational load, only those events are selected that contain the particles of interest; for example, in p–Λ correlations events with at least one proton and a Λ

baryon are taken.

The FDCollisions table is used to link related particles to a collision and subsequently apply the event mixing techniques for the mixed k^* distributions. To this end, the z position and the multiplicity of an event are stored; the former in the PosZ variable while the later utilizes two variables: V0M for the amplitude of the V0M detector, and MultNtr for the number of tracks. The sphericity of the event is stored in Sphericity and lastly the strength of the magnetic field in the MagField variable. While the first is not needed for the mixing, the later is necessary to reduce the error caused from the effect of track splitting, where two separate tracks are reconstructed from a single physical one.

FemtoDream datamodel

FDParticles

Pt	float	p_T of the particle
Eta	float	η of the particle
Phi	float	φ of the particle
PartType	integer	value associated to particle type
TempFitVar	float	variable for the template fits
Cut	integer	cutbit for selection cuts
PIDCut	integer	cutbit for PID cuts
Children	internal link	links a Λ ($\overline{\Lambda}$) candidate to its decay products
MLambda	float	invariant mass of Λ
MAntiLambda	float	invariant mass of $\overline{\Lambda}$

FDCollisions

PosZ	float	z coordinate of the primary vertex
MultV0M	float	multiplicity based on the V0M signal
MultNtr	float	number of primary charged tracks with $\eta < 0.8$
Sphericity	float	event sphericity
MagField	float	strength of detector magnet

Table 4.1: The FemtoDream datamodel for particle candidates and collisions. The contained variables in each table are listed in the first column alongside their type and a description of each.

4.2 Event Selection

To perform the analysis of the p–p and p–Λ pairs, it is necessary to reconstruct the tracks of both protons and Λ particles. To ensure the best quality selection cuts to the

data have to be applied to discriminate background from true signal. Accordingly, the minimum bias data, composed of all collisions including high and low multiplicity events, is used to study the pairs. The following sections describe in more detail the cuts applied to protons and Λ particle candidates.

4.2.1 Proton Candidate Selection

The selection cuts for the protons and antiprotons follow a similar criteria to the Run 2 analysis [8]; adapted however to the new detectors of ALICE and can be found in table 4.2. Given that protons can be directly measured by reconstructing their tracks, the selection cuts of the particle candidates are presented as selection criteria for the tracks. The chosen pseudorapidity range is symmetrical and below 0.8 units. The detectors used to find the primary vertex, the ITS and TPC, and those for PID are capable of measuring at larger values; to achieve greater quality of the tracks and secure the reconstruction the range is reduced. The interval of transverse momentum is $0.5 < p_{\mathrm{T}} < 2.2\,\mathrm{GeV/c}$ for which protons of below $0.75\,\mathrm{GeV/c}$ are identified exclusively by the TPC. For values above $0.75\,\mathrm{GeV/c}$ both TPC and TOF are used and the combined number of standard deviations, $n_{\sigma,\mathrm{comb}} = \sqrt{(n_{\sigma,\mathrm{TPC}})^2 + (n_{\sigma,\mathrm{TOF}})^2}$, is used to apply the cut on the n_σ of below 3 units; the deviation represents the agreement of measured to expected value.

Track selection criteria	
Pseudorapidity	$\lvert\eta\rvert < 0.8$
Transverse momentum	$0.5 < p_{\mathrm{T}} < 2.2\,\mathrm{GeV/c}$
TPC cluster	$n_{\mathrm{TPC}} > 80$
Crossed TPC rows	$n_{\mathrm{crossed}} > 80$
Distance of closest approach xy	$\lvert\mathrm{DCA}_{xy}\rvert < \left(0.105 + \frac{0.0305}{(p_{\mathrm{T}} \,/\, \mathrm{GeV}/c)^{1.1}}\right)$ cm
Distance of closest approach z	$\lvert\mathrm{DCA}_z\rvert < 0.1\,\mathrm{cm}$
Particle identification	$\lvert n_{\sigma,\mathrm{TPC}}\rvert < 3$ for $p < 0.75\,\mathrm{GeV/c}$ $n_{\sigma,\mathrm{comb.}} < 3$ for $p > 0.75\,\mathrm{GeV/c}$

Table 4.2: Selection criteria for the proton candidates.

Within the TPC a cut on the clusters and the crossed rows is imposed. The first determines the number of clusters assigned to a single track and is set to at least 80, which guarantees enough hits in the detector to achieve great track quality for the measurement of the momentum. The latter sets the threshold on the count of crossed rows from the available 152 of the TPC readout pads.

Lastly, for the distributions of DCA in the transverse plane, DCA_{xy}, and in z-direction, DCA_z, a cut on the distance is necessary to suppress contamination of non-primary protons; for example, material protons from interactions with the matter of the detector or secondary protons from the decays of Λ particles, both contributing to the back-

ground signature. The DCA_z is cut at a value of 0.1 cm while for the DCA_{xy} the formula $(0.105 + 0.0305/(p_T/\mathrm{GeV/c})^{1.1})$ is used to set a p_T dependent cut. The information from the TOF for high p_T tracks allows for a more precise track to vertex association and therefore a more narrow cut to the DCA distribution.

4.2.2 Λ Baryon Candidate Selection

The selection cuts for the Λ and $\overline{\Lambda}$ particles differ substantially from those of the protons due to their nature, as they are neutral charged and thus require to be reconstructed from their decay products. The most common decay mode of a Λ with a branching ratio of 63.9 % is the weak decay into a proton and a negatively charged pion, $\Lambda \rightarrow \mathrm{p} + \pi^-$. The topology of such an event is a split of the single trajectory into two diverging tracks due to the curvature from their opposed charges in the magnetic field of the experiment; this characteristic classifies it as a V_0 decay and necessitates cuts to the V_0 candidates as well as the daughter tracks, both of which can be found in table 4.3.

Daughter track selection criteria	
Pseudorapidity	$\lvert\eta\rvert < 0.8$
TPC Cluster	$n_{TPC} > 70$
DCA from primary vertex	$\lvert\mathrm{DCA}\rvert > 0.05\,\mathrm{cm}$
Particle identification	$n_{\sigma,\mathrm{TPC}} < 5$
V_0 selection criteria	
Transverse momentum	$p_T > 0.5\,\mathrm{GeV/c}$
Λ decay vertex	$\lvert i_{\mathrm{vertex}_\Lambda}\rvert < 100\,\mathrm{cm}, i = x, y, z$
Transverse radius of the decay vertex r_{xy}	$0.2 < r_{xy} < 100\,\mathrm{cm}$
DCA of daughter tracks at the decay vertex	$\mathrm{DCA}_{daugh} < 1.5\,\mathrm{cm}$
Pointing angle α	$\cos\alpha > 0.99$
K^0 rejection	$0.48 < \mathrm{M}_{\pi^+\pi^-} < 0.515\,\mathrm{GeV/c^2}$
Λ selection	$\lvert M_{p\pi} - M_{\Lambda,\mathrm{PDG}}\rvert < 8\,\mathrm{MeV/c^2}$

Table 4.3: Selection criteria for the Λ candidates.

Beginning with the similarities to the protons, the daughter tracks are selected in the same pseudorapidity range of $|\eta| < 0.8$ but require a minimum of 70 hits in the TPC clusters. For these tracks a DCA larger than 0.05 cm is used and for PID the number of standard deviations in the TPC is chosen to be $n_{\sigma,\mathrm{TPC}} < 5$. For the V_0 candidates the DCA is set to a maximum of 1.5 cm. The DCA allows to determine the decay vertex between the daughter tracks from the decay vertex of the Λ and combined with the CPA appraise the purity of the candidates; the CPA is defined as the angle between the

momentum vector of the particle candidate and the line connecting the primary vertex to its decay vertex. The CPA, which is calculated as the cosine of the pointing angle α, is chosen to be above 0.99.

For the V_0 candidates a minimum transverse momentum of 0.5 GeV/c is required to register and their invariant mass needs to fall within $\pm 8\,\mathrm{MeV/c^2}$ of the PDG mass of $1115.683(6)\,\mathrm{MeV/c^2}$ to be classified as a Λ particle. Candidates with an invariant mass compatible with a K^0 meson, under the assumption of a $\pi^+\pi^-$ decay, are dismissed from the sample.

4.2.3 Analysed Datasets

On a final note, the analysed Run 3 dataset for this analysis is the LHC22_pass4_highIR, which stands for the fourth reconstruction pass of the high interaction rate data taken in 2022. The total events alongside the count of protons, Λ particles and pairs in the derived dataset, generated by the FemtoDream producer, are listed in table 4.4. The full dataset is additionally catalogued into the individual data taking periods for which the configuration of the detector was the same. The different periods differ in some aspects of the setup but the overall characteristics are deemed to be of similar quality. The original raw data for the dataset was deleted due to disk space constrains, which makes the fourth reconstruction pass the last of its kind. Nevertheless, this dataset is the most suited for a differential analysis as it contains the most statistics.

Number of particles in the dataset

Merge List	Events (10^9)	p (10^6)	$\overline{\mathrm{p}}$ (10^6)	Λ (10^6)	$\overline{\Lambda}$ (10^6)
FullTrain	23.6	23.9	23.2	20.08	20.6
LHC22m	2.31	2.34	2.05	1.97	1.96
LHC22o	14.6	14.8	13.2	12.44	12.91
LHC22p	1.16	1.17	1.00	0.98	0.98
LHC22r	3.0	3.06	2.71	2.57	2.58
LHC22t	2.45	2.47	2.20	2.08	2.09

Table 4.4: Number of events, protons, antiprotons, Λs and $\overline{\Lambda}$s in the dataset and from the individual periods.

5 Data Modelling

In order to correctly assess the genuine signal of the previously selected particles, it is essential to first model the different contributions that feed down into them and those that form the background, in addition to applying any necessary corrections to the data. In this chapter, the steps needed to prepare the raw data and subsequently estimate the share of the non-genuine signal are shown.

5.1 Multiplicity Re-Weighting

Starting off with a correction, after applying the event mixing techniques to generate the mixed event distribution, an unbalance is created. The same event distribution, in contrast to the mixed, is limited by the composition of the measured signal. Only a certain amount of events contain both particles of interest and contribute therefore to the same event sample. Conversely, the techniques used for the mixed rely on combining particles from different events, thus allowing the creation of pairs orders of magnitude larger than the other. However, this procedure breaks the conservation of energy and momentum, thus introducing an unrealistic multiplicity distribution and an unphysical correlation signal.

To correct for this effect the mixed event distribution is weighted in each bin by the yield of the same event. Following the example set in [25], the new weights are given by solving the condition

$$\int_0^\infty N_{\text{same},m}(k^*)dk^* = \omega_n \int_0^\infty N_{\text{mixed},m}(k^*)dk^*,$$

where for each multiplicity interval m, the N_{same} represents the yield of the same event sample, N_{mixed} the yield of the mixed, and ω_m are the weights for each class. The resulting value for the mixed event yield is thus given by

$$N'_{\text{mixed}}(k^*) = \sum_m \omega_m N_{\text{mixed},m}(k^*) \tag{5.1}$$

Figure 5.1a shows the effect of the re-weighting. In the left panel the unweighted distribution (blue) is shown, which includes an order of magnitude more counts of pairs than its same event counterpart (green). The re-weighting normalizes the distribution to the yield of the same event sample and creates therefore a comparable count, shown in the right panel.

The correlation functions resulting from each sample are drawn in figure 5.1b. A difference can be spotted in both, the low and large k^* regions. The re-weighted $C(k^*)$ for lower values of k^* is larger than the unweighted, although this is then compensated in the larger k^* region.

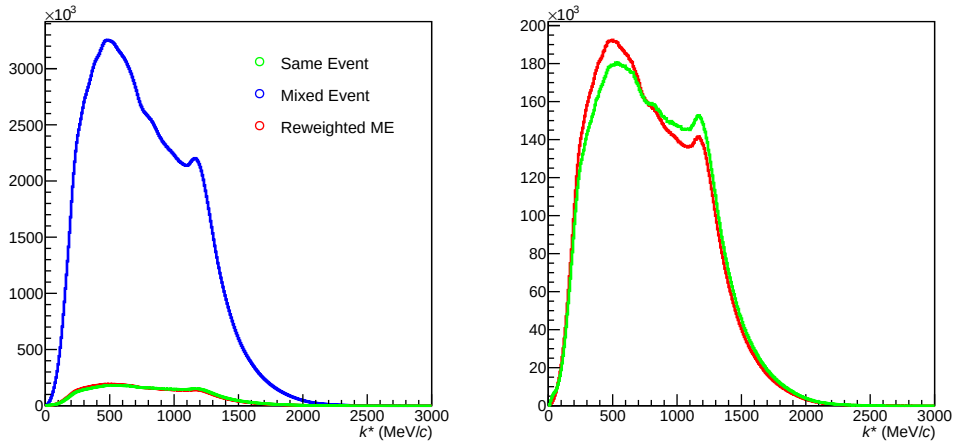

(a) The mixed event distribution (blue) and the re-weighted (red) compared to the same event distribution.

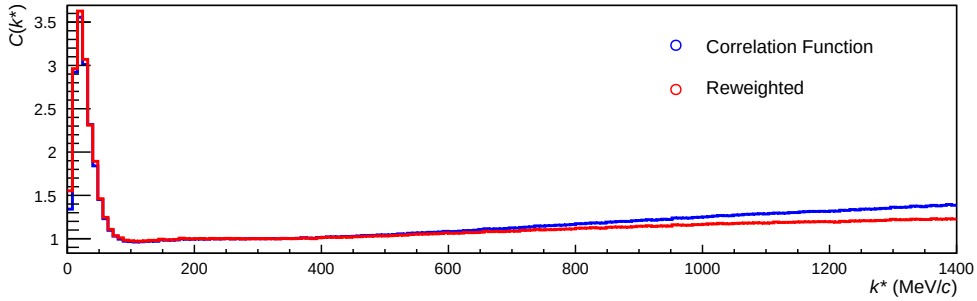

(b) The unweighted $C(k^*)$ (blue) compared to the $C(k^*)$ resulting from the re-weighting.

Figure 5.1: Comparison of the effect of the re-weighting on the mixed event distribution in the top panels, and the resulting correlation functions in the lower panel.

5.2 Decay Feed-Down

As previously mentioned, the experimental correlation function is a mixture of the genuine particle of interest and, among other things, weakly decaying resonances that feed into the same species. On the theoretical side, this not only requires consideration of the possible decay channels but also the underlying forces acting on a pair of particles. For example, the correlations between a set of protons are subject to the strong interaction, the Coulomb force and, as fermions, the antisymmetrization of the wave function.

To tackle the first hurdle, the formalism of the λ (lambda) parameters was introduced in previous analyses and concludes in a sum of the single contributions weighted by a fraction λ_i, whose sum over all adds to one [8]. In its most essential form it reads

$$C_{\text{model}}(k^*) = 1 + \sum_i \lambda_i (C_i(k^*) - 1) \tag{5.2}$$

and, as expected, adds to unity in the absence of correlations. The λ parameters are calculated as the product of the purity of a particle sample and the fraction of expected yield from the measured signal. The first can usually be obtained with the help of Monte Carlo simulations but, unfortunately, no anchored simulations to the detector were available at the time of writing and a data-driven approach was favoured based on the n_σ distribution of the TPC and TOF signal [26]. For the second, a general purpose dataset, intended for testing purposes and limited in size, was available and used to roughly estimate the share of each contribution. Consequently, the obtained fractions have to be evaluated with care as the dataset is not expected to reproduce the conditions of the detector faithfully; a detailed analysis of these is provided in the following section 5.3.

The contributions considered for the evaluation of the p–p correlation function follow the example set in [8]. Accounting for misidentified particles, the set is composed of

$$\begin{aligned}\{\text{p-p}\} = {} & \text{p-p} + \text{p-p}_\Lambda + \text{p}_\Lambda\text{-p}_\Lambda + \text{p-p}_{\Sigma^+} + \text{p}_{\Sigma^+}\text{-p}_{\Sigma^+} + \text{p}_\Lambda\text{-p}_{\Sigma^+} \\ & + \tilde{\text{p}}\text{-p} + \tilde{\text{p}}\text{-p}_\Lambda + \tilde{\text{p}}\text{-p}_{\Sigma^+} + \tilde{\text{p}}\text{-}\tilde{\text{p}},\end{aligned} \tag{5.3}$$

where protons from feed-down are represented with a subscript p_X for its mother particle X and misidentified indicated by the tilde $\tilde{X}$ for a particle of species X. Given the share and relative size of each contribution, as reported in 5.3, only the most prominent are considered to have a substantial correlation and the rest is taken as a constant, referred to as flat, equal to its λ parameter. However, the k^* dependent analysis of both, the fractions and the purity, allows likewise evaluation of the weights as a function of k^*. Therefore, the model correlation function consists of

$$\begin{aligned}C_{\text{model}}(k^*) = {} & \lambda_{\text{pp}}(k^*)\, C_{\text{pp}}(k^*) + \lambda_{\text{p}\Lambda\text{p}}(k^*)\, C_{\text{p}\Lambda\text{p}}(k^*) + \lambda_{\text{p}\Sigma\text{p}}(k^*)\, C_{\text{p}\Sigma\text{p}}(k^*) \\ & + \lambda_{\text{feed}}(k^*) + \lambda_{\text{fake}}(k^*),\end{aligned} \tag{5.4}$$

for which the less prominent feed-down contributions are merged into the flat *feed* and the misidentified into *fake*.

Similarly, the composition of the p–Λ correlation function can be listed as

$$\begin{aligned}\{\text{p-}\Lambda\} = {} & \text{p-}\Lambda + \text{p-}\Lambda_{\Sigma^0} + \text{p-}\Lambda_{\Xi^-} + \text{p-}\Lambda_{\Xi^0} + \text{p}_\Lambda\text{-}\Lambda + \text{p}_\Lambda\text{-}\Lambda_{\Sigma^0} \\ & + \text{p}_\Lambda\text{-}\Lambda_{\Xi^-} + \text{p}_\Lambda\text{-}\Lambda_{\Xi^0} + \text{p}_{\Sigma^+}\text{-}\Lambda + \text{p}_{\Sigma^+}\text{-}\Lambda_{\Sigma^0} + \text{p}_{\Sigma^+}\text{-}\Lambda_{\Xi^-} + \text{p}_{\Sigma^+}\text{-}\Lambda_{\Xi^0} \\ & + \tilde{\text{p}}\text{-}\Lambda + \tilde{\text{p}}\text{-}\Lambda_{\Sigma^0} + \tilde{\text{p}}\text{-}\Lambda_{\Xi^-} + \tilde{\text{p}}\text{-}\Lambda_{\Xi^0} + \text{p-}\tilde{\Lambda} + \text{p-}\tilde{\Lambda}_{\Sigma^0} + \text{p-}\tilde{\Lambda}_{\Xi^-} + \text{p-}\tilde{\Lambda}_{\Xi^0} + \tilde{\text{p}}\text{-}\tilde{\Lambda}\end{aligned} \tag{5.5}$$

where apart from the already introduced protons and their channels, the Λ particles themselves can also stem from feed-down. In this case, from the decay of a Ξ^- (dss), a Ξ^0 (uss) or a Σ^0 (uds) particle. Unfortunately, the Monte Carlo data needed for the constraining of the fractions was not available at the time of writing and thus the evaluation of the λ parameters defaulted to using the fractions from the previous analysis of the p–Λ correlation function [8]. The result from the fit to the data should therefore be taken as preliminary to assess the quality of the data. Further discussion is provided in the later sections. Regardless, the model correlation function is correspondingly used in the same way as in the previous analysis and reads

$$\begin{aligned}C_{\text{model}}(k^*) = {} & \lambda_{\text{p}\Lambda} C_{\text{p}\Lambda}(k^*) + \lambda_{\text{p}\Lambda_{\Sigma^0}} C_{\text{p}\Lambda_{\Sigma^0}}(k^*) + \lambda_{\text{p}\Lambda_\Xi} C_{\text{p}\Lambda_\Xi}(k^*) \\ & + \lambda_{\text{feed}} + \lambda_{\text{fake}}\end{aligned} \tag{5.6}$$

where unlike for the protons, the λ parameters are constant. Once again, the less prominent feed-down contributions are collected in the *feed* term and the misidentified in *fake*.

The final ingredient to model the experimental correlation function is to account for the non-femtoscopic background that appears at large k^*. The necessary mixed event distribution for the function is one obtained by applying event mixing techniques. As was mentioned before, such a sample does not include two-particle correlations in theory, as the individuals stem from different events. In practise, long-range effects infiltrate the distribution, for example, in the form of artificial correlations from the inability of assuring compatible single particle kinematics. As a consequence, a non-femtoscopic tail appears in the distribution.

Given that the correlation function is normalized in the region where it is assumed that no correlations of any kind are expected and the function equals unity, this interval can be used as a lower limit for modelling the baseline. The requirement of a smooth transition into the femtoscopic region is thus ensured, and a flat contribution to it by employing a third degree polynomial with its linear term removed; this additionally guarantees a flat contribution to the low k^* region. The polynomial can then be restructured by taking the constant term to be one and having a constant, associated to the normalization $\mathcal{N}$, as a value affecting the whole polynomial. The correlation function used to fit the experimental data thus reads

$$C_{\text{fit}}(k^*) = B_{\text{non-femto}}(k^*) \times C_{\text{model}}(k^*), \tag{5.7}$$

with $B_{\text{non-femto}} = \mathcal{N}\left(1 + ak^2 + bk^3\right)$.

5.3 Template Fitting

To evaluate the fractal amount of each contribution in the measured signal, a comparison of data to simulation can be performed. The signal can be fitted by spectra given by the simulation of the events in a reconstructed environment. The DCA distribution offers the best observable in the case of protons and antiprotons for this task and can be produced in the transversal plane xy or the longitudinal z.

One option to undertake such a fit is by performing a combined one to both distributions. The shapes of the individuals can be fitted by their independent spectra in each dimension while the total fraction is taken as a free parameter. Although this approach was used to gauge the contributions in the earlier stages, the loss of information from the projection onto the single dimensions and the poor quality of the simulated spectra made an approach less prone to bias a necessity. The lack of quality comes from the fact that the sum of the simulated distributions from the general purpose dataset does not accurately represent the measured signal; they include larger yield in the tails which in turn underestimates the signal region.

To mitigate the bias a two-dimensional fit of the DCA_{xy} vs DCA_z is favoured. This allows for better capture of the topology and is less prone to outliers in the signal. For the evaluation of the proton and antiproton fractions, a set of five two-dimensional

templates is used: primary, the genuine signal; secondary, from the feed-down of either a Λ or Σ particle whose spectra are similar to such an extend that they cannot be separated in the fit; wrong collision, from pile-up of the events; material, stemming from interactions which cause the material to release protons; and misidentified (fake), whose fraction is fixed to the value given by the purity. An example of such a fit is shown in figure 5.2a, where the resulting fit is drawn as a red mesh on top of the DCA distribution.

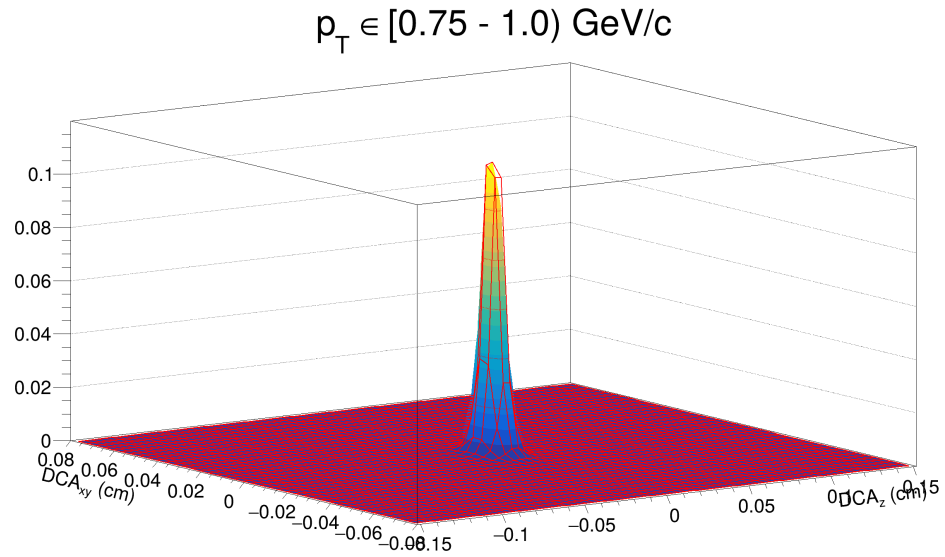

(a) Two-dimensional fit drawn as a red mesh over the DCA distribution.

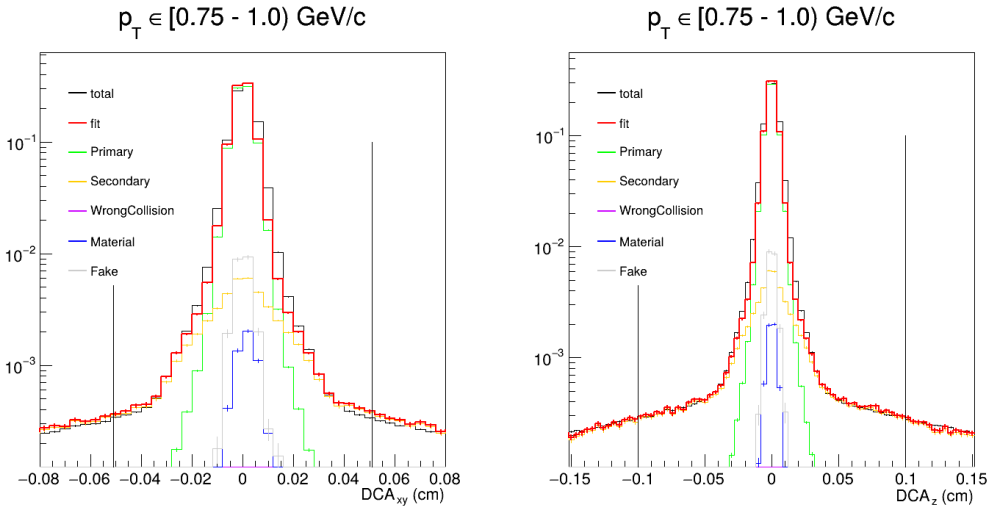

(b) Projection of the DCA fit with vertical lines drawn to indicate the signal region.

Figure 5.2: Two-dimensional fit of the DCA_{xy} vs DCA_z distribution of antiprotons in the p_T range of [0.75, 1.00) GeV/c.

In this analysis the template fitting is performed differentially in the p_T ranges of: [0.500, 0.625), [0.625, 0.750), [0.750, 1.000), [1.000, 1.500), [1.500, 2.200) GeV/c. The DCA

region for the execution of the fit is in all cases 0.5 cm in DCA_{xy} and 0.2 cm in DCA_z. To evaluate the fraction of each contribution a signal region is defined wherein the share of each in relation to the total is computed. The signal region in DCA_z is a constant 0.1 cm while for DCA_{xy} the formula

$$\left(0.0105 + \frac{0.035}{\langle p_\mathrm{T} \rangle^{1.1}}\right) \mathrm{cm}$$

is used to define a symmetrical region that captures the shrinking characteristic of the distribution with increasing p_T. Figure 5.2b shows the projection of the two-dimensional fit in the selected fit range in each dimension, and the signal region used for the calculation of the fractions. As is evident, the fit (red line) does not completely reproduce the experimental distribution (black line) due to the aforementioned discrepancy in the templates. The tails of the distribution are overestimated while the signal region is underestimated. To reflect this inaccuracy, the hereby obtained fractions will later be varied a certain percentage to compute the systematic uncertainty from fitting with the λ parameters obtained from these fits.

Repeating the fit for all the p_T bins allows to create a scaling which is later used alongside the purity of the different constituents to generate the k^* dependent λ parameters. The resulting scaling for both protons and antiprotons is shown in 5.3. The average value for protons is $\approx 87\%$ while for antiprotons it is $\approx 91\%$. The difference is due to the proton signal being contaminated in the lower p_T values by material protons and by the lack of separation in the TOF signal at high momenta between kaons and protons.

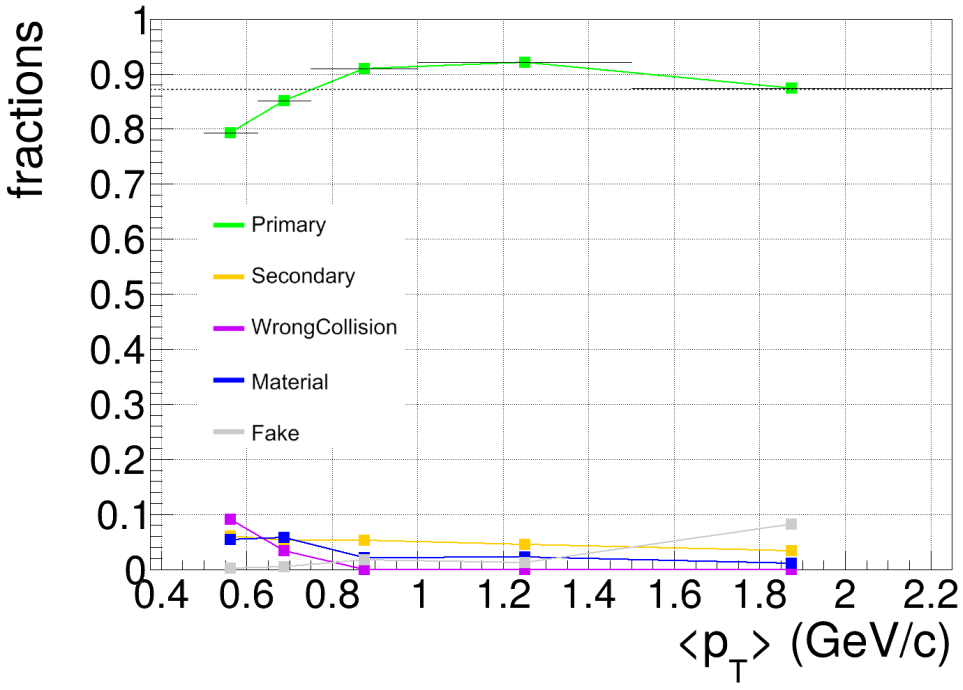

(a) Proton fractions.

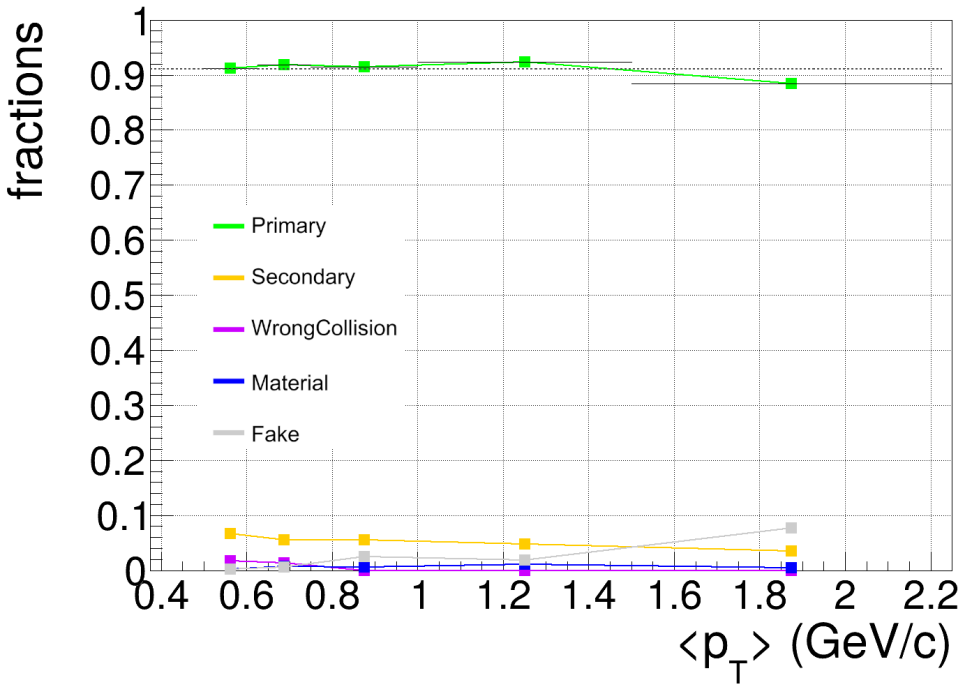

(b) Antiproton fractions.

Figure 5.3: Fractions resulting from a two-dimensional fit of the DCA distribution in five p_{T} bins.

5.4 Resonance Source Model

To review the results in the later sections it is necessary to compare them to those of previous analyses that concluded a common hadron-emission source [9, 27].

Given that the size of the source in pp collisions is around 1-2 fm and resonances that decay via the strong nuclear force have a typical decay length around the same size of 1 fm, it stands to reason that the source functions is affected by them. In other words, the modelled source is the effective size measured for a correlation function. This reasoning was the inspiration to develop the Resonance Source Model (RSM) and capture the effect of resonances on the source function.

The assumptions behind the RSM are: an equal time of emission of all primordial particles and resonances; an independent emission of all primordial particles and resonances from the same *core* source distribution; and a free propagation of the resonances before decaying. The last of them is rationalized by the difference in time-scales between the decays and the final state interactions.

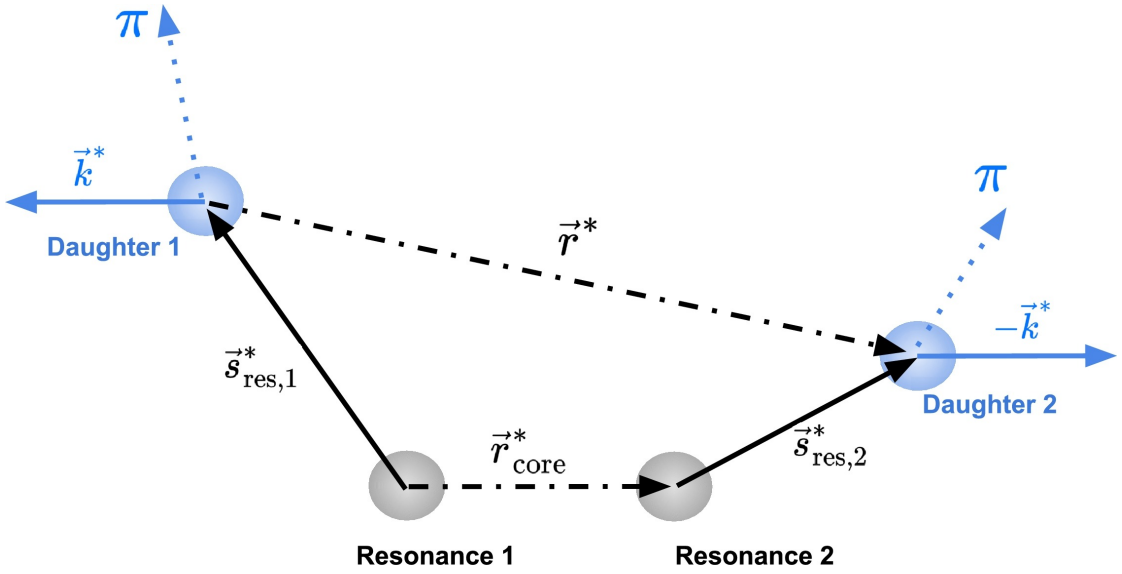

Figure 5.4: Sketch of the decay and propagation of resonances (gray) affecting the core radius of the source function for the particles of interest (blue), taken from [9].

The idea behind the RSM is to have the core source distribution as a basis, broadened by a halo representing the spatial offset induced by the resonances. Schematically, it can be illustrated as two particles separated by an effective size r^* that originate from, for example, two resonances at a closer distance r^*_{core}. A representation can be seen in figure 5.4, where the resonances decay into the particles of interest after a distance s^* in the pair rest frame; alternatively, the combination of a single resonance decaying and a primordial particle contributes to the source similarly. The computation of the distribution therefore requires the specification of the resonance yields in the form of their abundances and their decay kinematics. The first can be obtained through calculations based on the Statistical Hadronization Model (SHM) [28]. For protons

the fraction of primordial particles is 35.78 % and for Λ particles it is 35.62 %; the rest of the particles are taken as the product of resonance decays. The kinematics can be computed with the help of the EPOS transport model [29]. Through Monte-Carlo simulation the spatial coordinates of the emission can be generated from which the angular distribution of the decays are created. Combining this information with the lifetimes of the decay channels is enough to account for the dynamics. For protons the average lifetime of the resonances is $\langle c\tau_{\mathrm{res}} \rangle = 1.65\,\mathrm{fm}$ and their average mass is $\langle m_{\mathrm{res}} \rangle = 1.362\,\mathrm{GeV/c^2}$. The resonances for Λ particles have a larger lifetime of $\langle c\tau_{\mathrm{res}} \rangle = 4.69\,\mathrm{fm}$ and a mass of $\langle m_{\mathrm{res}} \rangle = 1.463\,\mathrm{GeV/c^2}$ [25].

As an example of the effect of the resonances, the effective source function and a core distribution of the same size are shown in figure 5.5 for the p–p and p–Λ system. The discontinued lines show the effective size while the dots represent the combination of core distribution and resonance halo. The difference is substantial, as the source function is parametrized as a Gaussian and the large tails from the resonances broaden the distributions, thus generating a larger width.

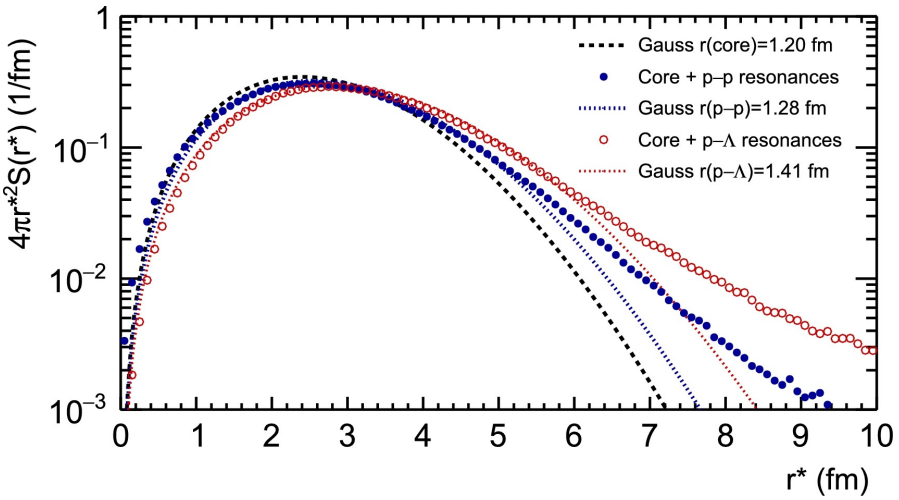

Figure 5.5: Comparison of the core and effective source functions for p–p and p–Λ, taken from [9].

In previous analyses the discovery was made that by computing the core source size differentially in m_{T} for the p–p and p–Λ system, a common scaling appeared [9]. This claim will be further investigated in the femtoscopic analysis of the data from Run 3 and extended by a differential study in multiplicity.

6 Femtoscopic Analysis

In this chapter, the selected particle pairs are first split differentially in transversal mass m_{T} and multiplicity, and subsequently fitted with the previously constructed model to obtain a measurement for the source. Additionally, a comparison for the p–p system with different potentials is performed.

6.1 Data Partitioning

The candidates, selected in section 4.2, from the different periods, listed in table 4.4, and their resulting same and mixed event distributions, are first merged into single distributions representing the whole dataset and subsequently re-weighted according to section 5.1. The evaluation of the correlation function for both p–p and p–Λ is then executed differentially in m_{T} and in the three multiplicity percentiles: 0-10%, 10-50%, and 50-100%. The percentiles correspond to the decreasing number of particles in an event. The smallest percentile represents the events with the highest count of particles while the largest the events with the least particles. To this end, the same and mixed event distributions for the systems are divided in m_{T} segments containing approximately the same amount of pairs. The p–p and $\overline{\mathrm{p}}$–$\overline{\mathrm{p}}$ systems are split into seven intervals: [1.02, 1.14), [1.14, 1.20), [1.20, 1.26), [1.26, 1.38), [1.38, 1.56), [1.56, 1.86), [1.86, 2.40) GeV/c; these correspond to the values that were used in the previous analysis [9]. The number of pairs for each are listed in table 6.1, where the p–p and $\overline{\mathrm{p}}$–$\overline{\mathrm{p}}$ pairs are

Number of p–p and $\overline{\mathrm{p}}$–$\overline{\mathrm{p}}$ pairs

	p–p			$\overline{\mathrm{p}}$–$\overline{\mathrm{p}}$		
m_{T} [GeV/c]	0 - 10%	10 - 50%	50 - 100%	0 - 10%	10 - 50%	50 - 100%
[1.02, 1.14)	6.98×10^7	1.12×10^8	3.99×10^7	5.40×10^7	8.60×10^7	3.01×10^7
[1.14, 1.20)	2.91×10^7	4.51×10^7	1.51×10^7	2.27×10^7	3.49×10^7	1.15×10^7
[1.20, 1.26)	2.50×10^7	3.77×10^7	1.21×10^7	1.99×10^7	2.97×10^7	9.57×10^6
[1.26, 1.38)	3.86×10^7	5.60×10^7	1.73×10^7	3.17×10^7	4.56×10^7	1.41×10^7
[1.38, 1.56)	3.75×10^7	5.12×10^7	1.49×10^7	3.22×10^7	4.37×10^7	1.28×10^7
[1.56, 1.86)	2.50×10^7	3.13×10^7	8.56×10^6	2.30×10^7	2.86×10^7	7.96×10^6
[1.86, 2.40)	5.38×10^6	6.06×10^6	1.60×10^6	5.38×10^6	6.11×10^6	1.68×10^6

Table 6.1: Number of p–p and $\overline{\mathrm{p}}$–$\overline{\mathrm{p}}$ pairs divided in seven m_{T} bins for the three multiplicity percentiles of 0-10%, 10-50%, and 50-100%.

subdivided into two tables split into the three multiplicity percentiles and each row represents a single m_T interval. As can be seen, most distributions include $\approx 10^7$ entries regardless of multiplicity and m_T; only in the highest range of both do the counts drop to 10^6 entries.

For the p–Λ and $\overline{\text{p}}$–$\overline{\Lambda}$ systems six intervals are used, which correspond again to the values from the same analysis and are: [1.08, 1.26), [1.26, 1.32), [1.32, 1.44), [1.44, 1.65), [1.65, 1.90), [1.90, 4.50) GeV/c; for which the number of pairs are listed in table 6.2. This gives a total of 21 correlation functions for each proton particle pairs and antiparticle pairs, respectively, and 18 for the p–Λ and $\overline{\text{p}}$–$\overline{\Lambda}$ pairs each.

Number of p–Λ and $\overline{\text{p}}$–$\overline{\Lambda}$ pairs

	p–Λ			$\overline{\text{p}}$–$\overline{\Lambda}$		
m_T [GeV/c]	0 - 10%	10 - 50%	50 - 100%	0 - 10%	10 - 50%	50 - 100%
[1.08, 1.26)	2.80×10^7	4.30×10^7	1.52×10^7	2.37×10^7	3.59×10^7	1.25×10^7
[1.26, 1.32)	8.55×10^6	1.27×10^7	4.40×10^6	7.20×10^6	1.06×10^7	3.64×10^6
[1.32, 1.44)	1.51×10^7	2.18×10^7	7.24×10^6	1.29×10^7	1.84×10^7	6.07×10^6
[1.44, 1.65)	1.97×10^7	2.66×10^7	8.23×10^6	1.71×10^7	2.30×10^7	7.09×10^6
[1.65, 1.90)	1.38×10^7	1.72×10^7	5.01×10^6	1.23×10^7	1.53×10^7	4.42×10^6
[1.90, 4.50)	1.26×10^7	1.42×10^7	3.88×10^6	1.11×10^7	1.26×10^7	3.40×10^6

Table 6.2: Number of p–Λ and $\overline{\text{p}}$–$\overline{\Lambda}$ pairs divided in seven m_T bins for the three multiplicity percentiles of 0-10%, 10-50%, and 50-100%.

6.2 Data Fitting

The fitting of the experimental data is achieved as a simultaneous fit to a set of the previously obtained correlation functions, one of each particle-particle and antiparticle-antiparticle for a given m_T and multiplicity. The shape of the distributions changes between the two, due to the different contributions as for example antiprotons are not affected by material knock-out, and therefore requires a unique modelling of both baseline and signal.

The baseline is for all cases a polynomial of third degree with its linear term removed, as described in section 5.2. The normalization is then left as a free fit parameter to absorb any bias introduced from the arbitrary normalization of the correlation functions, which is performed in a range where the distributions equal unity, for visual purposes. The chosen k^* range for this is $[240, 340]$ MeV/c. The data can then be pre-fitted with the baseline to allow a direct comparison between different models or fitted directly with eq. 5.7 to get the best overall agreement.

The signal is then separately modelled, according to section 5.2, as the sum of the individual feed-down contributions; the p–p ($\overline{\text{p}}$–$\overline{\text{p}}$) system with eq. 5.4 and p–Λ ($\overline{\text{p}}$–$\overline{\Lambda}$) with eq. 5.6. The weights of each are realized as the λ parameters and obtained in

section 5.3 from the combination of the purity of a particle and the fraction of the signal. The latter is estimated for the p–p ($\overline{\text{p}}$–$\overline{\text{p}}$) system from template fits to the DCA distribution, which uses only the merged distribution of the secondary contributions due to the individual spectra being similar to the point of detriment to the fit. For the calculation of the λ parameters of the secondary protons, the obtained values of the fraction in figure 5.3 are divided, due to isospin considerations, into a composition of 70 % from Λ and 30 % from Σ^+ particles, according to [8]. The fraction of the misidentified protons is given by $1 -$ purity of the sample. The average values of the proton and antiproton $\lambda(k^*)$ parameters are displayed in table 6.3 and as can be identified, show a strong dependence on m_{T} and a small dependence on the multiplicity. This is due to a stronger dependency on the p_{T} distribution for the m_{T} ranges.

The values for the p–Λ ($\overline{\text{p}}$–$\overline{\Lambda}$) are, as already mentioned, taken from the analysis performed in [9] and equal:

$$\lambda_{\text{p}\Lambda} = 0.5031, \;\; \lambda_{\text{p}\Lambda_{\Sigma^0}} = 0.1677, \;\; \lambda_{\text{p}\Lambda_{\Xi}} = 0.0832, \;\; \lambda_{\text{feed}} = 0.2038, \;\; \lambda_{\text{fake}} = 0.0422.$$

To model the isolated genuine signal and compare it to theory, eq. 2.3 is used. For the source function a Gaussian profile is used, as characterized in eq. 2.4. Within the simultaneous fit, the width of both distributions is shared and left as a free-fit parameter. This allows to retrieve a single value representing the size of the particle emitting source for a set of particles and antiparticles.

The last component needed is the two-particle wave function for a given pair of particles and can be obtained by solving the Schrödinger equation for a given potential. To this end, the CATS framework [30] can be used to perform the computation. Additionally, the wave functions for a given interaction can be independently calculated and later fed into the framework, alongside a source function, to compute the correlation function for any desired k^* value.

For proton pairs the strong interaction is modelled with the Argonne v_{18} potential [12] up to the L=2 partial wave (D wave) and, additionally, the Coulomb interaction and the antisymmetrization of the wave functions are taken into consideration inside of the framework. The nucleon-hyperon interaction is modelled with the help of Chiral Effective Field Theory (χEFT) [31]. The idea of this effective theory is to mediate the interaction between hadrons through pions and, thereby, reducing the degrees of freedom. The model is constrained by the available scattering data of hyperons, which is used to adjust the low-energy constants internally. For the fitting, the Next-to-Leading Order (NLO) 19 version of the model was used, in the form of wave functions, as an input for CATS; a cutoff scale of 600 MeV/c for the model is used, which internally prevents unphysical momentum contributions in the computation from higher values. Additionally, χEFT allows the calculation of the couple-channel dynamics from the coupling of N$\Sigma \leftrightarrow$ NΛ, as described in section 2.4.

The last step is to perform the fits. For this the fit region for the femtoscopic signal of the protons is set to $[0, 280]$ MeV/c, which is used internally in CATS to evaluate the interaction and thus the individual correlation functions after providing the λ parameters. The output of the framework is then used to fit the experimental data in

Average value of the proton and antiproton $\lambda(k^*)$ parameters

		Protons					Antiprotons				
	m_T [GeV/c]	$\overline{\lambda}_{pp}$	$\overline{\lambda}_{p\Lambda p}$	$\overline{\lambda}_{p\Sigma p}$	$\overline{\lambda}_{feed}$	$\overline{\lambda}_{fake}$	$\overline{\lambda}_{pp}$	$\overline{\lambda}_{p\Lambda p}$	$\overline{\lambda}_{p\Sigma p}$	$\overline{\lambda}_{feed}$	$\overline{\lambda}_{fake}$
0 - 10 %	[1.02, 1.14)	0.657	0.031	0.016	0.294	0.003	0.830	0.038	0.019	0.109	0.004
	[1.14, 1.20)	0.719	0.031	0.015	0.228	0.007	0.820	0.035	0.017	0.119	0.010
	[1.20, 1.26)	0.754	0.030	0.015	0.191	0.010	0.813	0.033	0.017	0.124	0.014
	[1.26, 1.38)	0.783	0.030	0.015	0.161	0.011	0.814	0.032	0.016	0.123	0.016
	[1.38, 1.56)	0.805	0.028	0.014	0.139	0.015	0.813	0.029	0.014	0.124	0.019
	[1.56, 1.86)	0.779	0.024	0.012	0.154	0.031	0.786	0.025	0.013	0.143	0.033
	[1.86, 2.40)	0.663	0.018	0.009	0.256	0.054	0.684	0.019	0.009	0.236	0.052
10 - 50 %	[1.02, 1.14)	0.656	0.031	0.016	0.294	0.003	0.830	0.038	0.019	0.109	0.004
	[1.14, 1.20)	0.719	0.031	0.015	0.229	0.007	0.820	0.035	0.017	0.119	0.010
	[1.20, 1.26)	0.754	0.030	0.015	0.191	0.010	0.813	0.033	0.017	0.124	0.014
	[1.26, 1.38)	0.782	0.030	0.015	0.162	0.011	0.814	0.032	0.016	0.123	0.016
	[1.38, 1.56)	0.805	0.028	0.014	0.139	0.015	0.813	0.029	0.014	0.124	0.019
	[1.56, 1.86)	0.779	0.024	0.012	0.154	0.030	0.787	0.025	0.013	0.143	0.032
	[1.86, 2.40)	0.665	0.018	0.009	0.254	0.054	0.686	0.019	0.009	0.234	0.052
50 - 100 %	[1.02, 1.14)	0.655	0.031	0.016	0.296	0.003	0.830	0.038	0.019	0.109	0.003
	[1.14, 1.20)	0.718	0.031	0.015	0.229	0.007	0.820	0.035	0.017	0.118	0.010
	[1.20, 1.26)	0.753	0.030	0.015	0.192	0.010	0.813	0.033	0.017	0.124	0.014
	[1.26, 1.38)	0.781	0.030	0.015	0.163	0.011	0.814	0.032	0.016	0.123	0.016
	[1.38, 1.56)	0.804	0.028	0.014	0.140	0.015	0.813	0.029	0.014	0.124	0.019
	[1.56, 1.86)	0.781	0.024	0.012	0.153	0.030	0.788	0.025	0.013	0.142	0.032
	[1.86, 2.40)	0.667	0.018	0.009	0.252	0.053	0.688	0.019	0.009	0.232	0.052

Table 6.3: Average value of the $\lambda(k^*)$ parameters for the different contributions for the modelling of the correlation function. The values are divided into three multiplicity percentiles and seven m_T intervals.

a range of $k^* \in [0, 400]$ MeV/c; this range is incidentally used as well for the baseline with the normalization $\mathcal{N}$ in eq. 5.7 as a free-fit parameter alongside the coefficients of the polynomial, as both baseline and signal are modelled simultaneously. For the p–Λ ($\overline{\text{p}}$–$\overline{\Lambda}$) pairs, the femtoscopic signal region is set to $k^* \in [0, 400]$ MeV/c in order to capture the topology of the cusp, resulting from the couple-channel dynamics. The fit range of these pairs for the data is set to the same interval and the fit is, similar to the protons, performed in combination with the baseline, where the baseline can be taken as another free-fit parameter.

6.2.1 Fitting with the RSM

Similarly to the previously described fitting procedure, the evaluation of the core source distribution can be accomplished by applying the RSM within a fit for both systems in an analogous approach. First, the angular distributions obtained from the EPOS transport model, as explained in section 5.4, are loaded into CATS by reading

them from files as inputs. The source is then, unlike the Gaussian profile used before, replaced by the one resulting from the RSM. This necessitates providing the model with the fraction of primordial particles and that of those resulting from strongly decaying resonances. For protons and antiprotons the value of primordial particles is $\omega_{\text{prim}} = 35.78\,\%$ and, therefore, the value for the resonances is set to 64.22 %. For Λ particles and $\overline{\Lambda}$ antiparticles the primordial fraction is $\omega_{\text{prim}} = 35.62\,\%$. Additionally, the average mass and lifetime of the resonances are required. As stated in section 5.4, the proton resonances have an average mass of $\langle m_{\text{res}} \rangle = 1.362\,\text{GeV}/\text{c}^2$ and an average lifetime of $\langle c\tau_{\text{res}} \rangle = 1.65\,\text{fm}$. The average mass of the Λ particles is set to $\langle m_{\text{res}} \rangle = 1.463\,\text{GeV}/\text{c}^2$ and their average lifetime is set to $\langle c\tau_{\text{res}} \rangle = 4.69\,\text{fm}$.

The fit itself proceeds in the same manner as the fit of the effective size from this point onwards. The femtoscopic signal is evaluated in the same range of $k^* \in [0, 280]$ MeV/c for protons and $k^* \in [0, 400]$ MeV/c for the p–Λ ($\overline{\text{p}}$–$\overline{\Lambda}$) system. The global fit region for the signal of the correlation function and the baseline is again set for both system to $k^* \in [0, 400]$ MeV/c. The baseline is likewise left unconstrained and taken as a free-fit parameter of the fit. The source modelled by the RSM then returns a value for the core distribution that, if resonances are taken into consideration, corresponds to an effective size of the same experimental data fitted with a Gaussian profile instead.

The two-particle wave function is independent of the model used for the source and thus the same interactions are considered for the systems. The p–p and $\overline{\text{p}}$–$\overline{\text{p}}$ correlation functions are modelled again with the Argonne v_{18} potential and the p–Λ and $\overline{\text{p}}$–$\overline{\Lambda}$ with the NLO19 version of the χEFT model with a cut-off of 600 MeV/c.

6.2.2 Fitting with Other Potentials

On a final note, the fitting process can also be performed by providing CATS with a potential to examine the theoretical description of the interaction and its sensitivity to the applied model for the source. The two-particle wave function is then computed by the framework and used to model the correlation function. As an alternative to the Argonne v_{18}, the Reid 68 and its next iteration, Reid 93, are considered [32, 33]. The main difference between the two is the addition of the $^1\text{D}_2$ partial wave. This can be seen from the phase shifts computed by CATS and displayed in figure 6.1b. The phase shift of the Reid 68 potential in the $^1\text{D}_2$ partial wave in yellow is zero. Another difference is the resulting phase shift of the $^3\text{P}_2$ wave, which for Reid 68 tends towards a negative value in contrast to the very similar positive curve that the Argonne and Reid 93 potentials take. Given that the partial waves and phase shifts of Argonne v_{18} and Reid 93 are very similar, the resulting fit is expected to be of similar character. The radial partial waves are shown in figure 6.2.

In order to compare the quality of the fits between the different potentials, the baseline is fitted individually in the region of $k^* \in [0, 280]$ MeV/c for a single m_{T} and multiplicity. The resulting coefficients are then used to fix the baseline within the fit of the model to the correlation function. The only free-fit parameters are the normalization and the size of the source function, which in all cases is a Gaussian profile. The resulting width of the distribution is later used to compare the size of the particle emitting source.

6.3 Systematic Uncertainties

The statistical and systematic uncertainties of the source sizes by means of fitting the correlation functions are obtained in a bootstrapping approach. The main idea is to use random sampling of the data combined with systematic variations to obtain an estimate for the total error. The square of the total can be computed as the square sum of the statistical and systematic

$$\sigma^2_{\text{total}} = \sigma^2_{\text{stat}} + \sigma^2_{\text{syst}} \,, \tag{6.1}$$

where it is assumed that they are independent of each other. Sampling the correlation function alone without any systematic variations, allows to get a distribution for the fits that should reproduce the statistical fluctuations. This allows to get the systematic uncertainty, which might be subject to some bias not considered, by subtracting the statistical from the total

$$\sigma_{\text{syst}} = \sqrt{\sigma^2_{\text{total}} - \sigma^2_{\text{stat}}} \,. \tag{6.2}$$

6.3.1 Statistical Uncertainties

To compute the statistical uncertainty, the correlation function of a single m_{T} interval for a given multiplicity is sampled by taking the value of a bin in the histogram and using its statistical uncertainty to generate a new value for it. Applying this to each bin of a correlation function generates a new sample which is then fitted with the procedure described in section 6.2 for any source or interaction. The distribution of source radii generated from the individual fits follows a normal distribution as it is expected to have as a mean the true value and the width represent the statistical fluctuations from the fitting procedure. As such, the width of the resulting distribution is taken as the statistical uncertainty.

6.3.2 Total Uncertainties

Generating the total uncertainties of a sample is a more complicated endeavour as it incorporates both fluctuations of statistical and systematic nature. The systematic introduce a non-statistical bias that originates from the fitting procedure, the reconstruction of the data, or any other source which might not even be considered. As explained earlier, the total uncertainty is used as a proxy to obtain the systematic. For this, the process to obtain the statistical error is combined with systematic variations to random sample an estimate for the total.

To this end, two sources of systematic variations are introduced into the system. First, the method to obtain the experimental data is varied itself by changing the parameters that steer the particle identification and reconstruction, i.e. the selection criteria. The second, is to change the settings of the fitting routine to introduce a bias that applies equally to all performed fits.

Systematic Variations of the Data

Starting with the variations of the selection criteria, these are only applied to the protons and antiprotons due to the computational expense of generating the distributions. The selection of the Λ ($\overline{\Lambda}$) still require further improvement and, therefore, their variations were neglected. The default values and the variations of the cuts are displayed in table 6.4 and are combined with each other to generate a total of 45 distribution, of which only those are accepted that are within 20 % of the pair yield in the range of $k^* < 200\,\mathrm{MeV/c}$. That amounts to 15 different variations of the data.

Variations of the selection criteria

Variable	Default	Variations
min p_T (GeV/c)	0.5	0.45, 0.55
max $\lvert\eta\rvert$	0.8	0.77, 0.83
max n_σ	3	2.5
max number of TPC clusters	80	70, 90
max number of shared TPC clusters	10	8, 12

Table 6.4: Variations of the selection criteria for the proton candidates.

Systematic Variations of the Fit

The variations of the fitting parameters are very similar for both systems and are shown in table 6.5 for the p–p and $\overline{\mathrm{p}}$–$\overline{\mathrm{p}}$ correlation functions, and in table 6.6 for the p–Λ and $\overline{\mathrm{p}}$–$\overline{\Lambda}$ correlation functions. The first variable varied is the femtoscopic region where the interaction is calculated; the default value is varied by $\pm 40\,\mathrm{MeV/c}$. The same amount is used to modify the range for the fitting of the correlation function and allows to capture more or less of the non-femtoscopic region, which introduces some bias into the shape of the baseline. Additionally, the λ parameters of the genuine signal are adjusted by ± 5 % to counteract the bias from the template fits performed with the general purpose dataset. This is implemented as a change to the genuine signal; the amount removed from the genuine is added as a total percentage distributed between the rest of the contributions. Lastly, for the RSM two further variations are applied. First a ± 10 % modification of the fraction of the resonances and another of the same amount to the average mass of the resonances.

Bootstrapping

Finally, with all variations configured, the method to obtain the total uncertainty of the fit is by random sampling. The aforementioned process for the statistical uncertainty is combined with the variations to obtain a value for the total. To this end, all variations

Variations of the proton fit parameters		
Variable	Default	Variations
Femtostopic range (MeV/c)	280	240, 320
Fitting range (MeV/c)	400	360, 440
λ parameter	Genuine	+5 %, -5 %
Resonance Source Model		
Resonance fraction	0.6422	+10 %, -10 %
Resonance mass (MeV/c)	1362	+10 %, -10 %

Table 6.5: Variations of the parameters for the fits of the p–p and $\overline{\text{p}}$–$\overline{\text{p}}$ correlation function.

of the experimental correlation function are merged and the resulting distribution is used for the sampling. Next, the experimental correlation function is transformed, analogous to the statistical process, by traversing the points and generating a new value for each. The first sampling is performed from a normal distribution with its mean set on the value of the point and its width equal to the statistical uncertainty of the data. Thereafter, a uniform distribution is used around the obtained value to simulate a systematic bias, which is expected to affect the correlation function uniformly. The resulting correlation function is subsequently used as the input to be fitted, for which the previously introduced fit variations are considered. The fitting procedure is then repeated with random sampled correlation functions and randomly chosen variations 500 times to generate a distribution for the total uncertainty, which should account for different biases from either the fit routine or the detection devices. The systematic uncertainty is then calculated with eq. 6.2.

Variations of the p–Λ fit parameters		
Variable	Default	Variations
Femtostopic range (MeV/c)	400	360, 440
Fitting range (MeV/c)	400	360, 440
λ parameter	Genuine	+5 %, -5 %
Resonance Source Model		
Resonance fraction	0.6438	+10 %, -10 %
Resonance mass (MeV/c)	1462	+10 %, -10 %

Table 6.6: Variations of the parameters for the fits of the p–Λ and $\overline{\text{p}}$–$\overline{\Lambda}$ correlation function.

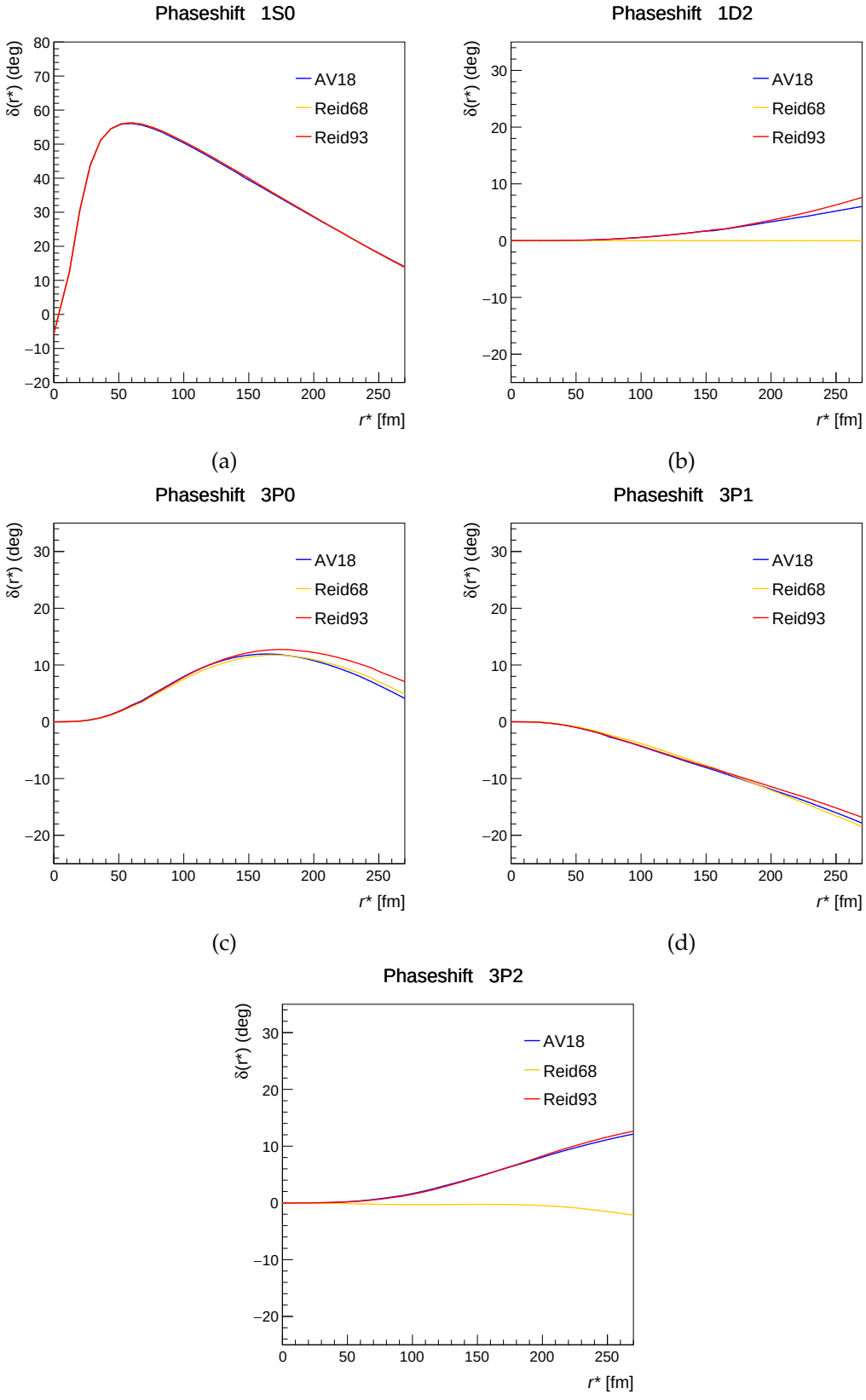

Figure 6.1: Phaseshifts of the Argonne v_{18}, Reid93 and Reid68 potentials for the partial waves $^3P_0$ (a), $^3P_1$ (b), $^3P_2$ (c), $^1S_0$ (d), $^1D_2$ (e).

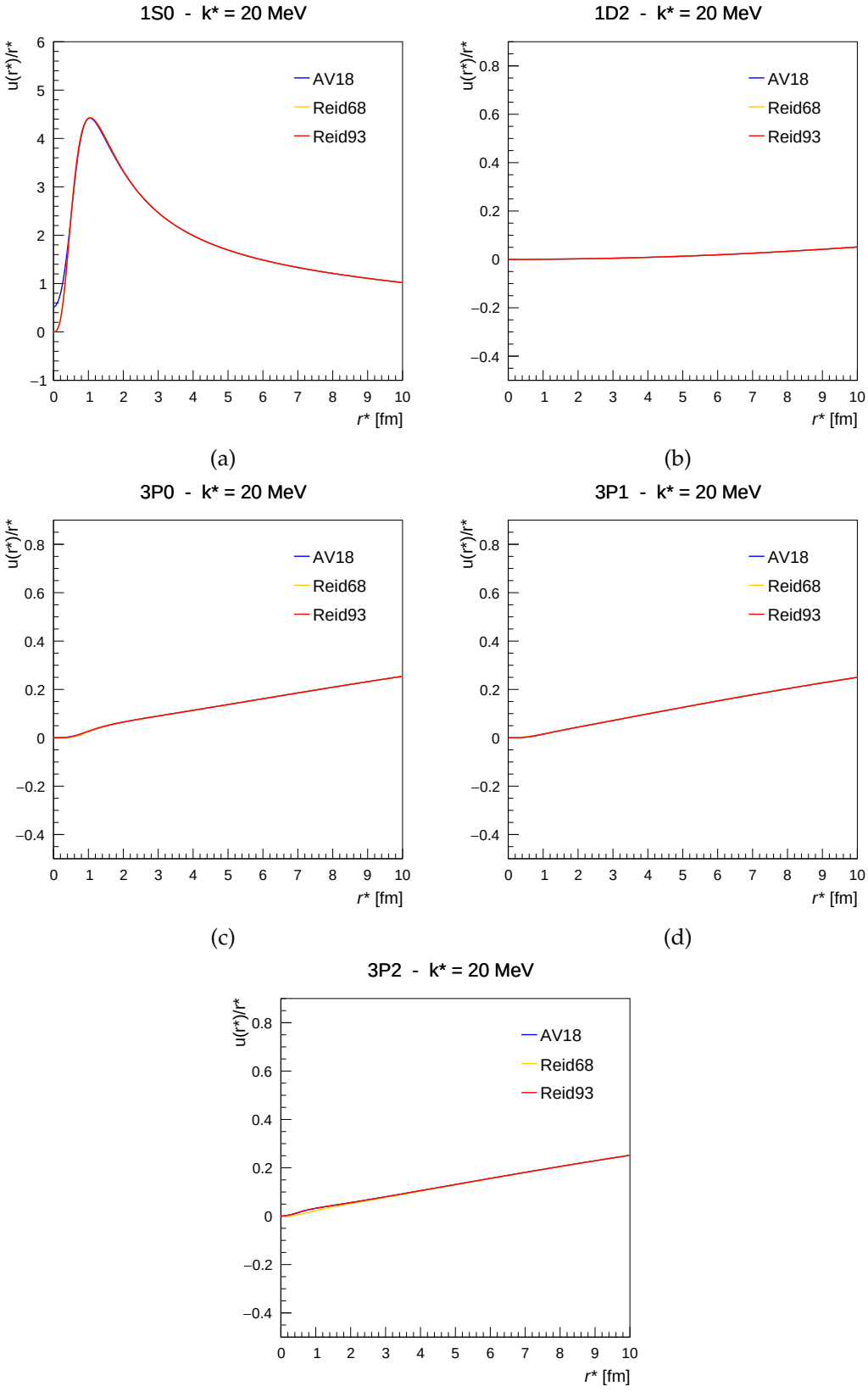

Figure 6.2: Radial wave functions for a value of 20 MeV/c in k^* of the Argonne v_{18}, Reid93 and Reid68 potentials for the partial waves $^3P_0$ (a), $^3P_1$ (b), $^3P_2$ (c), $^1S_0$ (d), $^1D_2$ (e).

7 Results

In this chapter the resulting fits to the correlation functions are shown and discussed. Each set of fits corresponds to a simultaneous fit to the particle-particle pair and the antiparticle-antiparticle pair for a given m_{T} interval and multiplicity percentile. Only a selection of the fits are shown here, due to the number of them performed; the rest can nevertheless be found in the appendix.

As an example, figure 7.1 shows the combined fit to the p–p and $\overline{\mathrm{p}}$–$\overline{\mathrm{p}}$ correlations functions for the multiplicity percentile of 0 to 10 % in the m_{T} interval of [1.02, 1.14). The markers represent the experimental correlation function from the processed ALICE data of pp collisions at an energy of $\sqrt{s} = 13.6\,\mathrm{TeV}$ and are weighted with the mean value of the mixed event distribution within the width of the bin. The weighting is most prominent in the first bin as the shape of the mixed distribution changes the most for the lowest k^* values and results in a shifted marker off the centre of the bin. The horizontal bars depict the width of the binning of the histogram and the vertical bars the statistical uncertainty of the data; the width corresponds to a binning of 8 MeV/c. The red boxes indicate the systematic uncertainty of the data from the variations performed on the selection cuts of the particle candidates. The blue band drawn alongside the data characterizes the fits performed, for which all variations of the fitting procedure, as explained in the previous chapter, are plotted as a distribution; its mean is consequently taken as the centre of the band. The distribution itself is, due to the variations introducing a systematic bias, a uniform and therefore the size of the band is obtained by taking its width divided by the square root of twelve. The baseline used in combination with the model for the correlation function is drawn as well as a gray band, for which the same method is used to obtain its width.

The lower panel displays the agreement of the fit to the data in n_σ, i.e. number of standard deviations. The value for each bin is obtained by calculating the difference of the estimate of the fit to the data and weighting the result with the total uncertainty:

$$n_\sigma = \frac{C_{\mathrm{data}}(k^*) - C_{\mathrm{fit}}(k^*)}{\sqrt{\sigma^2_{\mathrm{stat}} + \sigma^2_{\mathrm{syst}}}} \,. \tag{7.1}$$

The lower the value of the n_σ the better the agreement. In general, as will be seen across the performed fits, the value of the n_σ tends to deviate from zero for the lower bins due to the shape of the fit being dictated by the falling slope of the distribution when going from the peak of the correlation function to larger values of k^*. Nevertheless, the agreement after around 30 MeV/c improves significantly in spite of the decreasing size of the uncertainties.

Additionally, a zoomed in version of the correlation function and the fit for the p–p and $\overline{\mathrm{p}}$–$\overline{\mathrm{p}}$ systems is drawn over the histogram in the range of around [55, 165] MeV/c to show more detail about the captured shape of the distribution by the fit.

7.1 The p–p correlation function

The fits to the p–p and $\overline{\text{p}}$–$\overline{\text{p}}$ correlation functions are shown in the appendix (chapter 9). As already described, an example fit is presented in figure 7.1 from which the most prominent difference between the two systems is revealed. The correlations between antiprotons is consistently larger than for the protons over multiplicity percentiles and the lower m_{T} intervals. For higher m_{T} the difference decreases and the strength is similar, which can be seen by comparing figure 9.1 that shows the fits for the first m_{T} interval, and figure 9.7 for the last m_{T} interval.

The features of the p–p and $\overline{\text{p}}$–$\overline{\text{p}}$ systems that can be distinguished are a drop of the correlations for $k^* \to 0\,\text{MeV/c}$ and a peak at around 20 MeV/c. The pit for 0 MeV/c is due to Pauli blocking of the identical particles and a repulsive core from the strong interaction. Given that as fermions they cannot inhabit the same state, the correlation function goes to 0 as the repulsion will deprive the region from any correlations. The peak is due to the attractive force of the strong interaction that draws pairs closer in phase space and thus creates a higher density in the same-event pair distribution.

Afterwards, the correlation function falls below unity for $80 < k^* < 100\,\text{MeV/c}$ due to the interplay of strong interaction and the repulsive Coulomb interaction between the two same-charged particles. Finally, the function goes to unity and no further final state interactions take place.

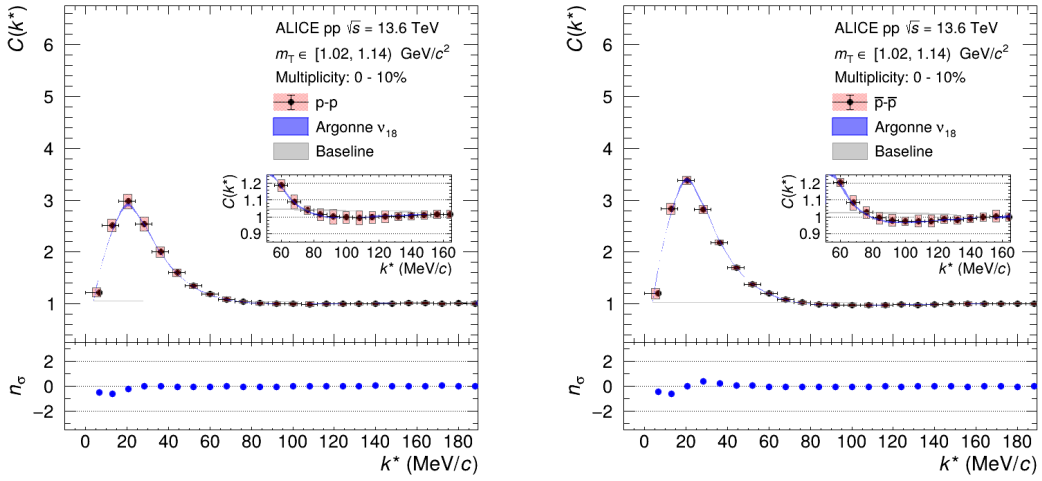

Figure 7.1: Simultaneous fits with the Argonne v_{18} potential to the p–p and $\overline{\text{p}}$–$\overline{\text{p}}$ correlation functions in the m_{T} range of [1.02, 1.14) for the multiplicity percentile of 0 to 10 %.

Comparing the multiplicity percentiles of a single m_{T} interval reveals that the magnitude of the correlations increases alongside the percentile, i.e. as the number of particles in a collision decreases. This effect is larger for the $\overline{\text{p}}$–$\overline{\text{p}}$ most likely due to the already larger initial magnitude of the function.

Increasing the average m_{T} affects the correlations in a similar fashion, as its strength increases. This results in a steeper and narrower distribution which when fitted with a

Gaussian source returns a smaller value for its width. Within a multiplicity percentile, the size shrinks in such manner that a scaling can be perceived as an exponential decrease. More about this in the later section 7.3 about the m_{T} scaling.

As a final remark, the correlation function for larger values of m_{T} and multiplicity percentile is influenced by statistical fluctuations and therefore low statistics that result in a sporadic value for the first bin of the function. Moreover, the distributions of the two highest m_{T} intervals, [1.56, 1.86) and [1.86, 2.40) GeV/c, are all missing the first bin between 0 and 8 MeV/c due to the small statistics in this region.

Fitting with the RSM

Similar to the previous fits with a Gaussian source, the fits with the RSM and the Argonne v_{18} potential are characterized by the same features. The quality of the fits, which can be seen in figure 9.8, is similar but the secret lies within the source. As explained in section 5.4, due to the consideration of resonances feeding into the particles of interest, i.e. protons or antiprotons, the underlying source function is of smaller nature. The resonances broaden the distribution and generate a tail. Therefore, the core distribution from where the primordial particles are emitted is smaller. The trend of decreasing size still prevails for increasing m_{T} and smaller event multiplicity and thus it is expected for a scaling of similar exponential decrease but shifted to lower values.

7.2 The p–Λ correlation function

The fits to the p–Λ and $\overline{\mathrm{p}}$–$\overline{\Lambda}$ correlation functions are shown in the appendix (chapter 9). As an example, figure 7.2 shows the simultaneous fit for the multiplicity percentile of 0 to 10 % in the m_{T} interval of [1.08, 1.26) MeV/c. Unlike protons, the p–Λ and $\overline{\mathrm{p}}$–$\overline{\Lambda}$ pairs do not experience from Pauli blocking and thus the mixed-event distribution is not drained from its entries in the lower k^* region. The correlation function therefore reaches its peak value for $k^* \rightarrow 0\,\mathrm{MeV/c}$. An additional difference to the previous system is the lack of Coulomb interaction because of the neutral charge of the Λ ($\overline{\Lambda}$) particle; the correlation function should not dip below unity. Unfortunately, the unique feature of the p–Λ and $\overline{\mathrm{p}}$–$\overline{\Lambda}$ correlation function, the cusp from the couple-channel dynamics, is not very pronounced in the experimental data due to the large bin width of 10 MeV/c. Nevertheless, the expected behaviour is displayed in the theoretical estimation of the fit.

The experimental correlation function, similar to the protons, suffers from a lack of statistics in the first bin, given that many of the partitions in m_{T} and multiplicity percentile are unstable in it and result in an unpredictable value. The fit however is once again dictated by the slope of the function and is thus resilient to this volatility.

Comparing the fits for a single m_{T} interval in the different multiplicities, e.g. figure 9.16, the shape of the function does not change as much as the protons. There is a slight increase which corresponds to a smaller width of the source function, and thus results in a systematic decrease of the source across the three percentiles.

Unfortunately, the increase of the m_{T} interval does not result in a smooth exponential decrease due to some unexpected properties of the experimental data. The two central

bins in m_{T}, [1.32, 1.44) and [1.44, 1.64) MeV/c, are affected by some contamination that elevates the distributions from their expected value of unity in the k^* region above 120 MeV/c. From the comparison of figure 9.16 and figure 9.18, a difference of up to 0.3 of units for the baseline can be observed for the lowest k^* values.

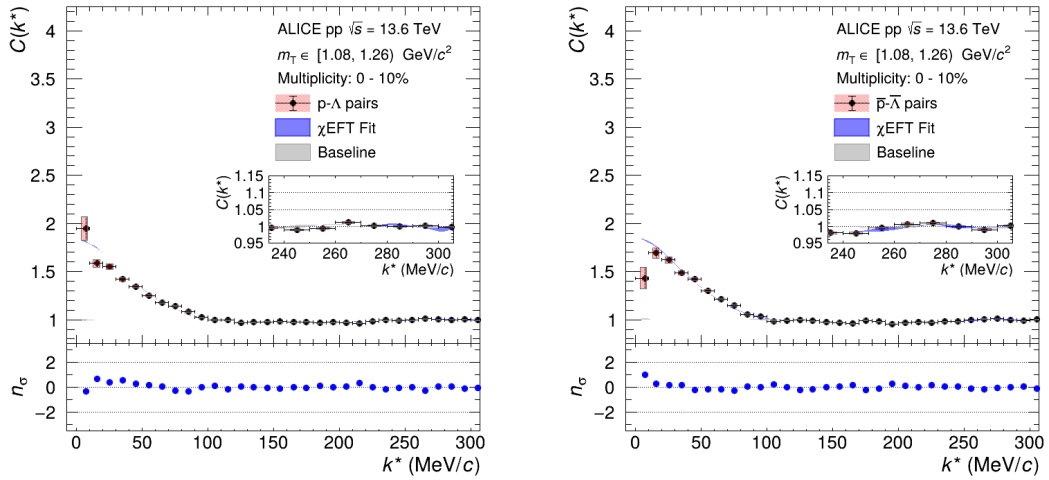

Figure 7.2: Simultaneous fits with the NLO19 potential to the p–Λ and $\overline{\mathrm{p}}$–$\overline{\Lambda}$ correlation functions in the m_{T} range of [1.08, 1.26) for the multiplicity percentile of 0 to 10 %.

7.3 The m_{T} Scaling

After many fits and much work, the size of the source function for all m_{T} intervals and multiplicity percentiles can be graphed. Figure 7.3 shows the scaling that occurs from plotting the size of the p–p and $\overline{\mathrm{p}}$–$\overline{\mathrm{p}}$ source at the weighted m_{T} value within an interval; the weight is calculated by considering the density of the p_{T} distribution. The values themselves are displayed in table 7.1. Three distinct scalings can be distinguished from the Run 3 data for either source and correspond to the three multiplicity percentiles. The gray markers denote the scaling from the Run 2 high-multiplicity analysis, which corresponds to a percentile of the 0 to 0.017 % highest multiplicity events with an average charged track multiplicity at mid-pseudorapitity of $\langle \mathrm{d}N/\mathrm{d}\eta \rangle_{|\eta|<0.5} \approx 30$ tracks. Underneath the scaling for the 0 to 10 % percentile of the Run 3 data can be found, which is marked by the red systematic uncertainties and translates to an average charged track multiplicity of $\langle \mathrm{d}N/\mathrm{d}\eta \rangle_{|\eta|<0.5} = 25.12^{+0.25}_{-0.19}$. The middle percentile, 10 to 50 %, is associated with the green systematic uncertainties in the plot and a value of $\langle \mathrm{d}N/\mathrm{d}\eta \rangle_{|\eta|<0.5} = 16.48^{+0.15}_{-0.11}$ charged tracks. The last, 50 to 100 %, is displayed with blue uncertainties and matches an average value of $\langle \mathrm{d}N/\mathrm{d}\eta \rangle_{|\eta|<0.5} = 12.33^{+0.07}_{-0.05}$. The scalings follow a distinct order related to their multiplicity. The higher the multiplicity, the larger the volume of the particle emission, thus leading to an increase in inter-particle distances. Similarly, the bigger the transverse mass, the larger the average

inter-particle momentum and thus an earlier departure from the region of emission which in turns reduces its size. As a last remark, the largest m_{T} interval appears to reach a value for which all multiplicity percentiles saturate and hint at the fact that the region of particle emission has a lower limit for its size due to the finite dimensions of particles.

Source sizes of the p–p and $\overline{\mathrm{p}}$–$\overline{\mathrm{p}}$ fits

	Effective			Core		
m_{T} [GeV/c]	0 - 10%	10 - 50%	50 - 100%	0 - 10%	10 - 50%	50 - 100%
[1.02, 1.14)	1.315(25)	1.212(26)	1.135(24)	1.126(25)	1.026(24)	0.951(23)
[1.14, 1.20)	1.269(25)	1.168(24)	1.078(24)	1.083(24)	0.985(24)	0.895(24)
[1.20, 1.26)	1.186(24)	1.101(22)	1.005(25)	1.002(23)	0.919(22)	0.824(25)
[1.26, 1.38)	1.146(24)	1.078(23)	1.008(24)	0.963(23)	0.896(22)	0.828(23)
[1.38, 1.56)	1.098(24)	1.034(22)	0.975(25)	0.915(23)	0.852(22)	0.794(24)
[1.56, 1.86)	1.026(23)	0.969(23)	0.914(30)	0.844(23)	0.776(23)	0.727(30)
[1.86, 2.40)	0.862(24)	0.815(25)	0.801(48)	0.680(24)	0.627(26)	0.601(57)

Table 7.1: Source sizes for the Gaussian and RSM source of the p–p and $\overline{\mathrm{p}}$–$\overline{\mathrm{p}}$ fits with the Argonne v_{18} potential.

Source sizes of the p–Λ and $\overline{\mathrm{p}}$–$\overline{\Lambda}$ fits

	Effective			Core		
m_{T} [GeV/c]	0 - 10%	10 - 50%	50 - 100%	0 - 10%	10 - 50%	50 - 100%
[1.08, 1.26)	1.573(3)	1.499(4)	1.468(4)	1.411(4)	1.335(14)	1.298(4)
[1.26, 1.32)	1.287(6)	1.207(4)	1.130(17)	1.115(5)	1.033(3)	0.949(18)
[1.32, 1.44)	1.061(43)	0.975(51)	0.879(40)	0.898(43)	0.807(46)	0.724(27)
[1.44, 1.65)	1.451(38)	1.444(42)	1.503(43)	1.297(40)	1.288(42)	1.351(44)
[1.65, 1.90)	1.146(5)	1.098(11)	1.098(12)	0.979(4)	0.932(12)	0.928(12)
[1.90, 4.50)	1.096(21)	1.072(11)	1.116(30)	0.936(24)	0.909(12)	0.954(31)

Table 7.2: Source sizes for the Gaussian and RSM source of the p–Λ and $\overline{\mathrm{p}}$–$\overline{\Lambda}$ fits with the NLO19 potential.

From measurements of the common baryonic source it is known that it follows a decreasing exponential function [27]. The p–p Run 2 scaling is included in the aforementioned source and displayed in the lower panel of figure 7.3 again marked by gray coloured uncertainties. For that reason a future improvement of the here presented

scalings could be the study of the dependence of the individuals as a parametrization by an exponential function. Nevertheless, the obtained scalings include a slight dip in the third bin. This imperfection might be due to the interval being associated with the switch in particle identification from TPC only to TPC and TOF, thus losing statistics from the unmatched tracks of the TPC in the TOF. Both the Gaussian source and the RSM source follow the same tendencies in all bins but are shifted by $\approx 0.05\,\mathrm{fm}$ each scaling from the preceding in percentile.

For the p–Λ and $\overline{\mathrm{p}}$–$\overline{\Lambda}$ the previously mentioned issue with the two middle m_{T} intervals becomes apparent when comparing the values in table 7.2 and figure 7.4. Once more the gray markers denote the Run 2 high-multiplicity scaling and the Run 3 scalings are denoted by the same colour scheme as for the proton pairs. For the Run 3 scalings, the third bin is consistently lower than expected as it lies beneath the fifth. The reverse applies for the fourth bin as it consistently lies above the second. As previously mentioned, this is due to the contamination in the two m_{T} intervals and affects them, due to the interplay of source and interaction, in such sporadic manner. Regardless, all bins fluctuate around the Run 2 scaling and, while there is a clear order of the sizes from different multiplicities, the overall result cannot be said to be conclusive as it is evidently; the multiplicity of the Run 2 data is larger and thus its scaling should consistently be larger than the rest. One of the reasons for this could be the λ parameters as they were taken from the Run 2 analysis and therefore should not be representative for the Run 3 feed-down contributions. Moreover, the genuine contribution is likely to be overestimated. A computation of the λ parameters from template fits and the calculation of them as a function of k^* should allow for a more correct extraction of the source sizes. Additionally, stricter selection cuts could mitigate the contamination in the middle bins and result in a scaling similar to that of Run 2.

7.4 Reid Potentials

As a final remark, a comparison of the p–p and $\overline{\mathrm{p}}$–$\overline{\mathrm{p}}$ correlation function fits is shown in here for the Argonne v_{18}, Reid68, and Reid93 potentials. To this end, the prior introduced routine for fitting is redone with a fixed baseline, fitted beforehand. This allows to have equal terms for all models. The result of this procedure is shown in table 7.3 for the Argonne v_{18} and in table 7.4 for the Reid potentials.

Fitting the baseline first and later the correlation functions for the Argonne potential results in a difference of $\approx 1\,\%$ for the radii. The pre-fitted is consistently smaller than the free-fit baseline fit. Comparing this to the Reid93 potential yields a smaller difference, as they consistently lie within the uncertainties. The Reid68 potential on the other hand, is systematically above the other two. This is within expectation due to the missing $^1\mathrm{D}_3$ partial wave and the different phase shift in the $^3\mathrm{P}_2$ wave, as explained in chapter 6.2.2, which results in a weaker attractive force for the strong interaction, and thus, an inability to reach the peak of the correlation function. This can also be observed in figure 7.5, where the pre-fitted baseline fit with the Argonne v_{18} potential is displayed alongside the fit with the Reid93 potential in the left panel, and with the Rei68 on the right. While the former is almost indistinguishable, as both fits lie on top

of each other, the latter is made out of two separate bands: Argonne v_{18} in blue and below Rei68 in red. The baseline obtains a small constant shift due to the normalization $\mathcal{N}$ being a common variable for both model and baseline. Nevertheless, the difference is substantial.

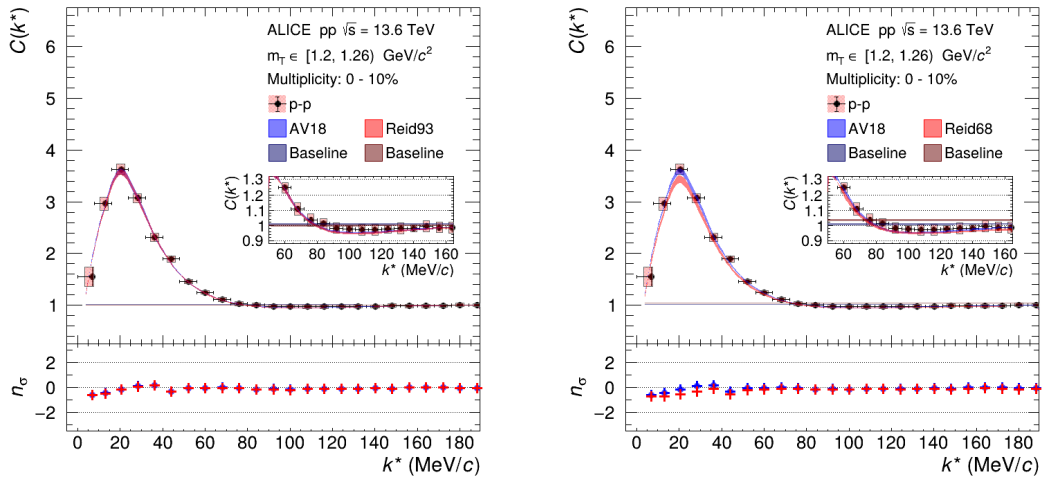

Figure 7.5: Simultaneous fits with the Argonne v_{18} potential to the p–p and $\overline{\text{p}}$–$\overline{\text{p}}$ correlation functions in the m_{T} range of [1.20, 1.26) for the multiplicity percentile of 0 to 10 %.

Source sizes of the Argonne v_{18} potential

	Effective			Core		
m_{T} [GeV/c]	0 - 10%	10 - 50%	50 - 100%	0 - 10%	10 - 50%	50 - 100%
[1.02, 1.14)	1.273(24)	1.166(24)	1.109(23)	1.085(23)	0.981(23)	0.926(23)
[1.14, 1.20)	1.233(23)	1.135(23)	1.032(23)	1.048(22)	0.952(22)	0.849(23)
[1.20, 1.26)	1.164(23)	1.084(21)	0.983(22)	0.948(22)	0.904(20)	0.803(22)
[1.26, 1.38)	1.122(21)	1.052(21)	0.971(21)	0.940(21)	0.872(20)	0.794(21)
[1.38, 1.56)	1.068(22)	1.004(20)	0.949(23)	0.887(21)	0.824(20)	0.770(23)
[1.56, 1.86)	1.002(22)	0.922(21)	0.874(26)	0.821(21)	0.741(21)	0.686(27)
[1.86, 2.40)	0.828(23)	0.758(25)	0.667(72)	0.645(25)	0.565(30)	0.461(54)

Table 7.3: Source sizes for the Gaussian and RSM source of the p–p and $\overline{\text{p}}$–$\overline{\text{p}}$ fits with the Argonne v_{18} potential and a pre-fitted baseline.

Source sizes for the Reid potentials

	Reid93			Reid68		
m_{T} [GeV/c]	0 - 10%	10 - 50%	50 - 100%	0 - 10%	10 - 50%	50 - 100%
[1.02, 1.14)	1.276(24)	1.169(24)	1.111(23)	1.332(23)	1.228(23)	1.177(22)
[1.14, 1.20)	1.237(24)	1.139(23)	1.035(23)	1.300(23)	1.205(22)	1.103(23)
[1.20, 1.26)	1.170(23)	1.088(20)	0.988(22)	1.261(26)	1.177(24)	1.069(25)
[1.26, 1.38)	1.126(21)	1.055(21)	0.976(20)	1.212(24)	1.142(23)	1.063(28)
[1.38, 1.56)	1.071(22)	1.006(21)	0.950(23)	1.157(24)	1.095(22)	1.043(26)
[1.56, 1.86)	1.005(22)	0.925(21)	0.877(26)	1.089(23)	1.009(23)	0.958(29)
[1.86, 2.40)	0.832(23)	0.762(26)	0.686(82)	0.909(24)	0.836(25)	0.641(79)

Table 7.4: Source sizes for the Gaussian source of the p–p and $\overline{\mathrm{p}}$–$\overline{\mathrm{p}}$ fits with the Reid93 and Reid68 potentials and a pre-fitted baseline.

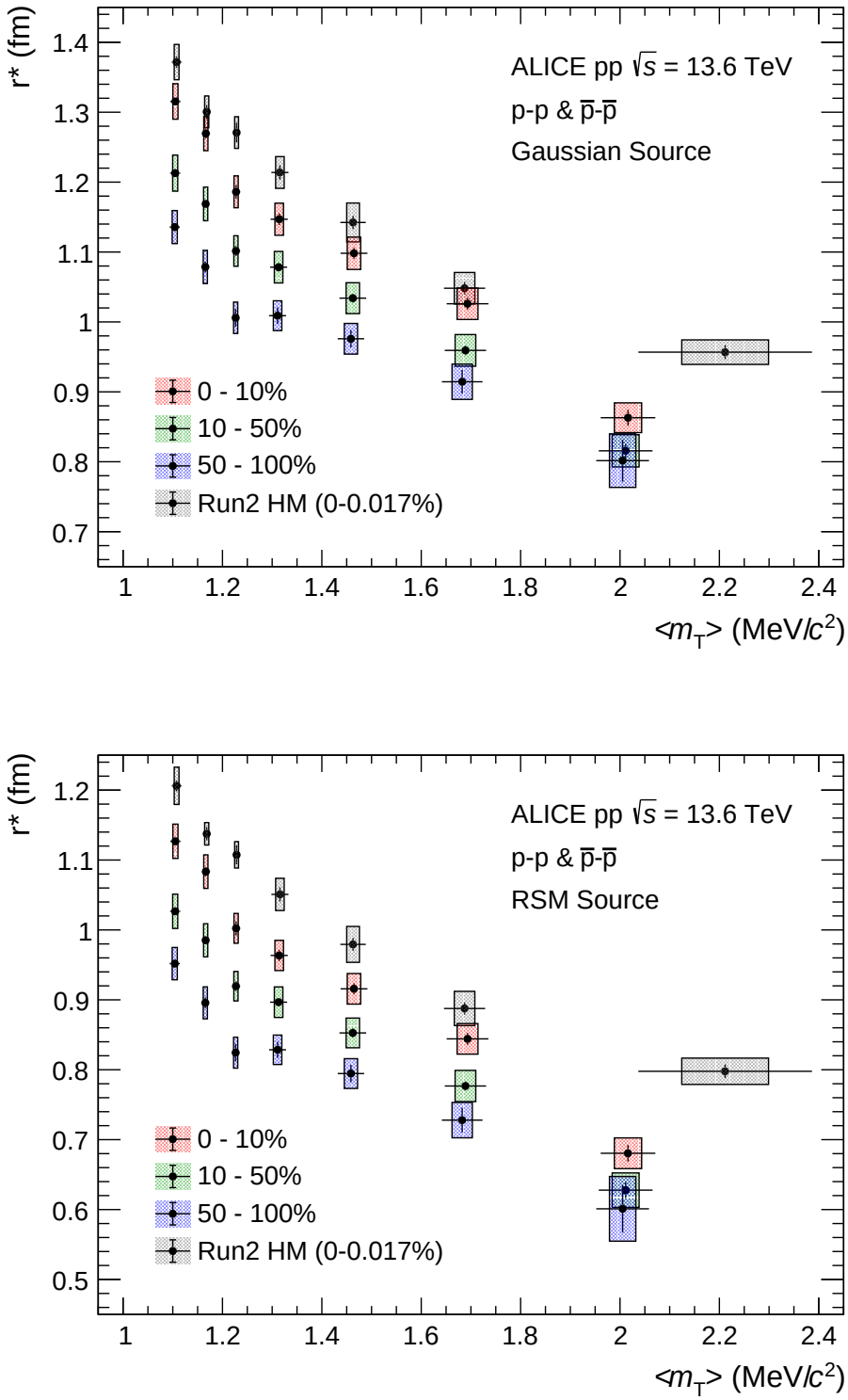

Figure 7.3: The p–p m_{T} scaling for the effective Gaussian source (top panel) and the core RSM source (bottom panel) separated into the three multiplicity percentiles.

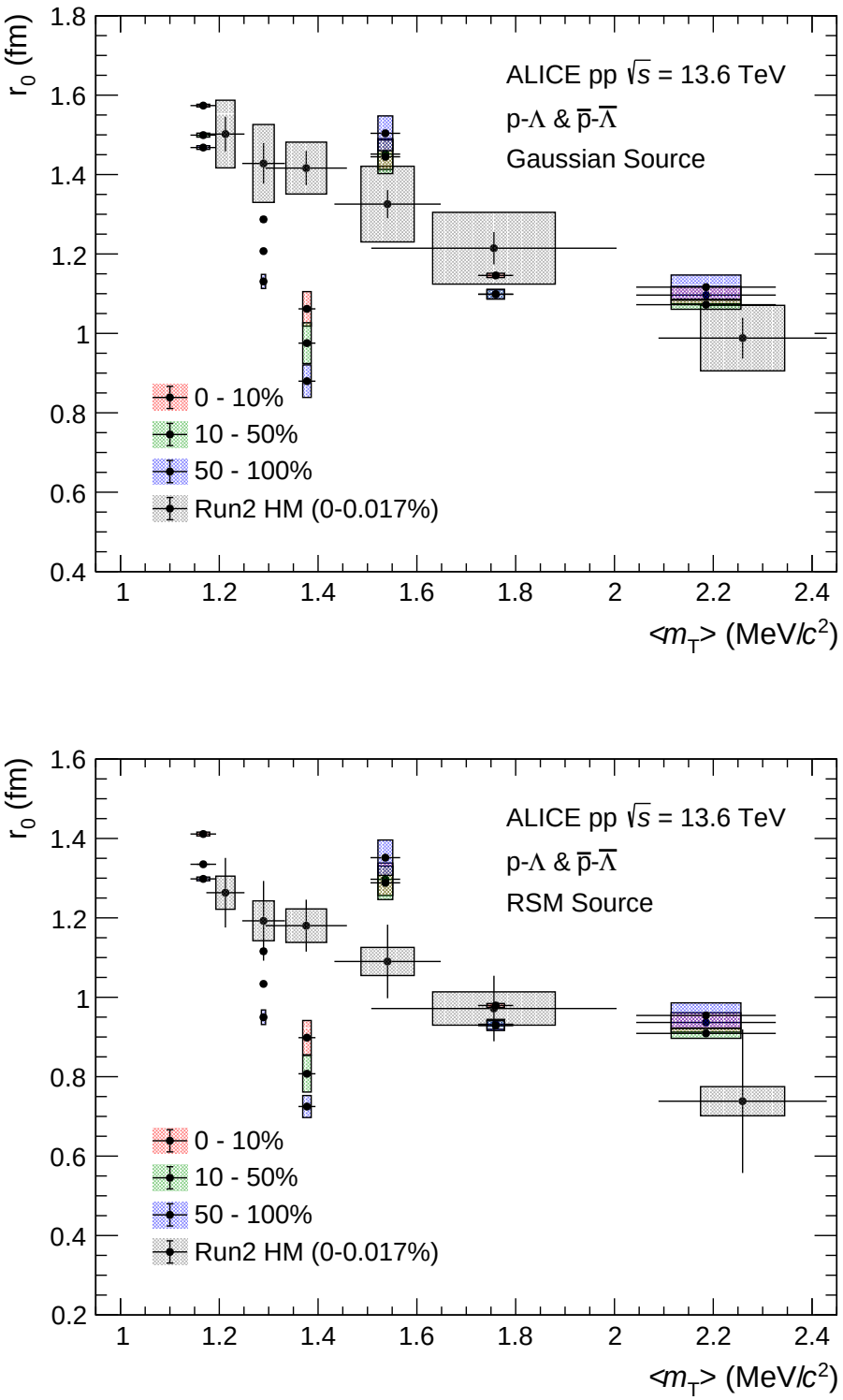

Figure 7.4: The p–Λ m_{T} scaling for the effective Gaussian source (top panel) and the core RSM source (bottom panel) separated into the three multiplicity percentiles.

8 Summary and Outlook

In this work the correlation function and, specifically, the particle emitting source was analysed differentially in transverse mass and event multiplicity. This was made possible by the large statistics obtained in the Run 3 data-taking period of the LHC. The continuous readout of the upgraded ALICE detector allowed for unprecedented precision, which was made accessible by the O^2 Project and the FemtoDream framework. The conclusion of which were the partition of the same-event and mixed-event pair distributions in multiple multiplicity percentiles. A further split was included in the form of m_T intervals. A total of seven bins for the p–p and $\overline{p}$–$\overline{p}$ system and six for the p–Λ and $\overline{p}$–$\overline{\Lambda}$ which resulted in distinct m_T scalings for the size of the source; one for each multiplicity class. The pair distributions for the p–p and $\overline{p}$–$\overline{p}$ correlation functions were well selected and the fitting worked as intended, which was performed as a simultaneous fit to both systems. To this end, the resonance feed-down contributions were controlled by template Monte Carlo fits to the two-dimensional DCA distribution. Combined with the purity of the particles, k^* dependent λ parameters were obtained and used to weight the individual contributions. Additionally, the RSM was used to examine the size of the core particle emitting source from where primordial particles originate. In this context it was shown that the m_T scaling follows a clear order dependent on the average charged-track multiplicity and saturate for larger values of m_T due to the finite size of particles.

Unfortunately, the p–Λ and $\overline{p}$–$\overline{\Lambda}$ were plagued by an unconstrained background contamination and thus the resulting scaling was not smooth. For future reference, an improvement on the selection cuts might help mitigate the contamination and the acquisition of purpose-built Monte Carlo simulations could be used to compute k^* dependent λ parameters for the Λ and $\overline{\Lambda}$ particles. Furthermore, a sideband analysis could additionally help mitigate the background. Those improvements could then be used to analyse the core source distribution of the system and compare it to the protons to investigate the and extend the common m_T scaling of the source.

Lastly, from the comparison of the fits with different potentials it was made apparent that interactions modelled by other potentials can be compatible with the typically used Argonne v_{18} potential. Accordingly, including those as a variation to the fitting procedure could be used in future studies to better compute the total and systematic uncertainty.

9 Appendix

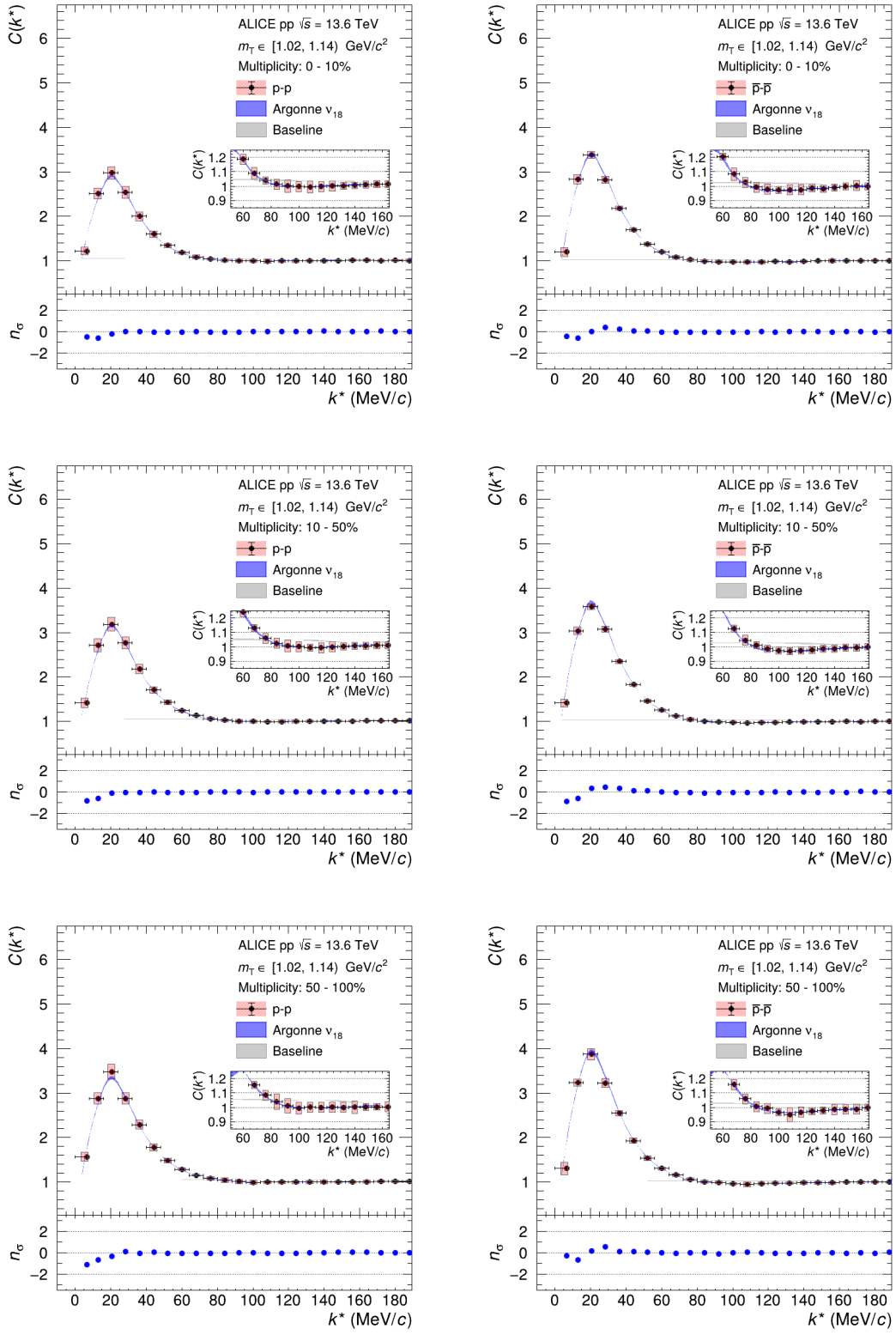

Figure 9.1: Simultaneous fits to the p–p and $\overline{\text{p}}$–$\overline{\text{p}}$ correlation functions with the Argonne v_{18} potential in the m_{T} range of [1.02, 1.14) GeV/c^2.

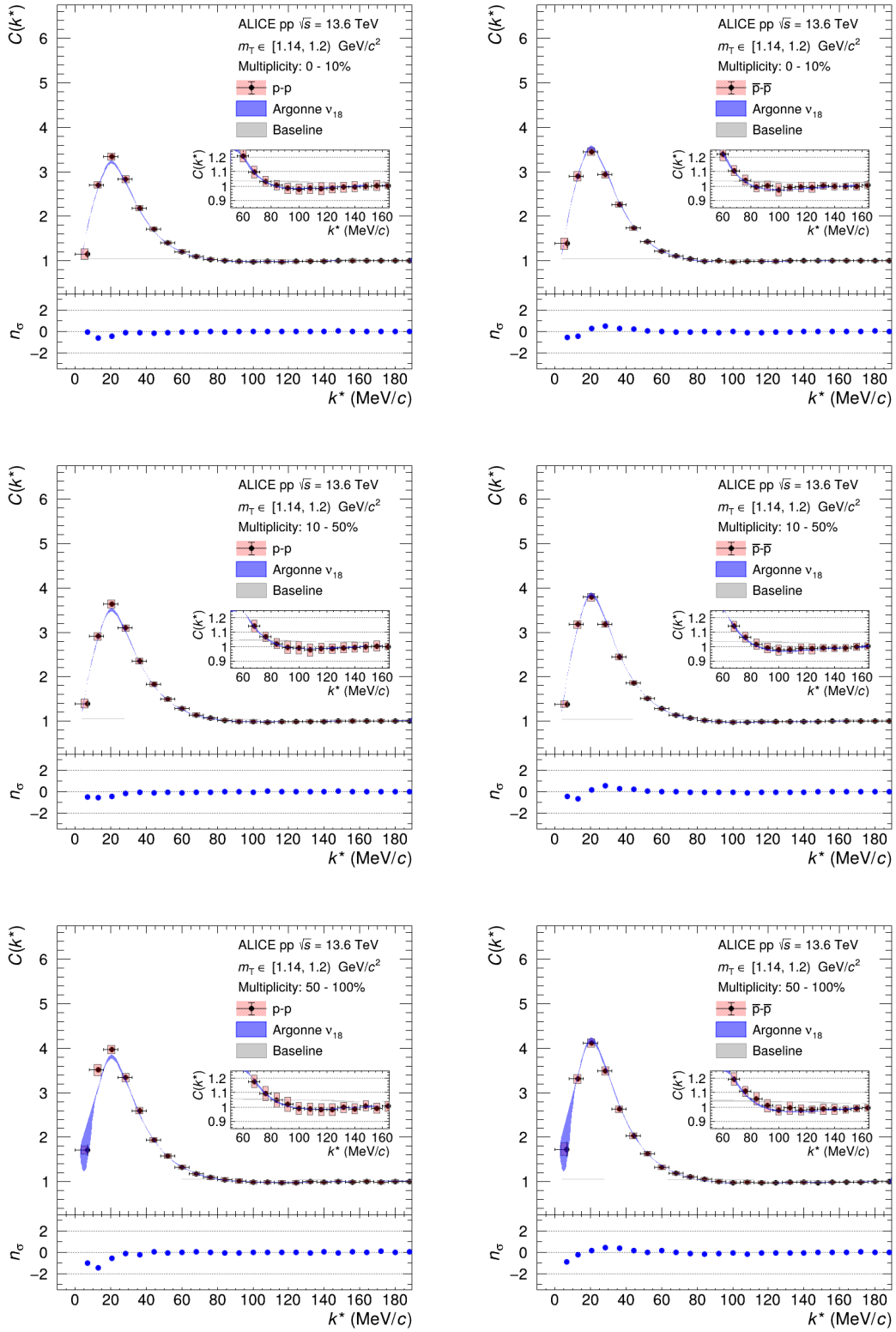

Figure 9.2: Simultaneous fits to the p–p and $\overline{\text{p}}$–$\overline{\text{p}}$ correlation functions with the Argonne v_{18} potential in the m_{T} range of [1.14, 1.20) GeV/c^2.

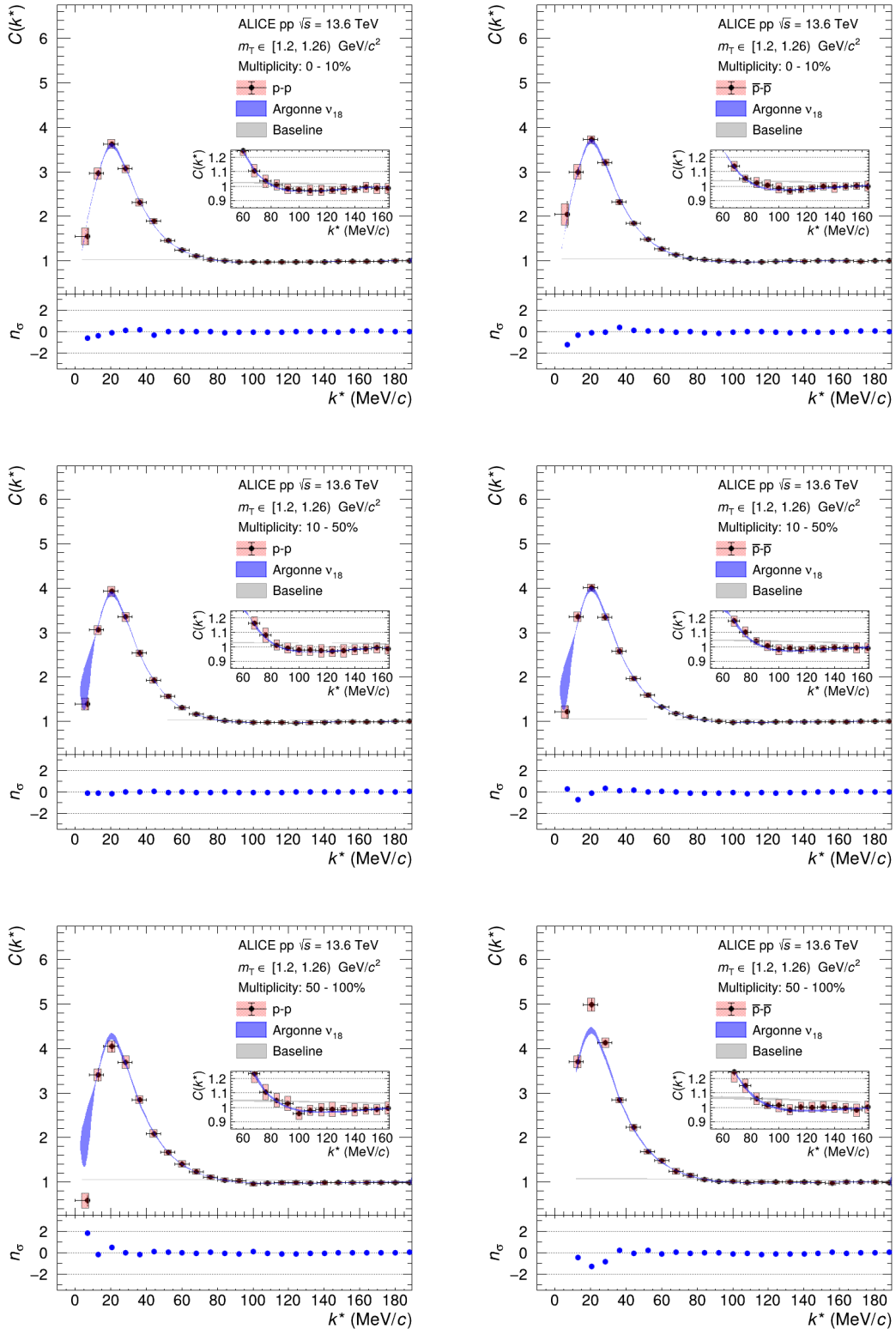

Figure 9.3: Simultaneous fits to the p–p and $\overline{\text{p}}$–$\overline{\text{p}}$ correlation functions with the Argonne v_{18} potential in the m_{T} range of [1.20, 1.26) GeV/c^2.

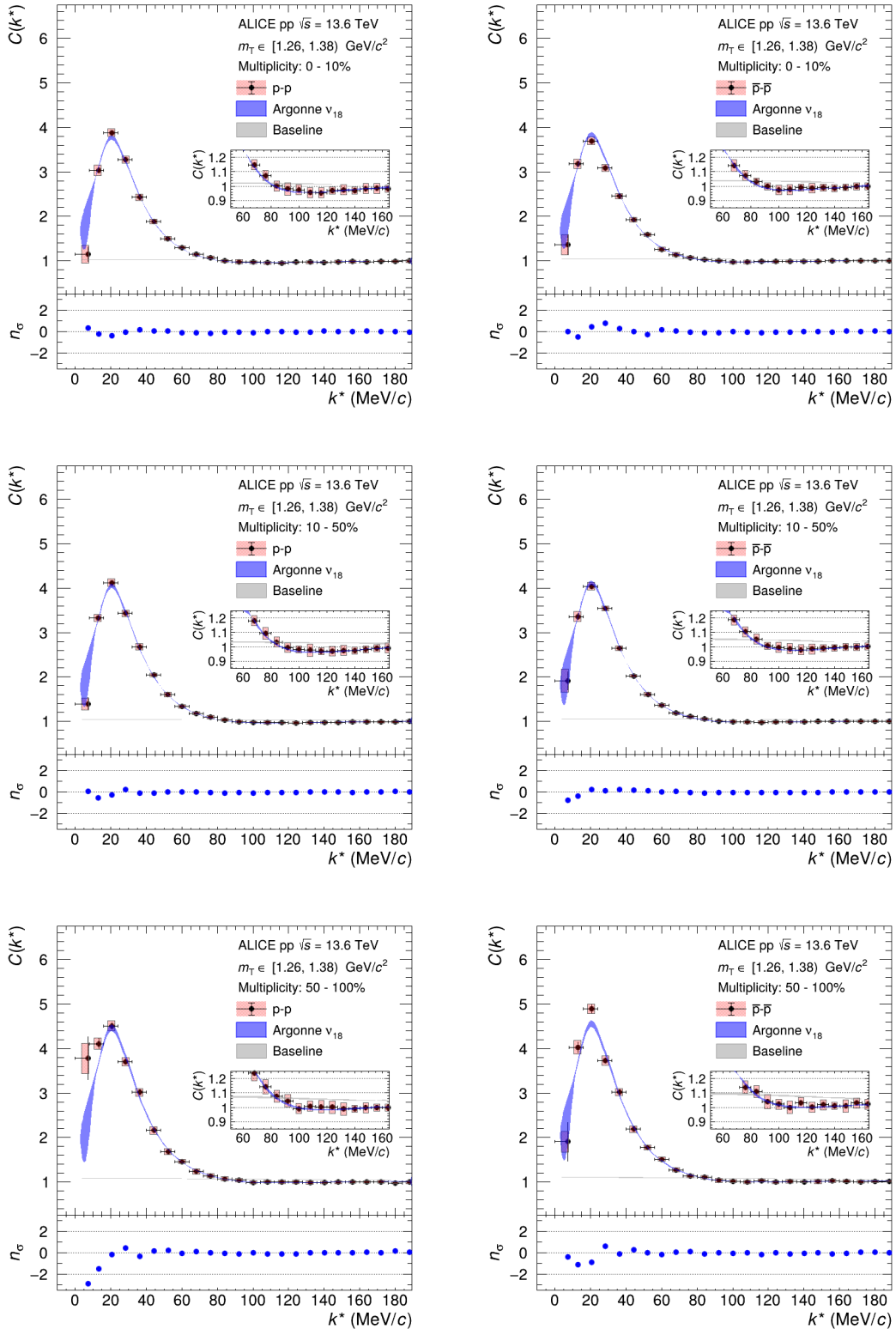

Figure 9.4: Simultaneous fits to the p–p and $\overline{\text{p}}$–$\overline{\text{p}}$ correlation functions with the Argonne v_{18} potential in the m_{T} range of [1.26, 1.38) GeV/c^2.

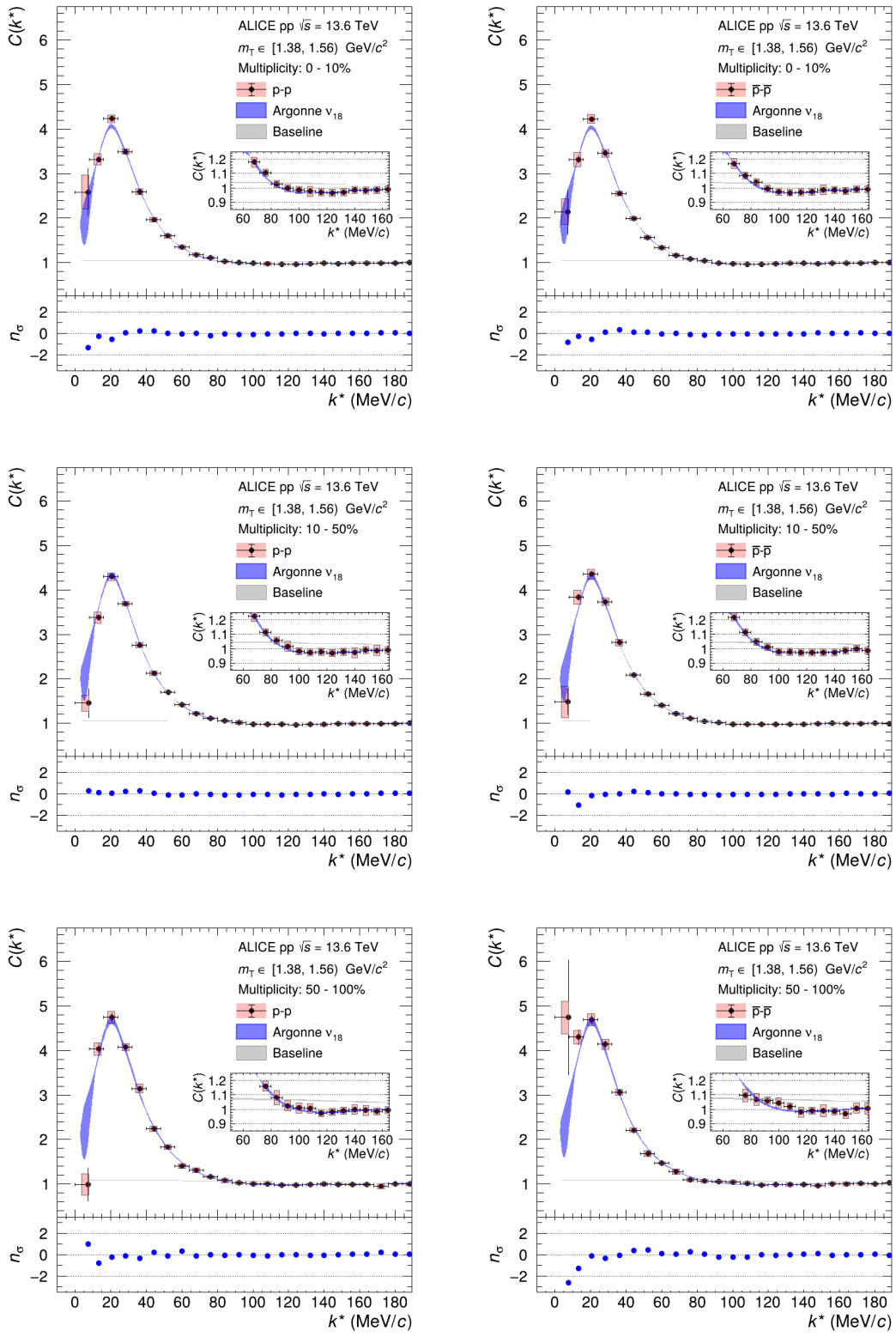

Figure 9.5: Simultaneous fits to the p–p and $\overline{\text{p}}$–$\overline{\text{p}}$ correlation functions with the Argonne v_{18} potential in the m_{T} range of [1.38, 1.56) GeV/c^2.

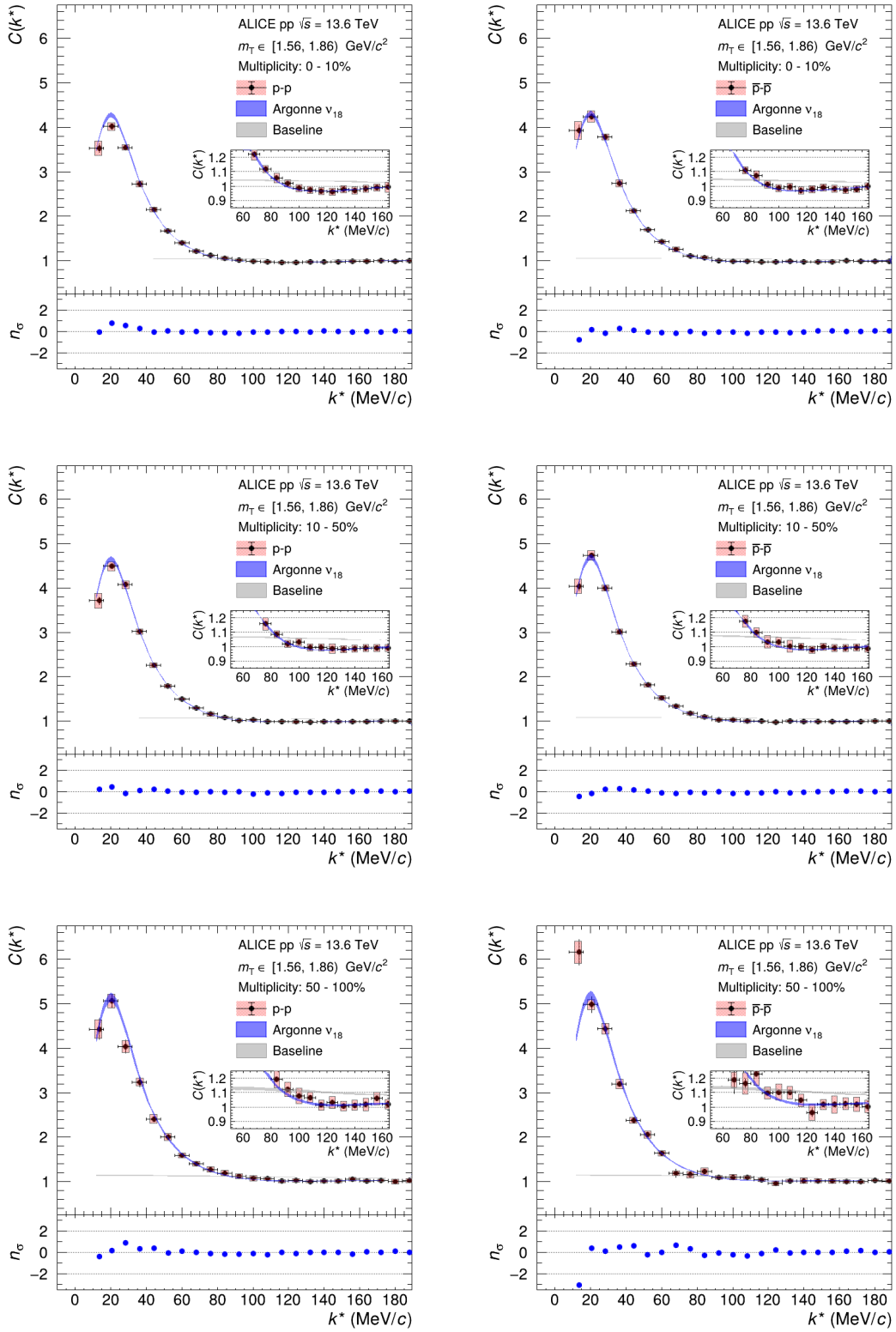

Figure 9.6: Simultaneous fits to the p–p and $\overline{\text{p}}$–$\overline{\text{p}}$ correlation functions with the Argonne v_{18} potential in the m_{T} range of [1.56, 1.86) GeV/c^2.

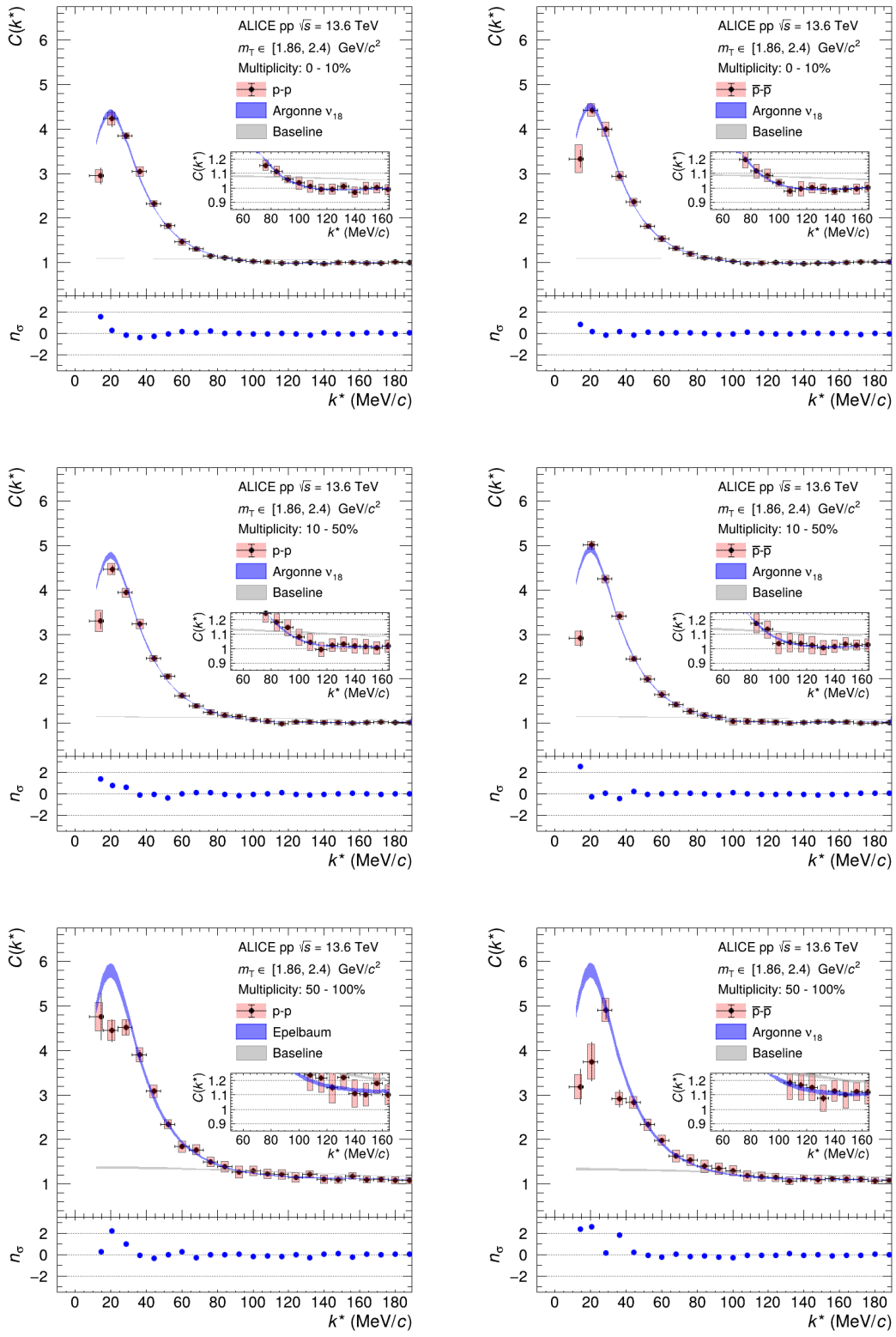

Figure 9.7: Simultaneous fits to the p–p and $\overline{\text{p}}$–$\overline{\text{p}}$ correlation functions with the Argonne v_{18} potential in the m_{T} range of [1.86, 2.40) GeV/c^2.

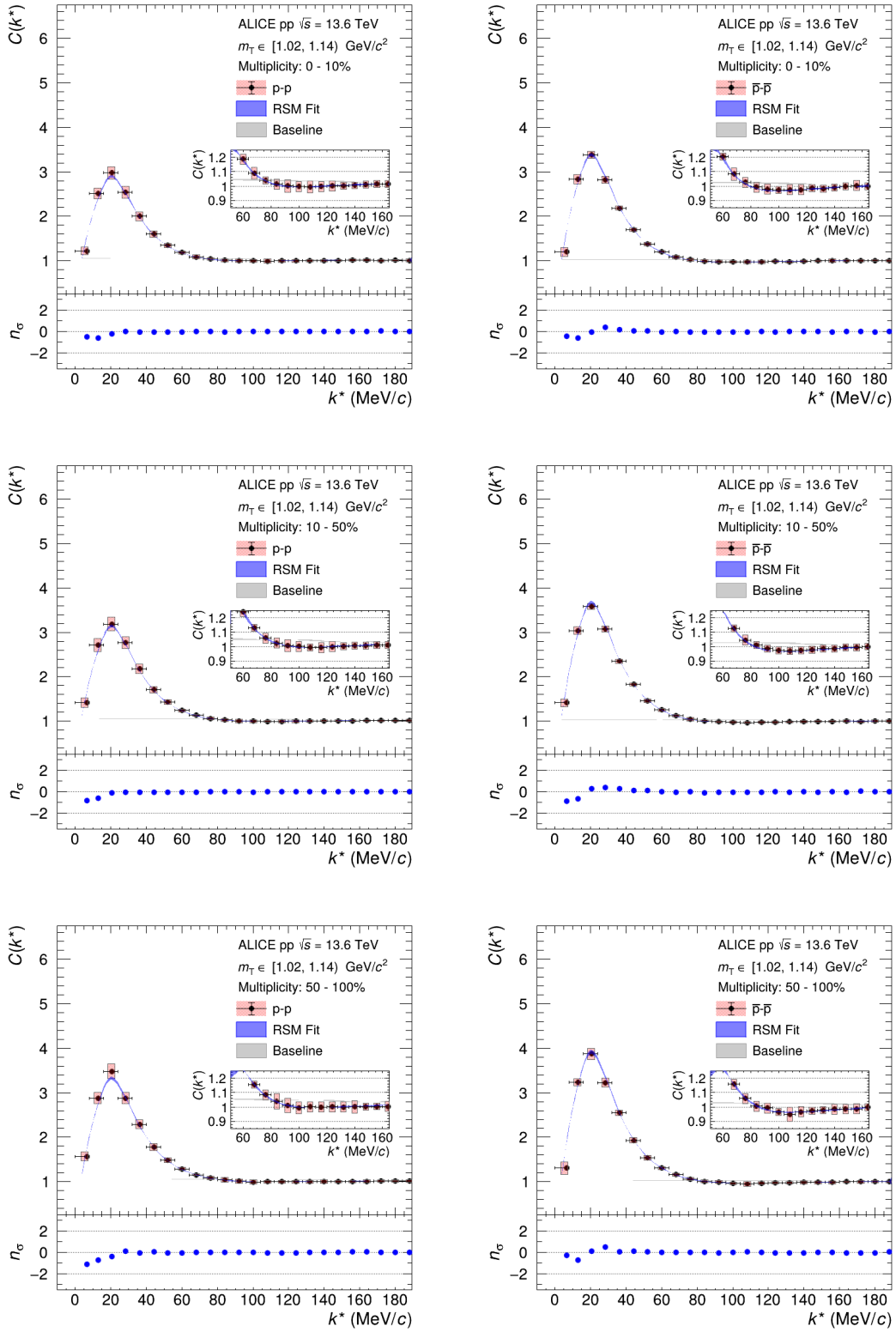

Figure 9.8: Simultaneous fits to the p–p and $\overline{p}$–$\overline{p}$ correlation functions with the RSM and the Argonne v_{18} potential in the m_T range of [1.02, 1.14) GeV/c^2.

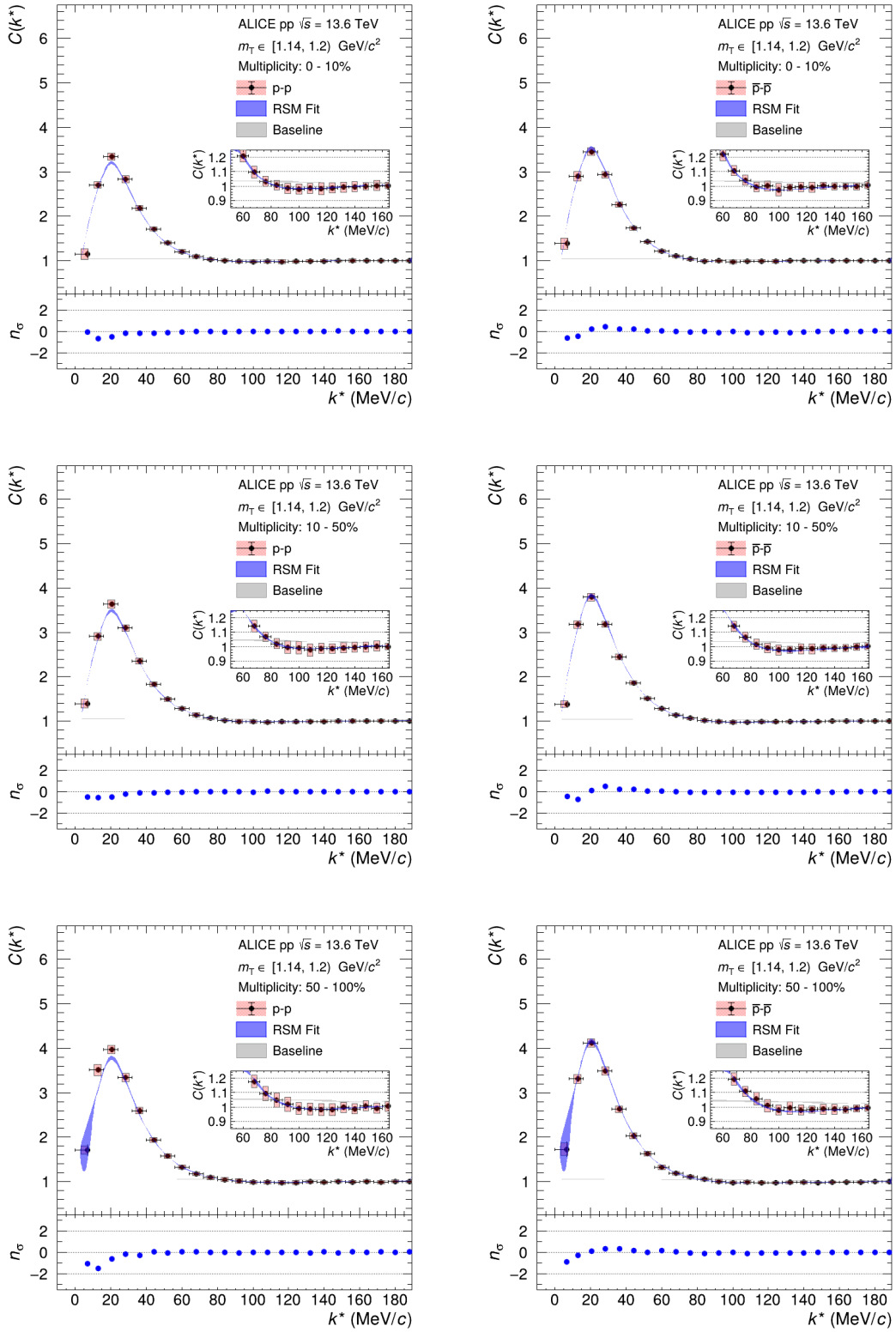

Figure 9.9: Simultaneous fits to the p–p and $\overline{p}$–$\overline{p}$ correlation functions with the RSM and the Argonne v_{18} potential in the m_T range of [1.14, 1.20) GeV/c^2.

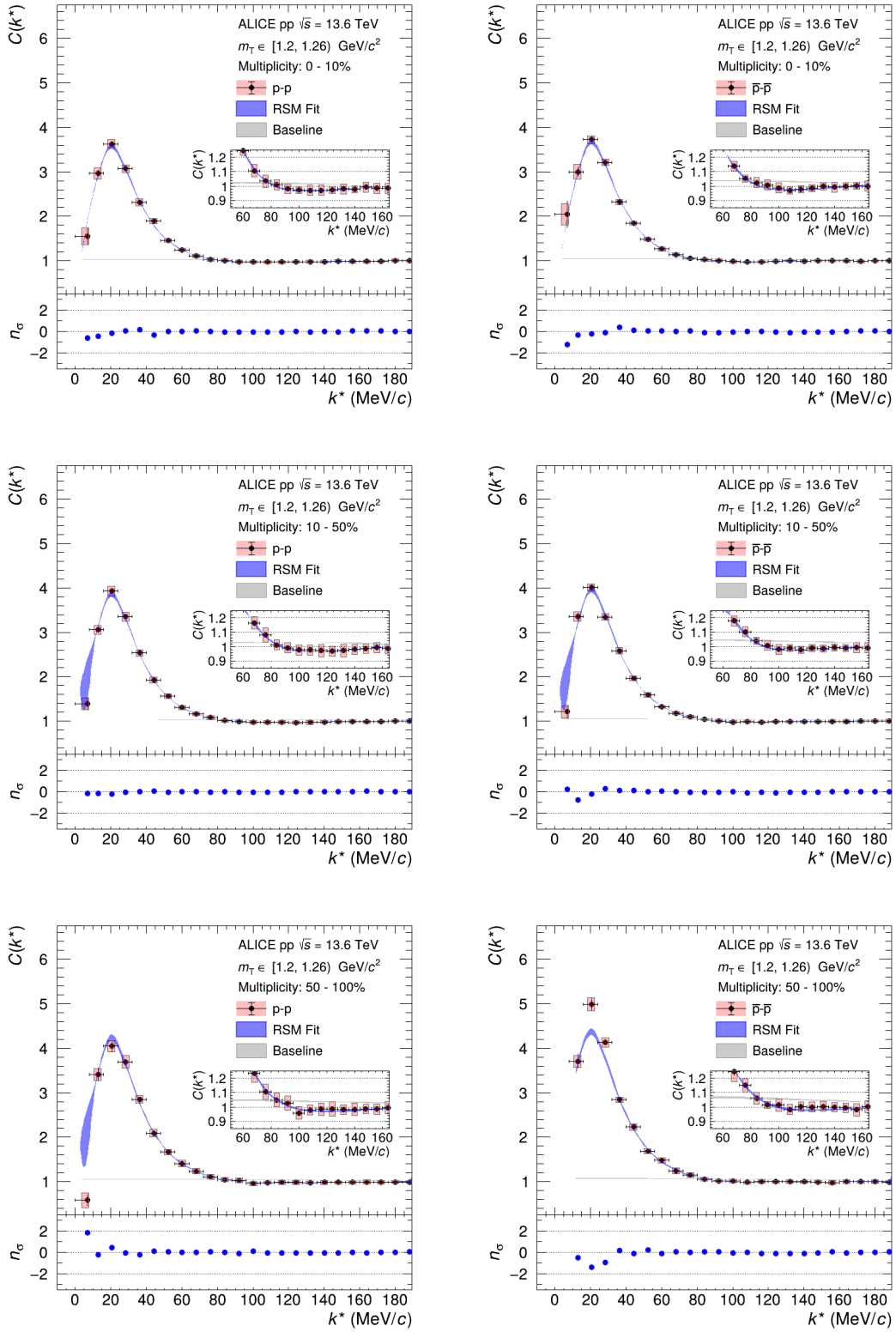

Figure 9.10: Simultaneous fits to the p–p and $\overline{\text{p}}$–$\overline{\text{p}}$ correlation functions with the RSM and the Argonne v_{18} potential in the m_{T} range of [1.20, 1.26) GeV/c^2.

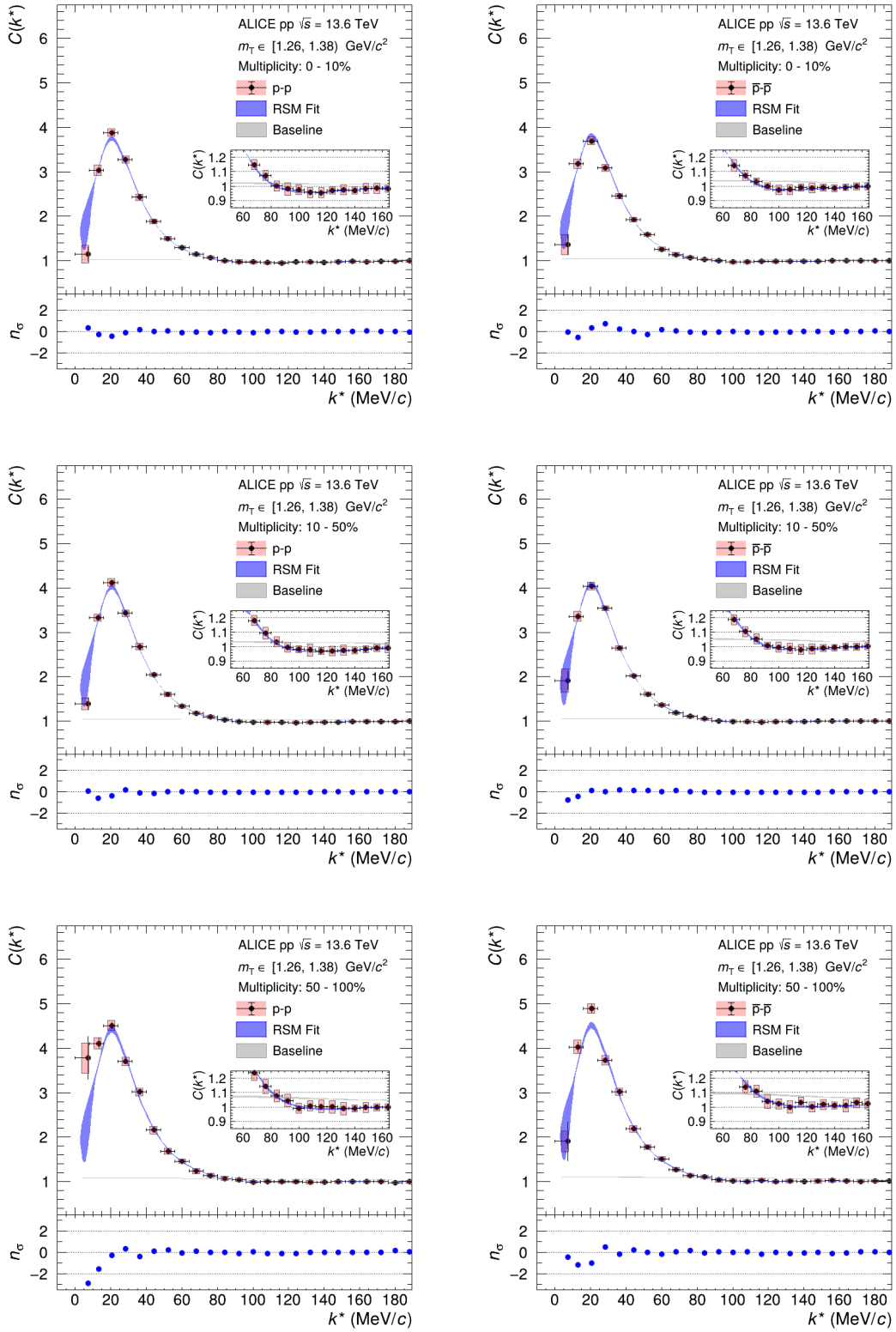

Figure 9.11: Simultaneous fits to the p–p and $\overline{p}$–$\overline{p}$ correlation functions with the RSM and the Argonne v_{18} potential in the m_T range of [1.26, 1.38) GeV/c^2.

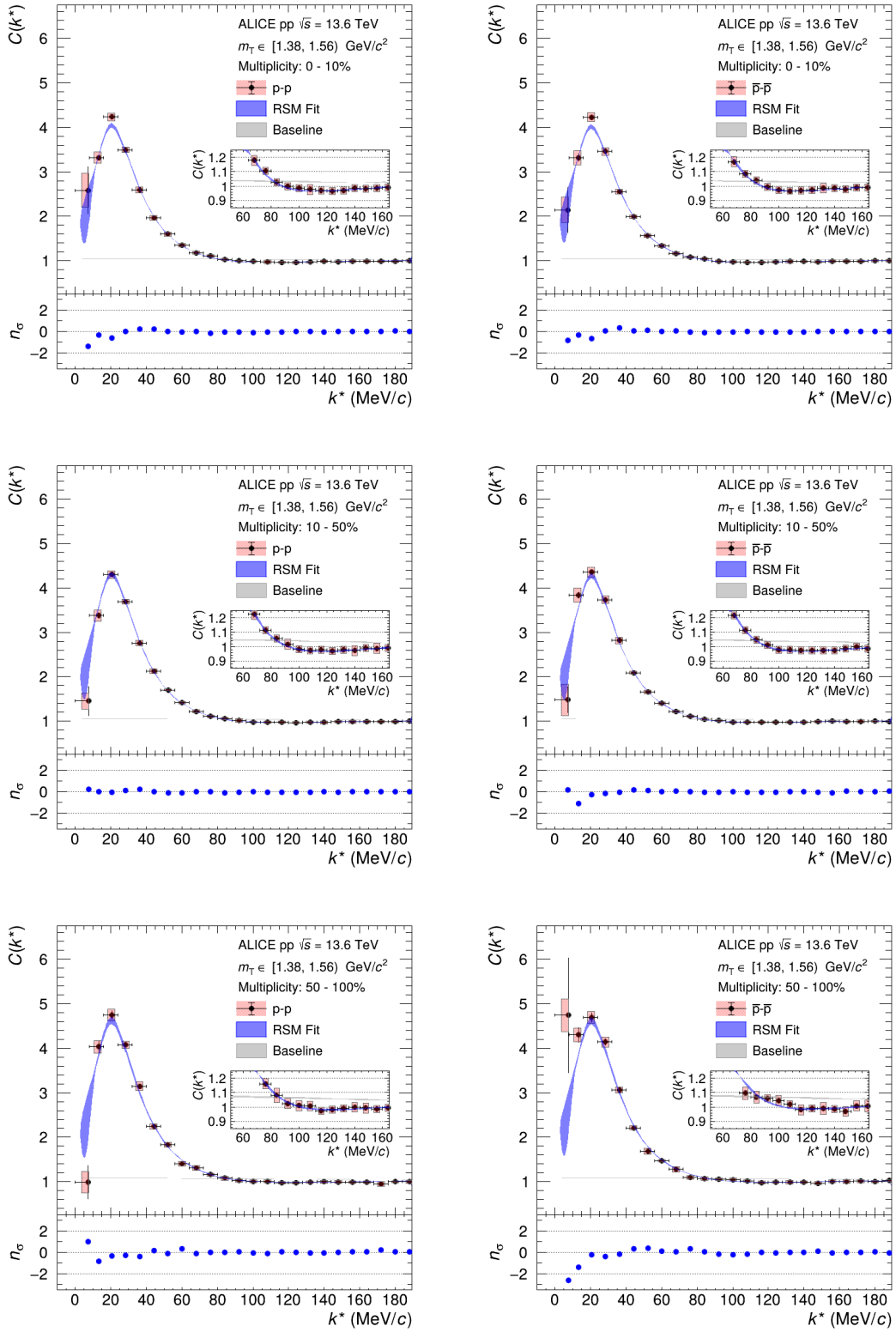

Figure 9.12: Simultaneous fits to the p–p and $\overline{\text{p}}$–$\overline{\text{p}}$ correlation functions with the RSM and the Argonne v_{18} potential in the m_{T} range of [1.38, 1.56) GeV/c^2.

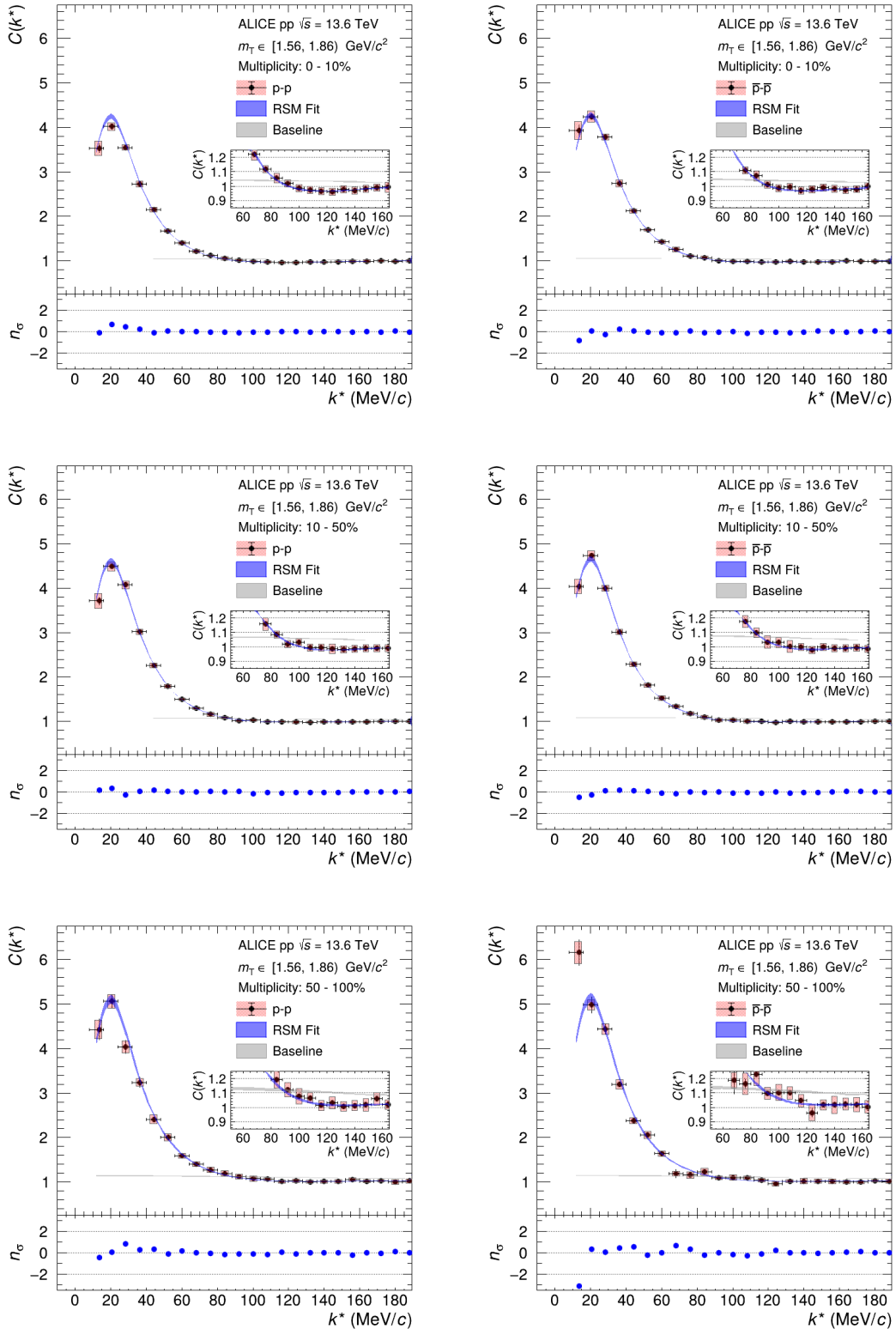

Figure 9.13: Simultaneous fits to the p–p and $\overline{\text{p}}$–$\overline{\text{p}}$ correlation functions with the RSM and the Argonne v_{18} potential in the m_{T} range of [1.56, 1.86) GeV/c^2.

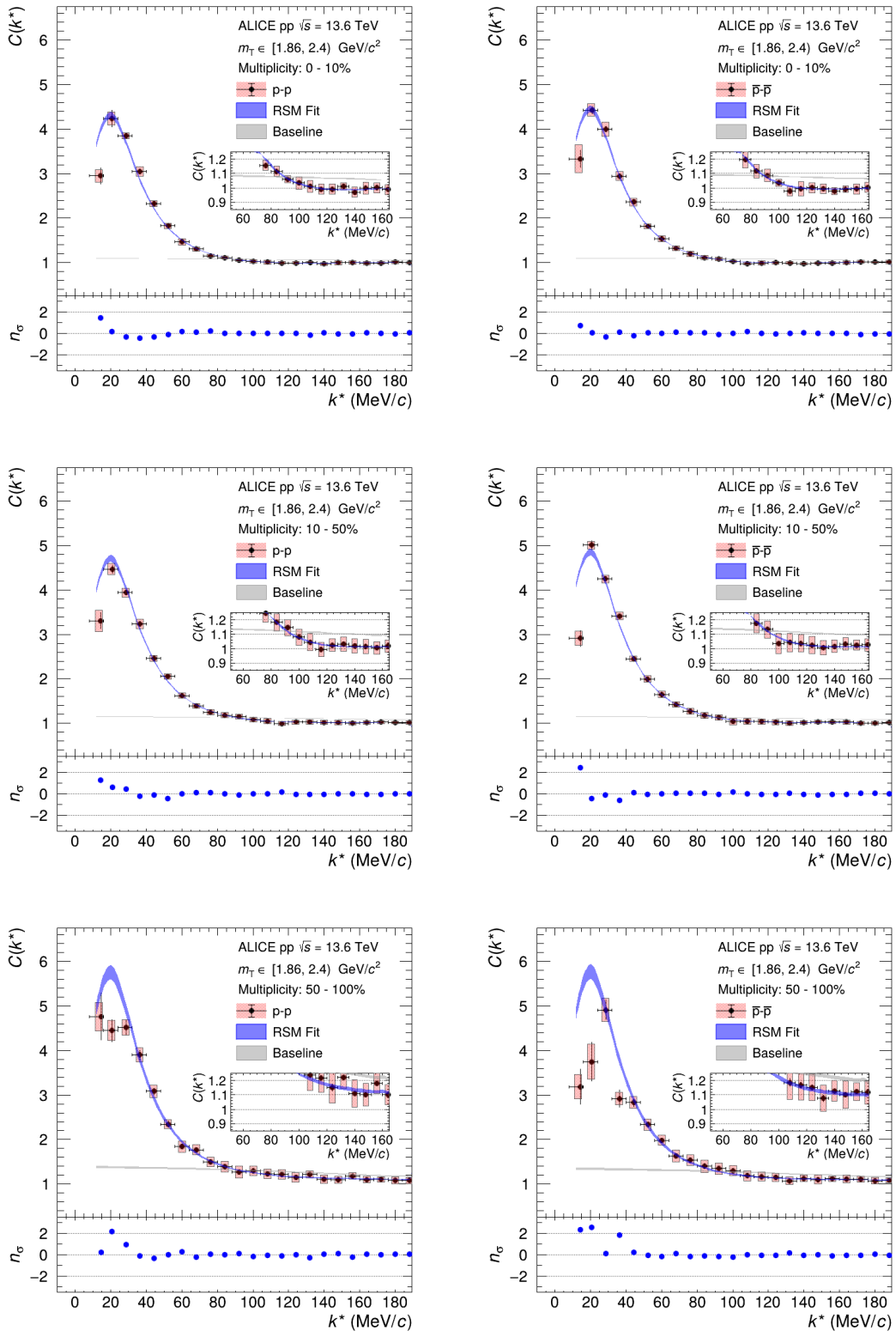

Figure 9.14: Simultaneous fits to the p–p and $\overline{p}$–$\overline{p}$ correlation functions with the RSM and the Argonne v_{18} potential in the m_T range of [1.86, 2.40) GeV/c^2.

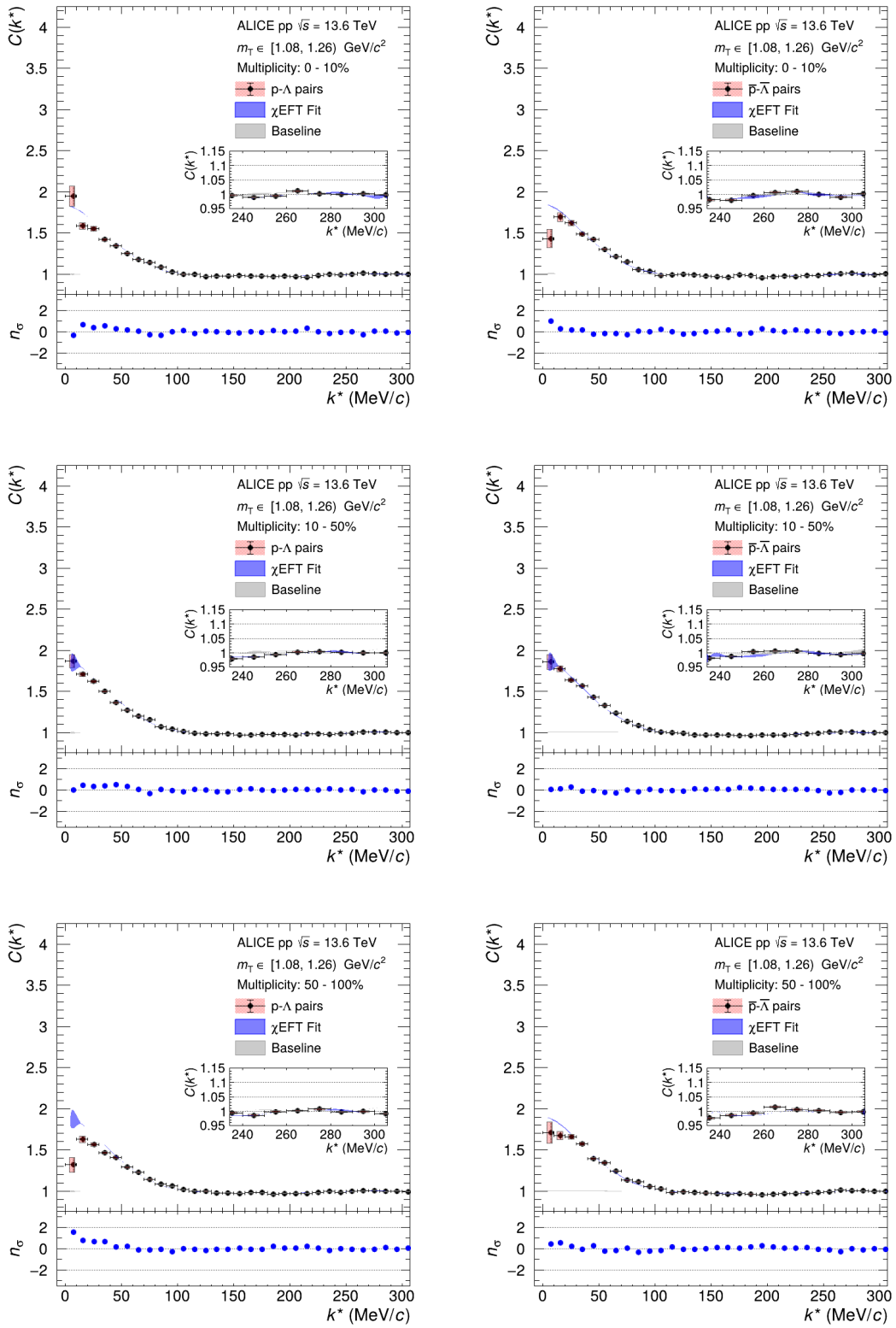

Figure 9.15: Simultaneous fits to the p–Λ and $\overline{\text{p}}$–$\overline{\Lambda}$ correlation functions with the NLO19 potential in the m_T range of [1.08, 1.26) GeV/c^2.

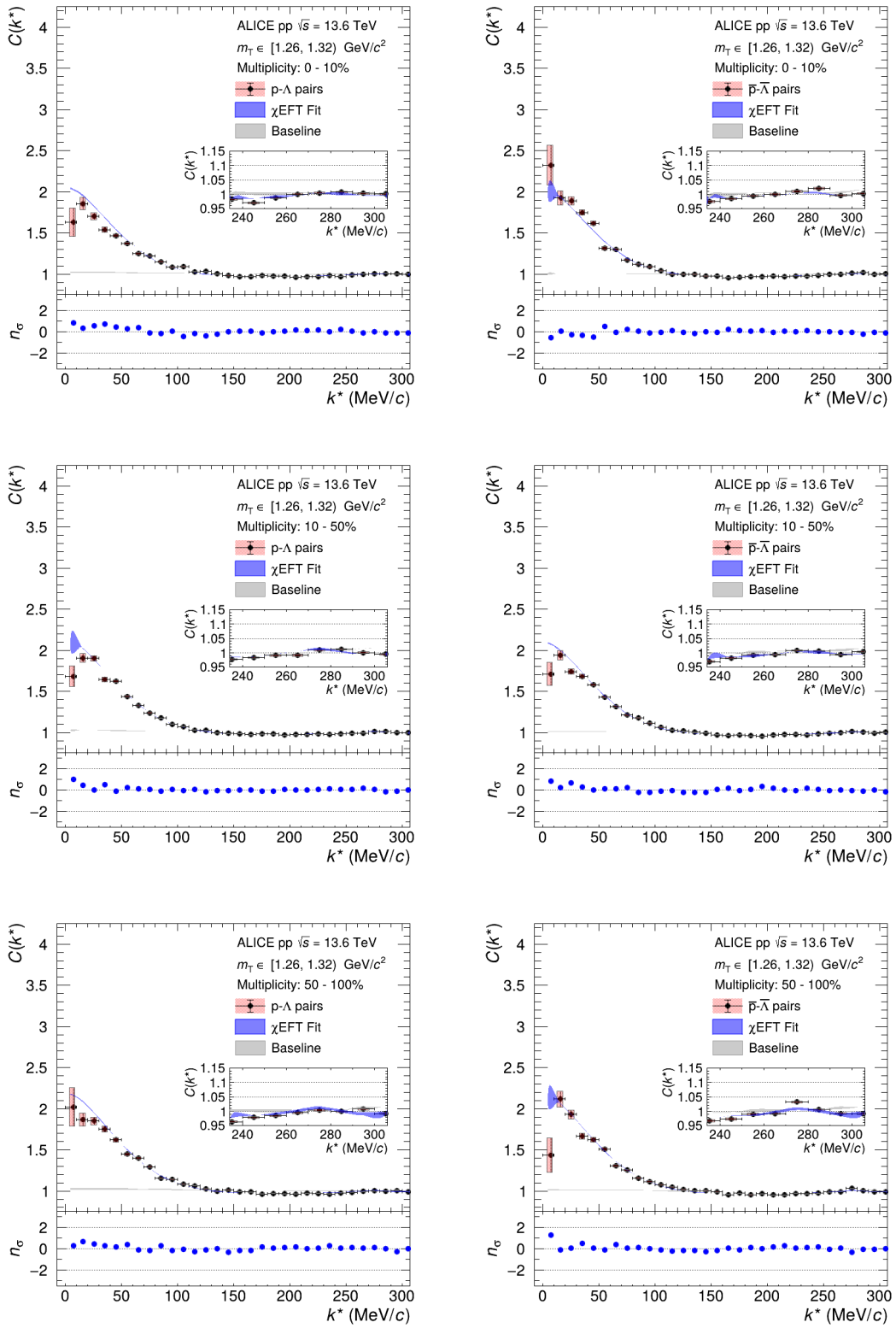

Figure 9.16: Simultaneous fits to the p–Λ and $\overline{\text{p}}$–$\overline{\Lambda}$ correlation functions with the NLO19 potential in the m_{T} range of [1.26, 1.32) GeV/c^2.

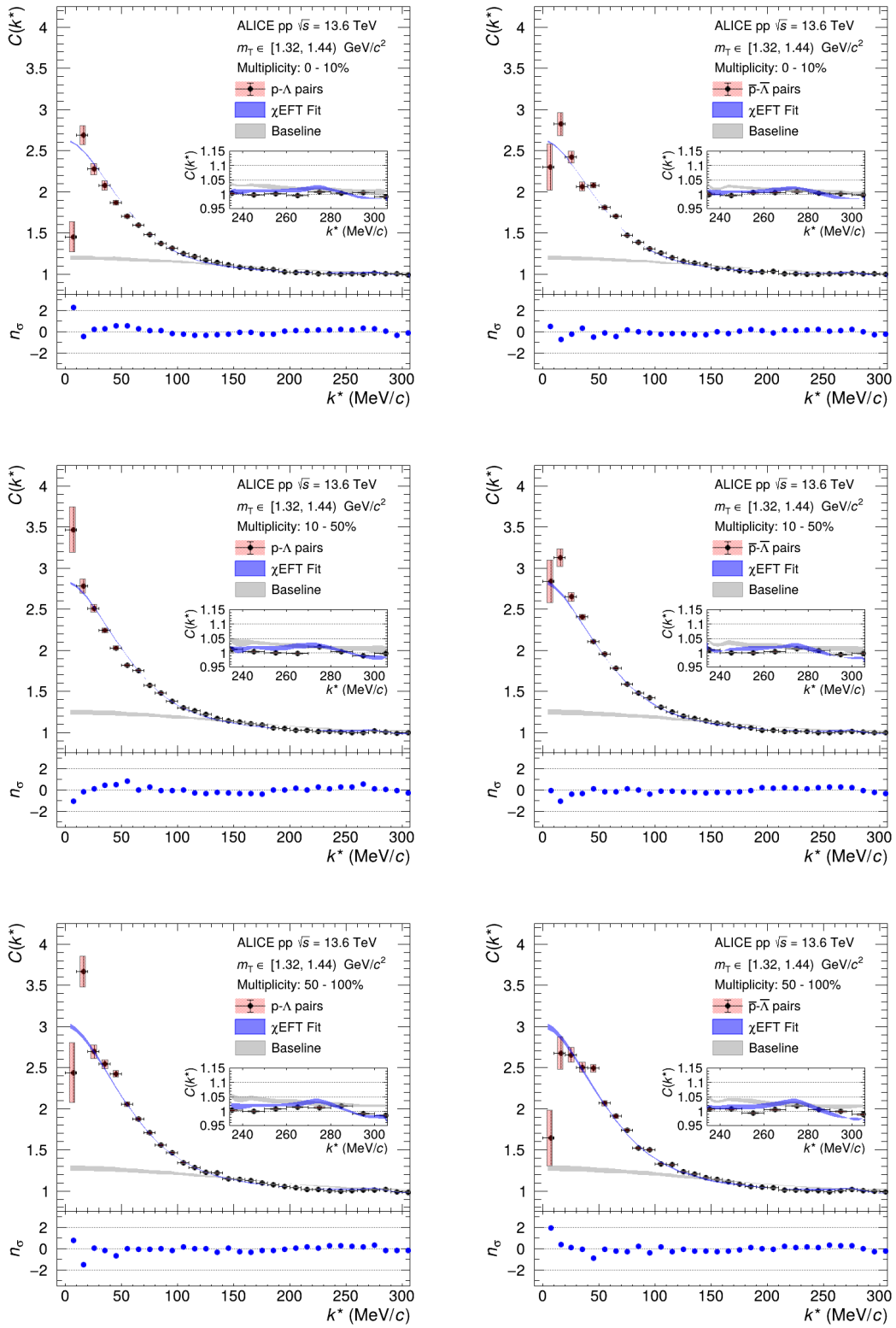

Figure 9.17: Simultaneous fits to the p–Λ and $\overline{\text{p}}$–$\overline{\Lambda}$ correlation functions with the NLO19 potential in the m_T range of [1.32, 1.44) GeV/c^2.

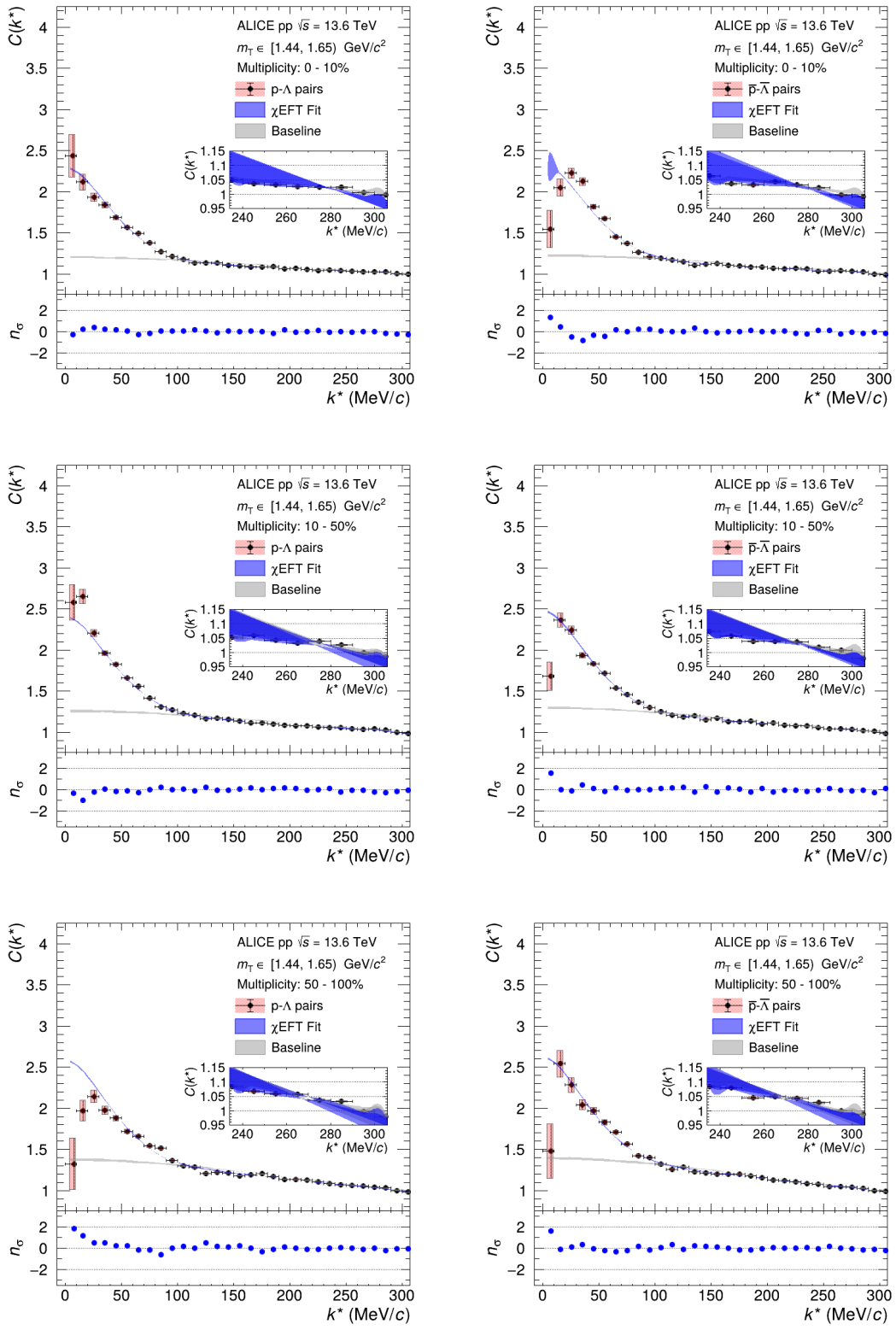

Figure 9.18: Simultaneous fits to the p–Λ and $\overline{\text{p}}$–$\overline{\Lambda}$ correlation functions with the NLO19 potential in the m_T range of [1.44, 1.65) GeV/c^2.

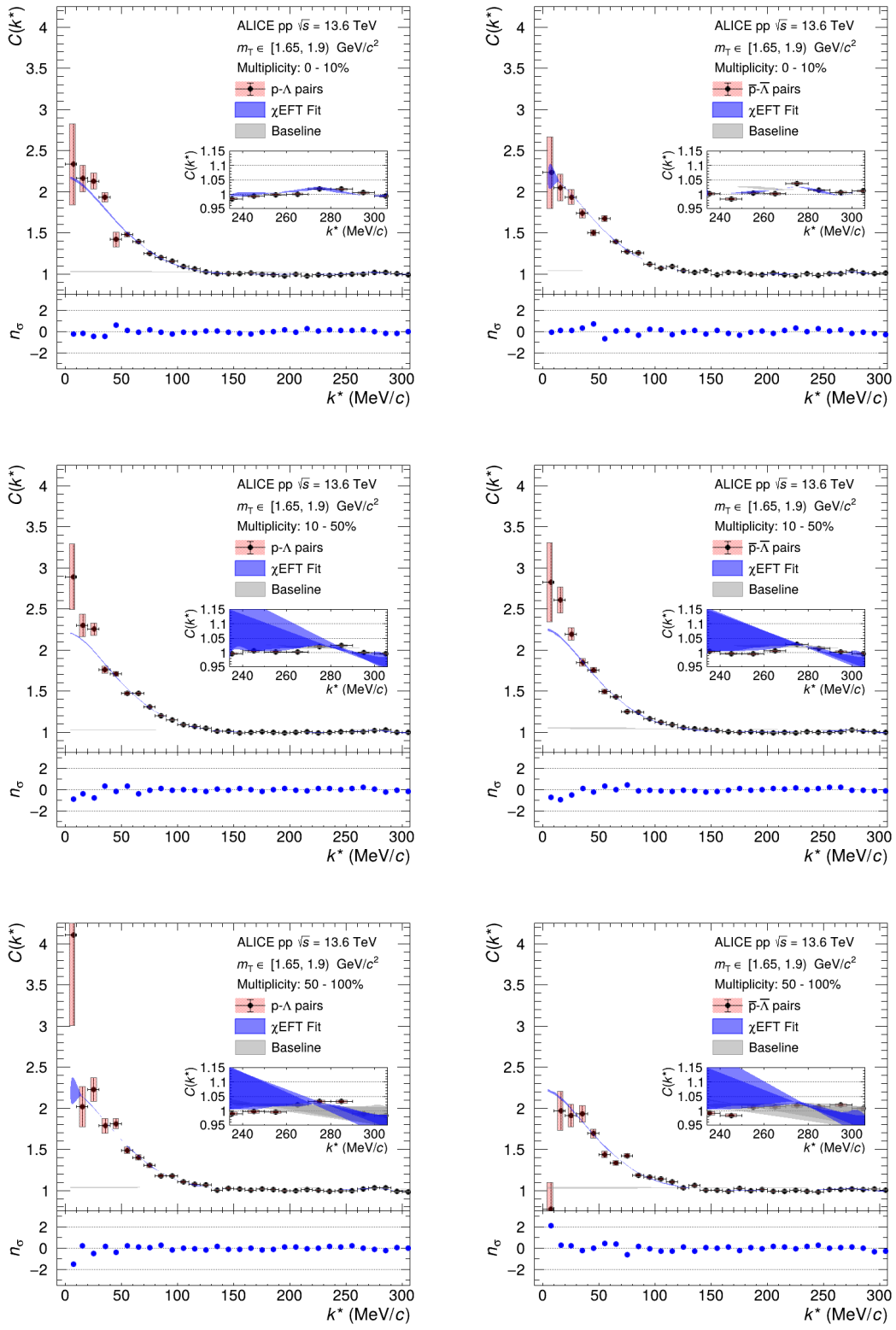

Figure 9.19: Simultaneous fits to the p–Λ and $\overline{\text{p}}$–$\overline{\Lambda}$ correlation functions with the NLO19 potential in the m_T range of [1.65, 1.90) GeV/c^2.

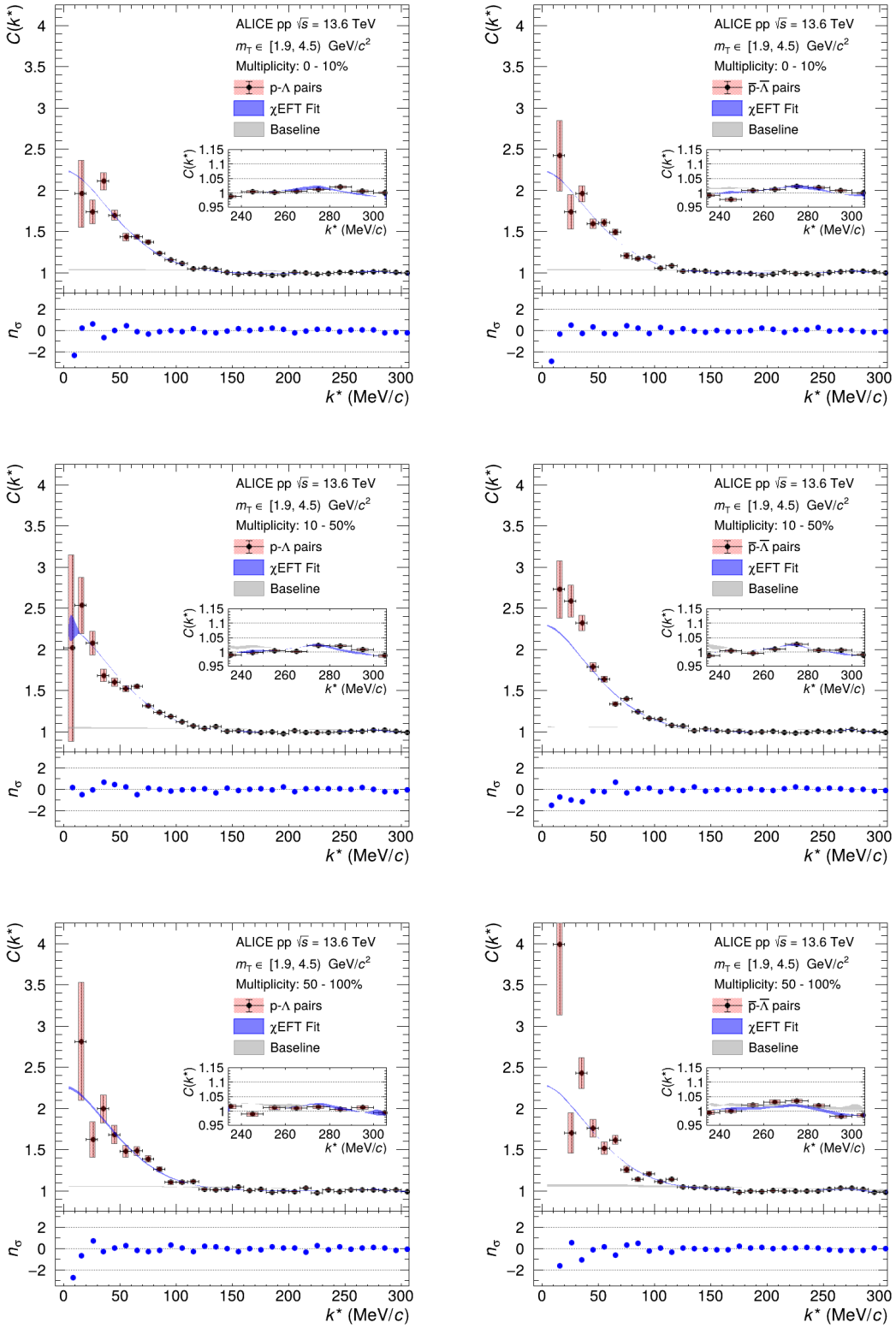

Figure 9.20: Simultaneous fits to the p–Λ and $\overline{\text{p}}$–$\overline{\Lambda}$ correlation functions with the NLO19 potential in the m_T range of [1.90, 4.50) GeV/c^2.

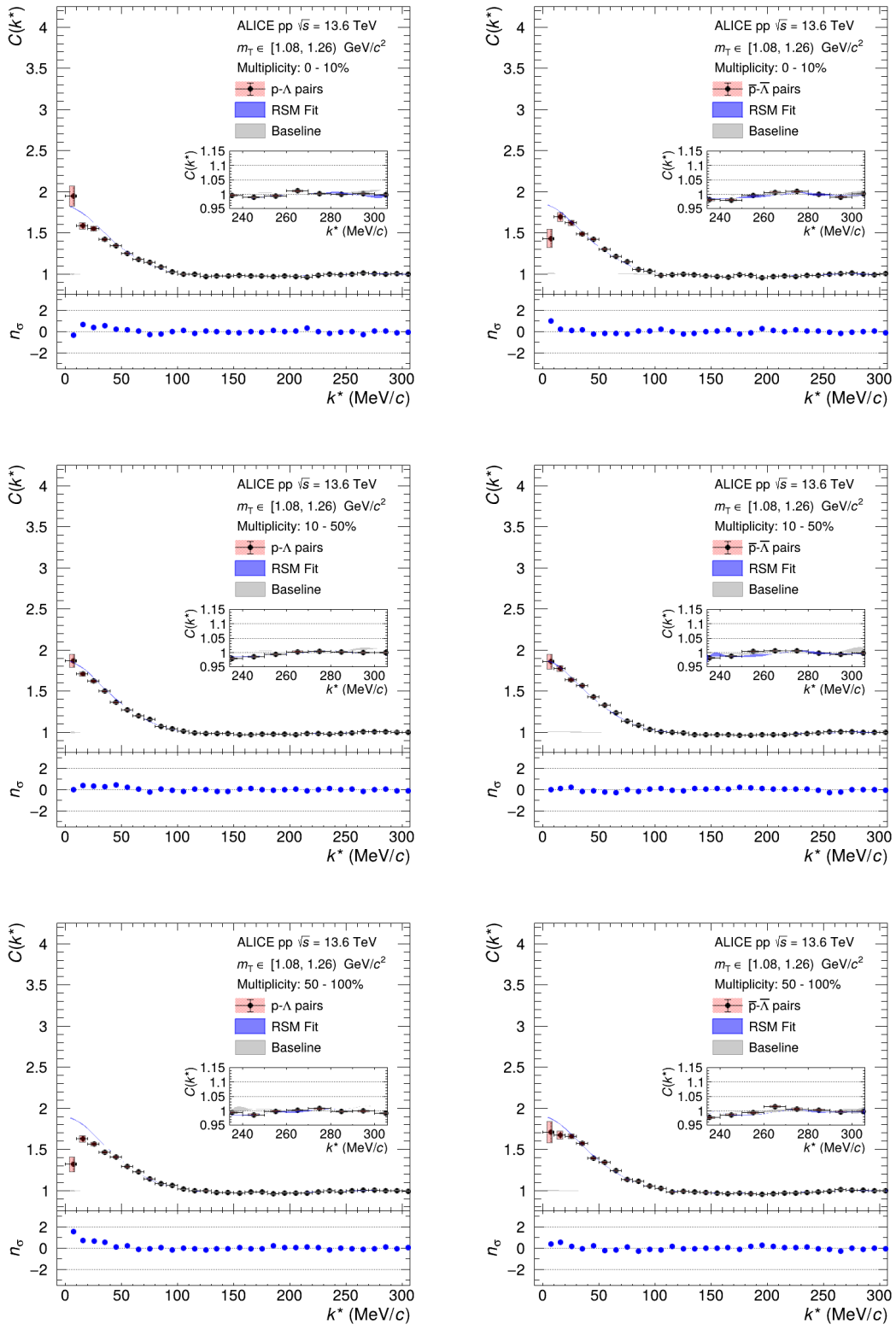

Figure 9.21: Simultaneous fits to the p–Λ and $\overline{\text{p}}$–$\overline{\Lambda}$ correlation functions with the RSM and the NLO19 potential in the m_{T} range of [1.08, 1.26) GeV/c^2.

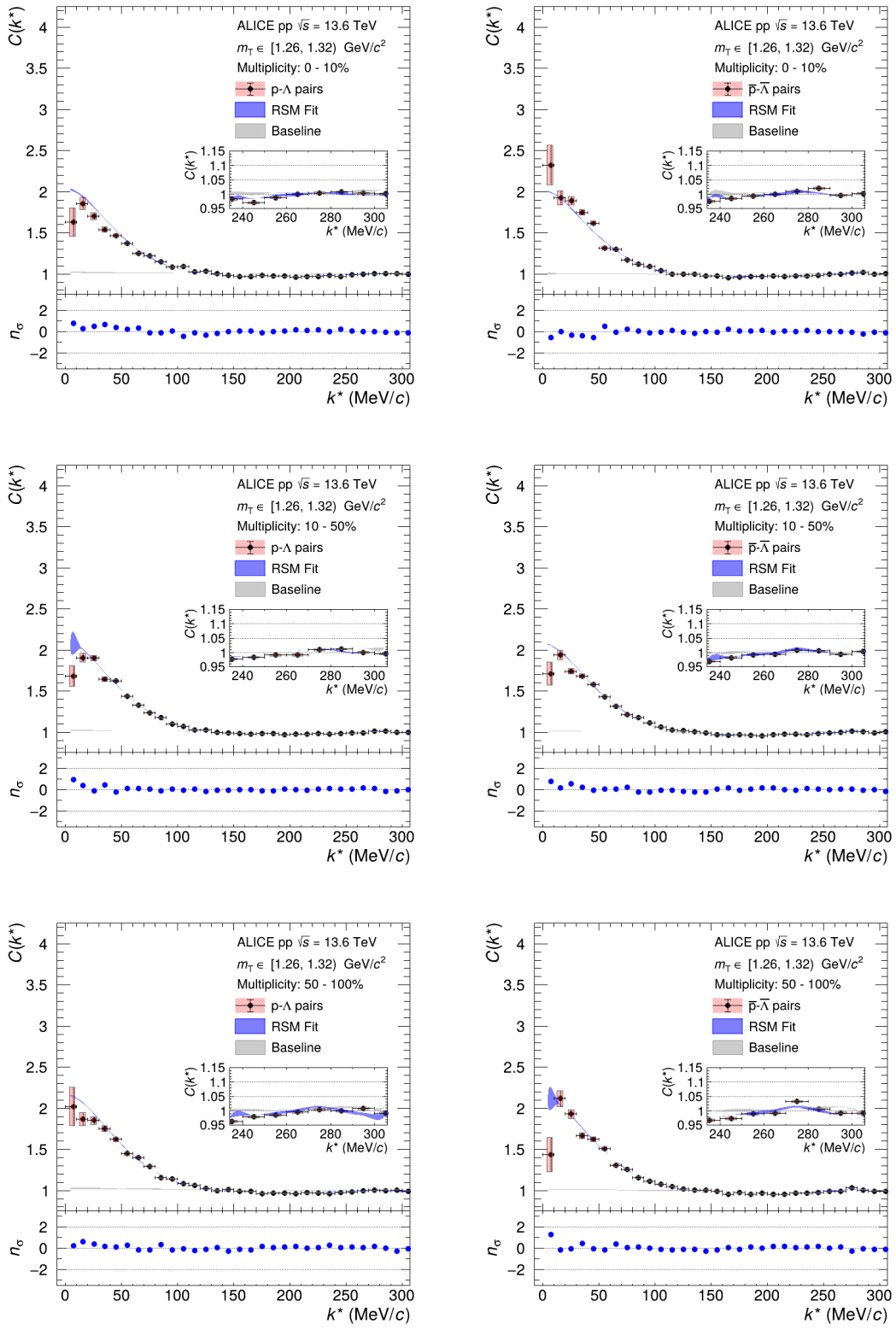

Figure 9.22: Simultaneous fits to the p–Λ and $\overline{\text{p}}$–$\overline{\Lambda}$ correlation functions with the RSM and the NLO19 potential in the m_{T} range of [1.26, 1.32) GeV/c^2.

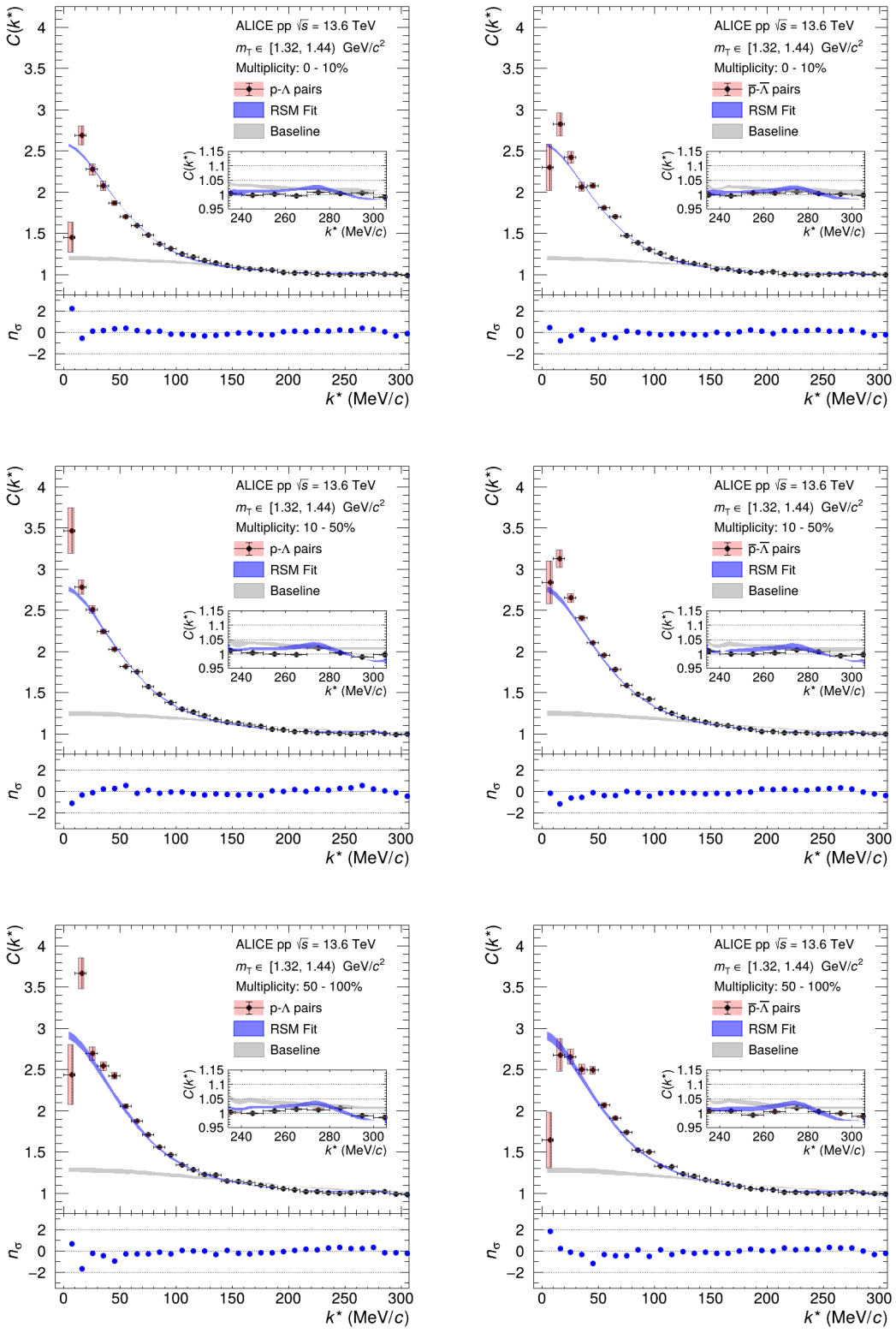

Figure 9.23: Simultaneous fits to the p–Λ and $\overline{\text{p}}$–$\overline{\Lambda}$ correlation functions with the RSM and the NLO19 potential in the m_T range of [1.32, 1.44) GeV/c^2.

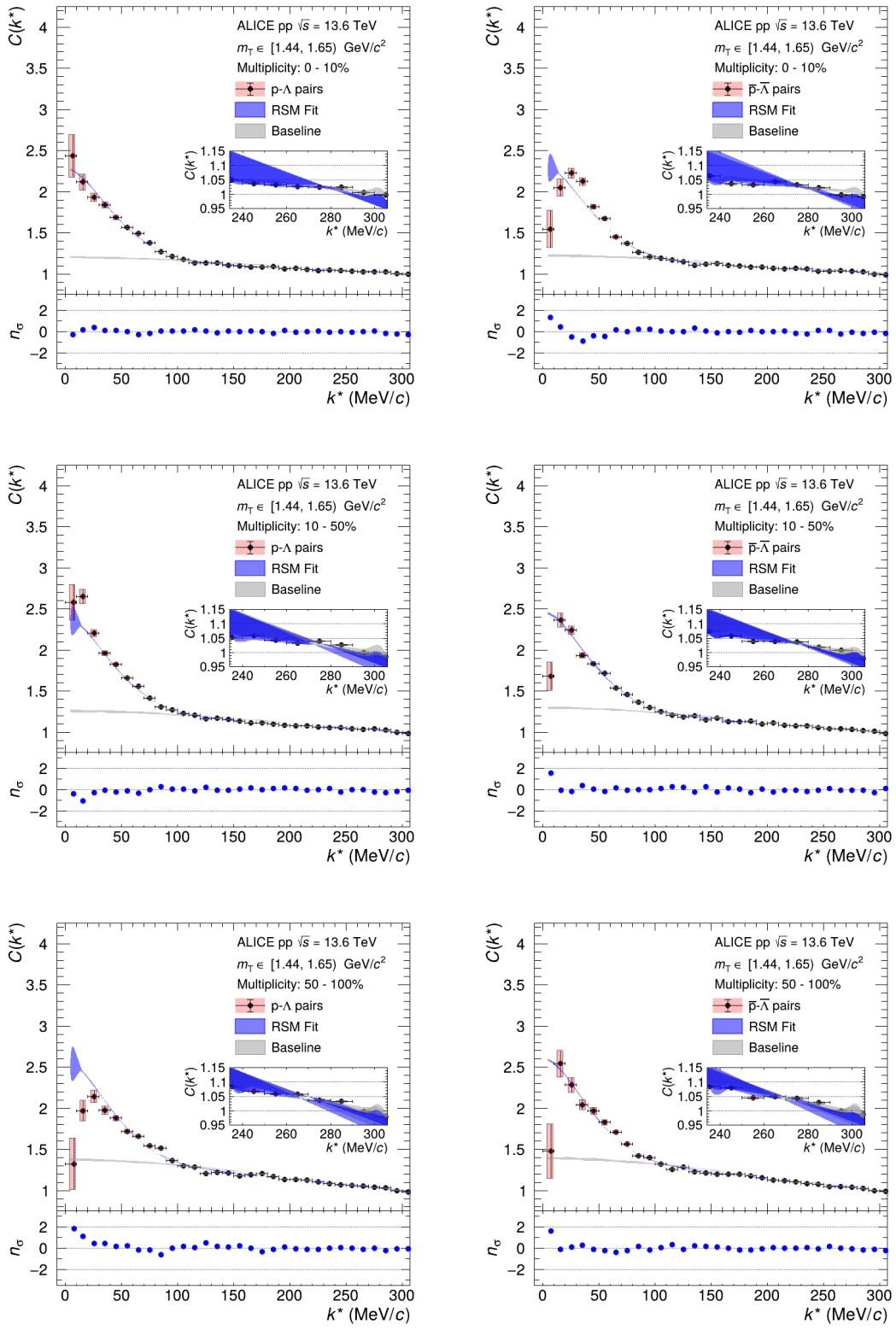

Figure 9.24: Simultaneous fits to the p–Λ and $\overline{\text{p}}$–$\overline{\Lambda}$ correlation functions with the RSM and the NLO19 potential in the m_T range of [1.44, 1.65) GeV/c^2.

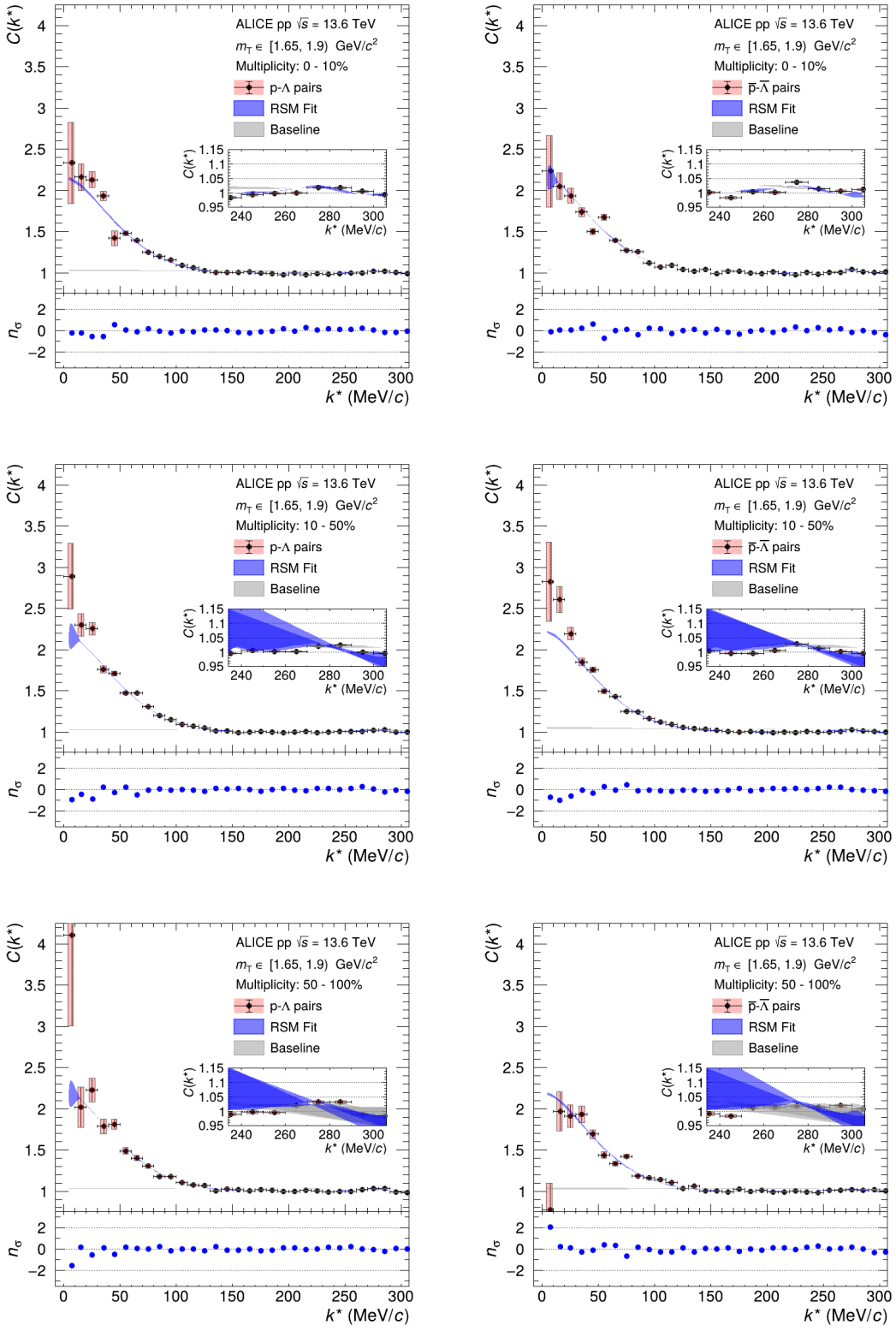

Figure 9.25: Simultaneous fits to the p–Λ and $\overline{\text{p}}$–$\overline{\Lambda}$ correlation functions with the RSM and the NLO19 potential in the m_{T} range of [1.65, 1.90) GeV/c^2.

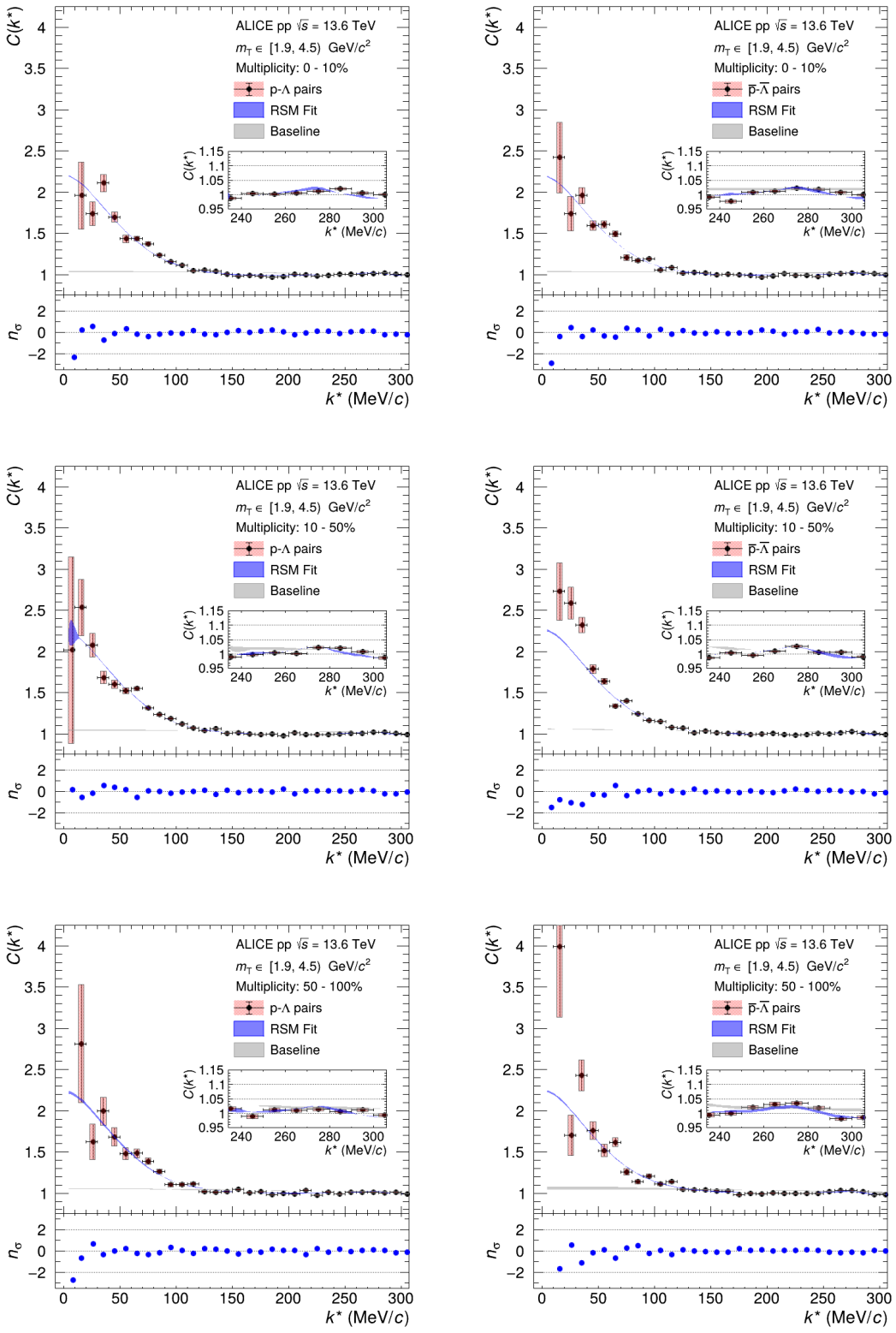

Figure 9.26: Simultaneous fits to the p–Λ and $\overline{\text{p}}$–$\overline{\Lambda}$ correlation functions with the RSM and the NLO19 potential in the m_{T} range of [1.90, 4.50) GeV/c^2.

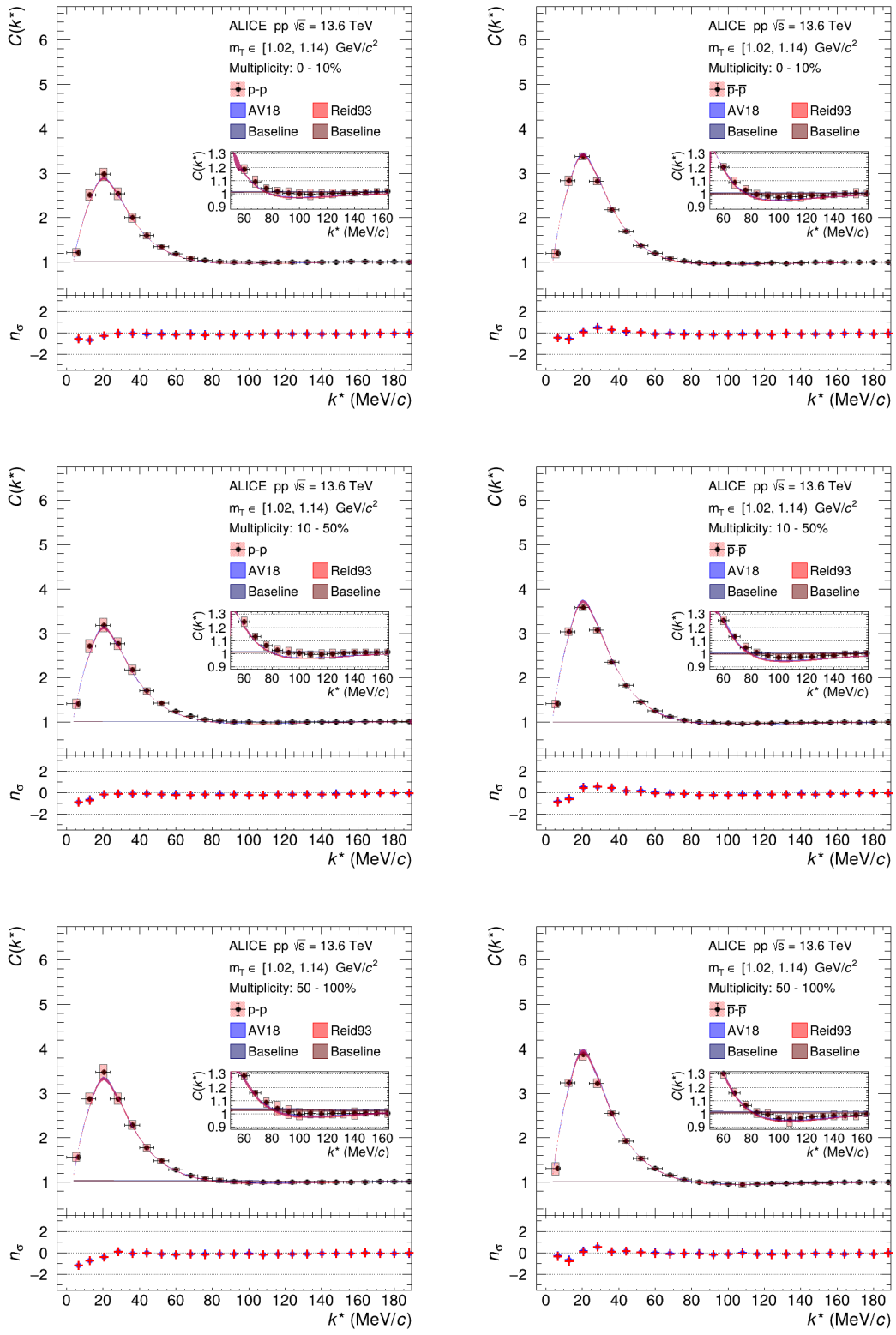

Figure 9.27: Comparison of the simultaneous fits to the p–p and $\overline{\text{p}}$–$\overline{\text{p}}$ correlation functions with the Argonne v_{18} and the Reid93 potential in the m_{T} range of [1.02, 1.14) GeV/c^2.

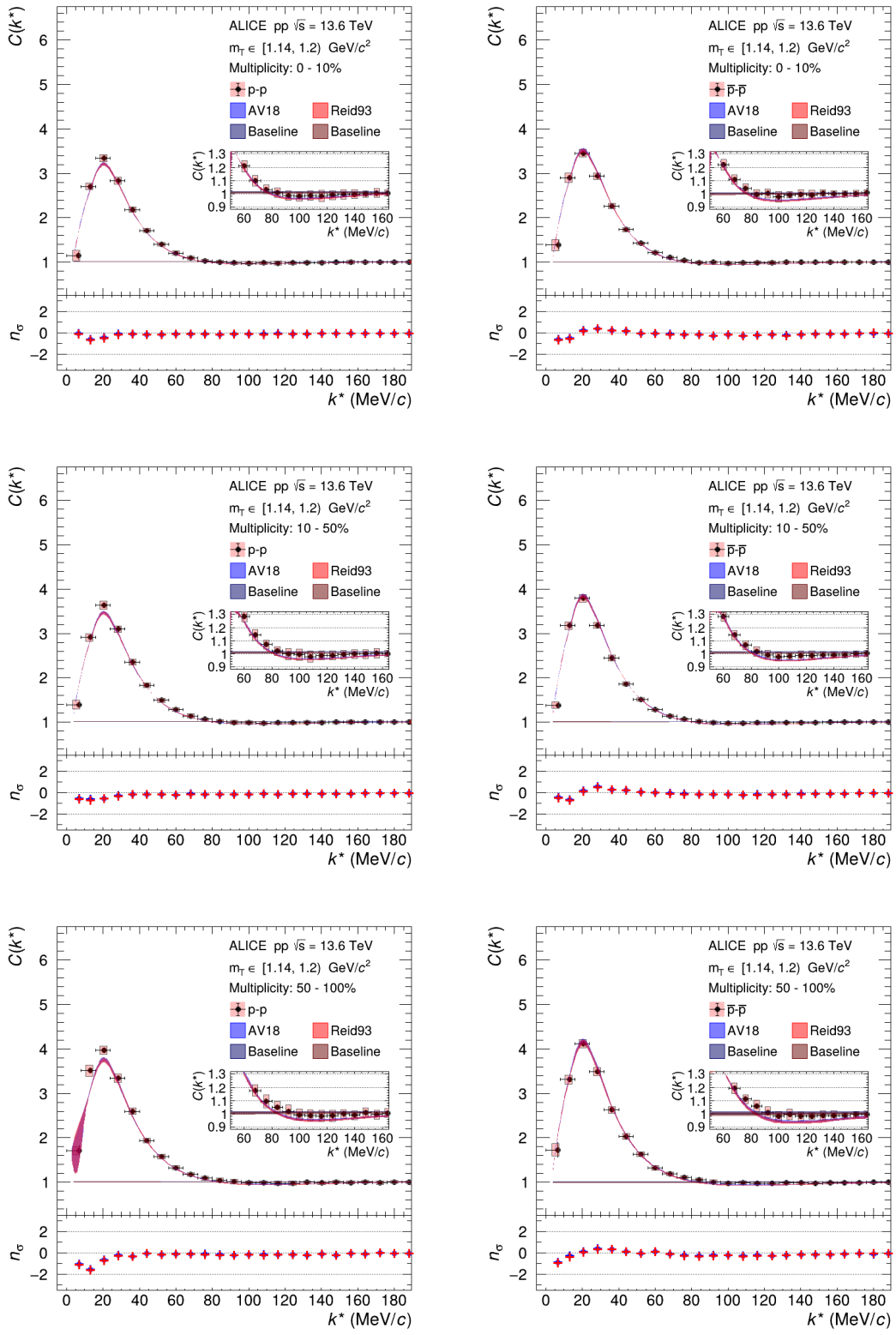

Figure 9.28: Comparison of the simultaneous fits to the p–p and $\overline{\text{p}}$–$\overline{\text{p}}$ correlation functions with the Argonne v_{18} and the Reid93 potential in the m_{T} range of [1.14, 1.20) GeV/c^2.

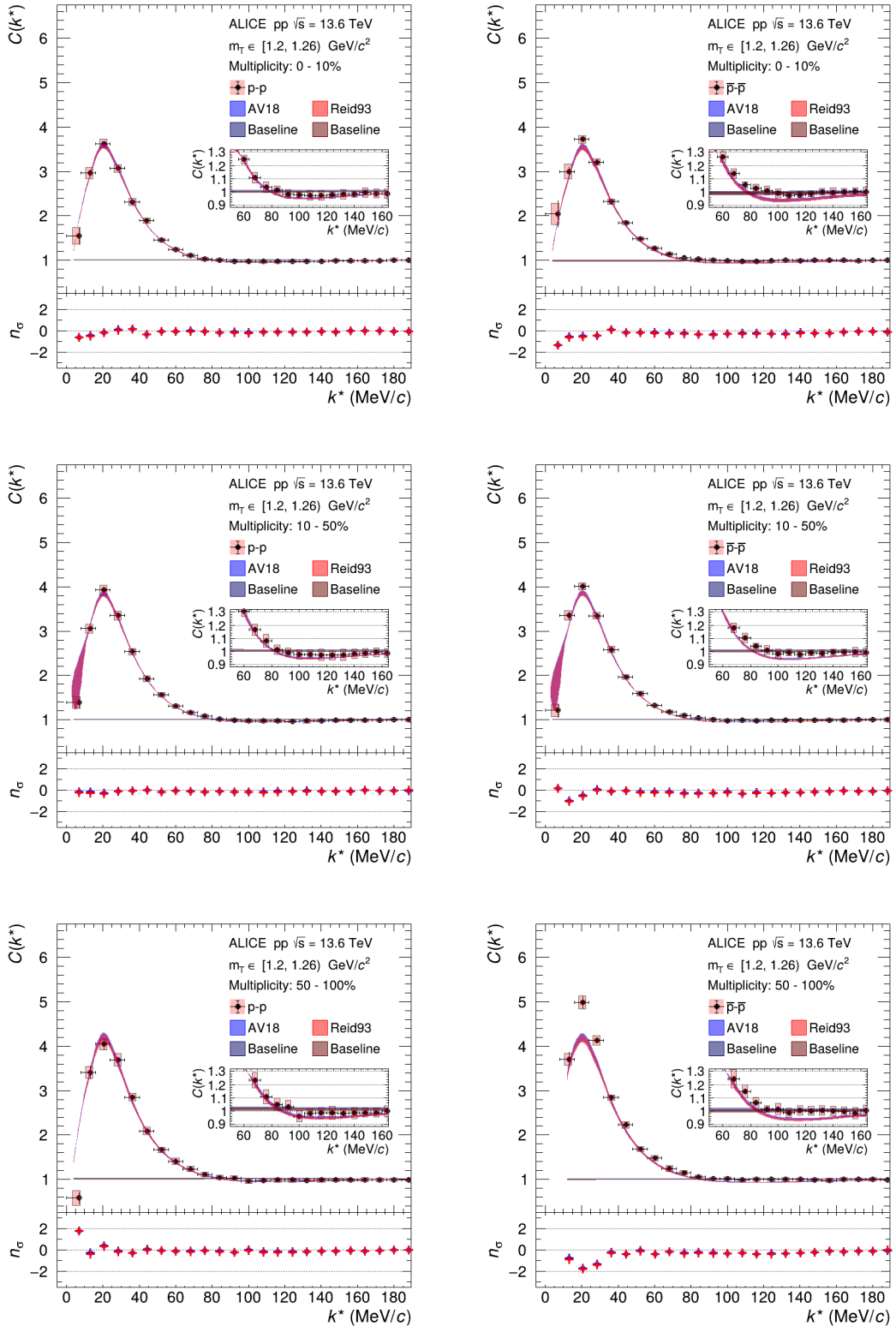

Figure 9.29: Comparison of the simultaneous fits to the p–p and $\overline{\text{p}}$–$\overline{\text{p}}$ correlation functions with the Argonne v_{18} and the Reid93 potential in the m_{T} range of [1.20, 1.26) GeV/c^2.

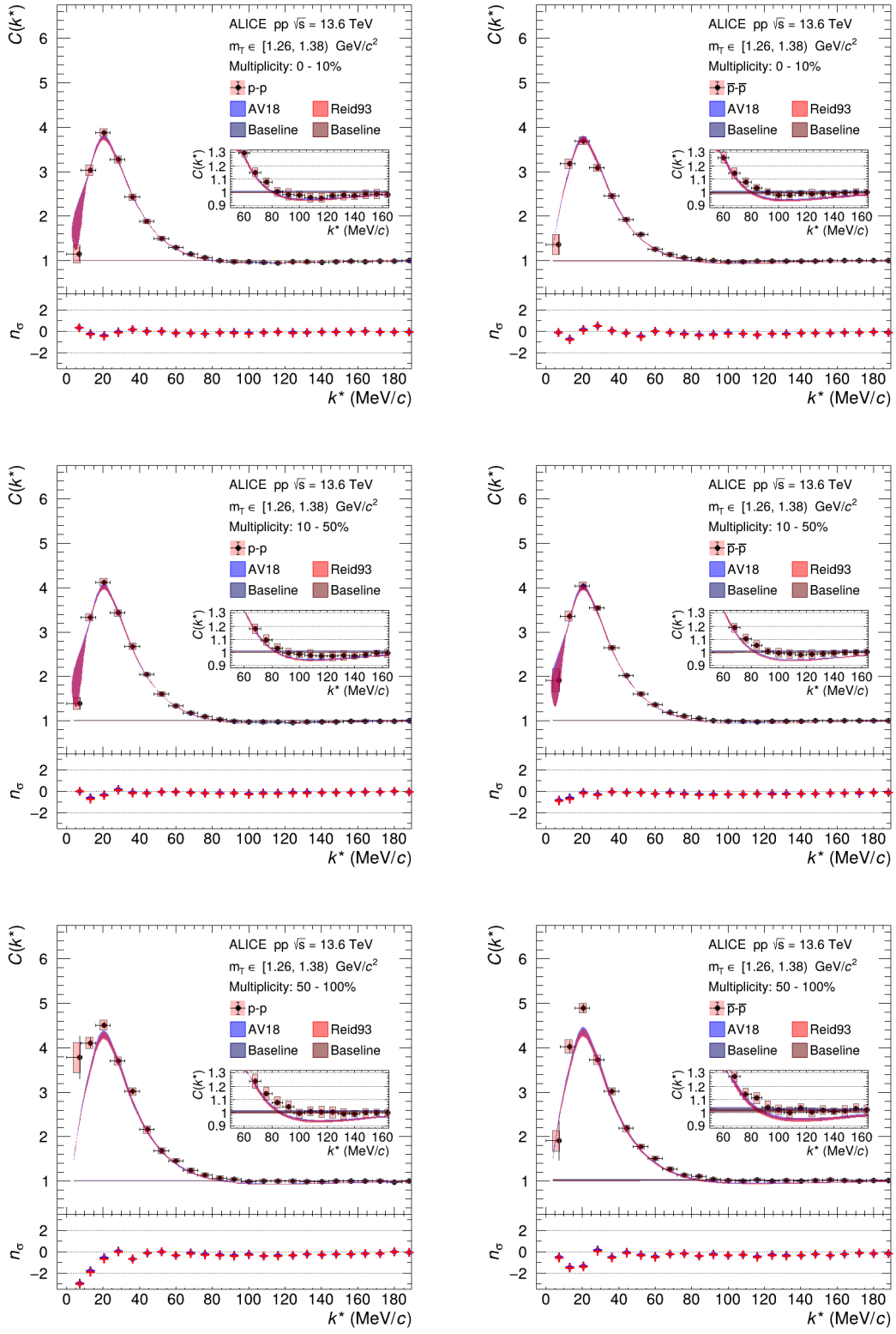

Figure 9.30: Comparison of the simultaneous fits to the p–p and $\overline{\text{p}}$–$\overline{\text{p}}$ correlation functions with the Argonne v_{18} and the Reid93 potential in the m_{T} range of [1.26, 1.38) GeV/c^2.

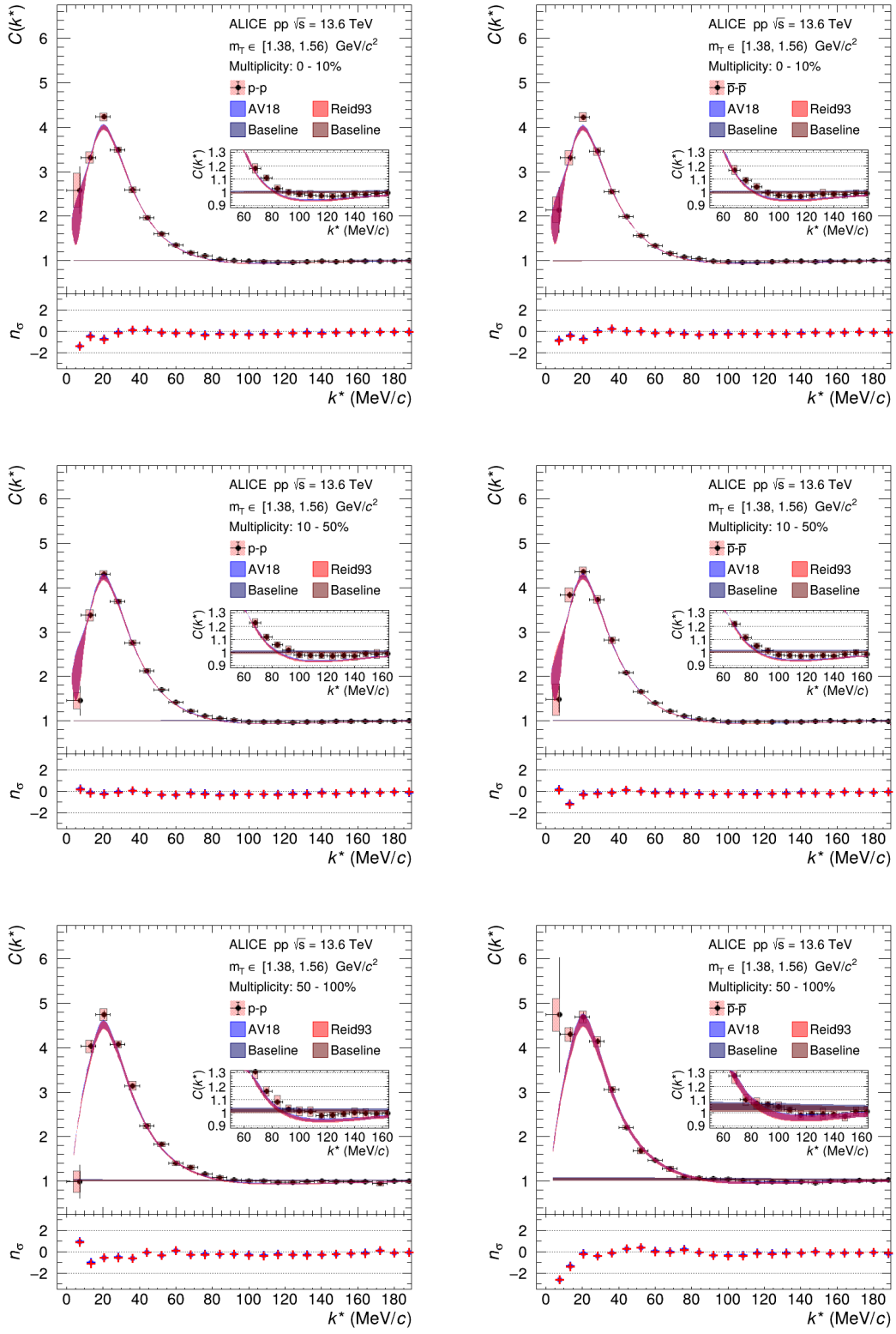

Figure 9.31: Comparison of the simultaneous fits to the p–p and $\overline{\text{p}}$–$\overline{\text{p}}$ correlation functions with the Argonne v_{18} and the Reid93 potential in the m_{T} range of [1.38, 1.56) GeV/c^2.

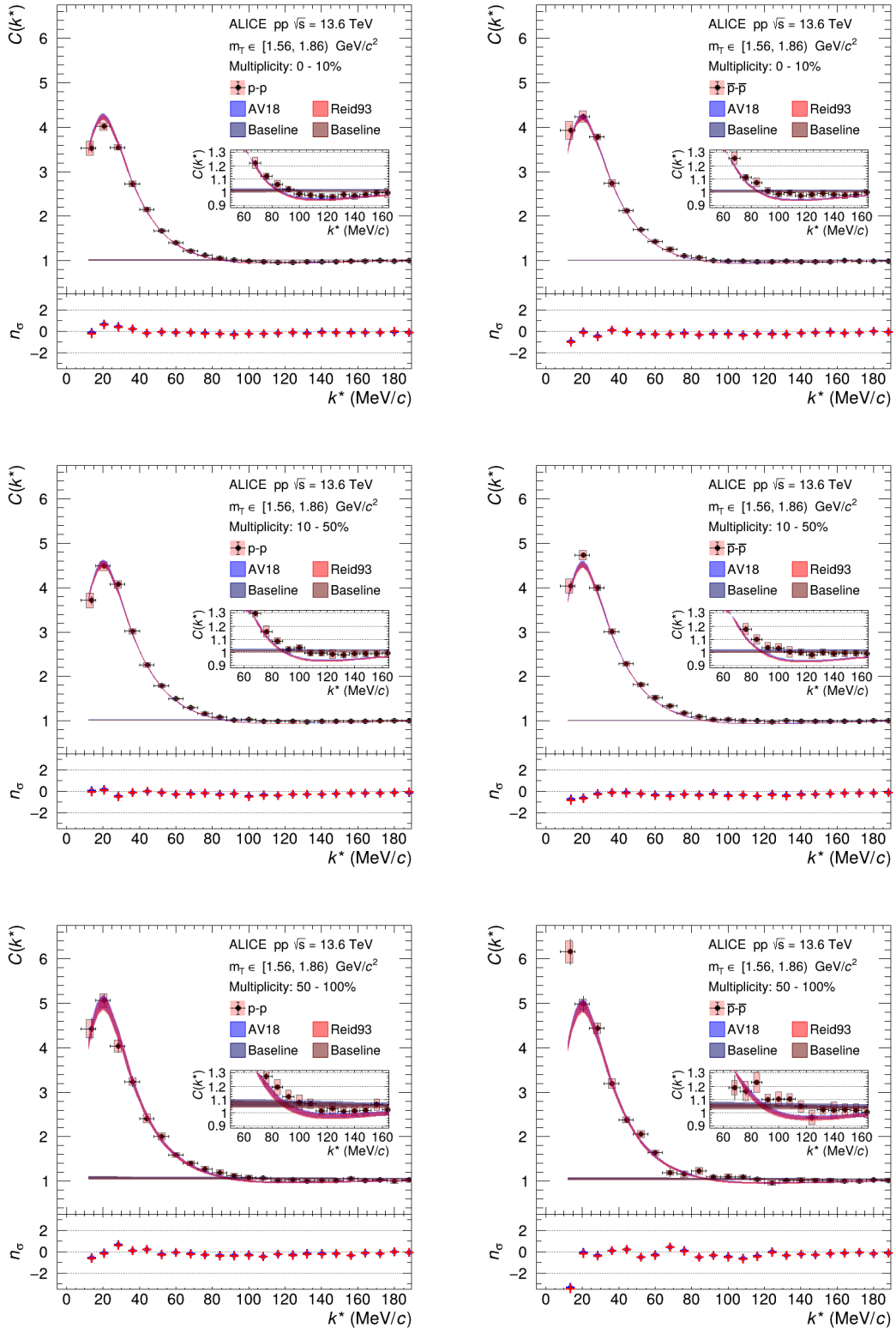

Figure 9.32: Comparison of the simultaneous fits to the p–p and $\overline{\text{p}}$–$\overline{\text{p}}$ correlation functions with the Argonne v_{18} and the Reid93 potential in the m_{T} range of [1.56, 1.86) GeV/c^2.

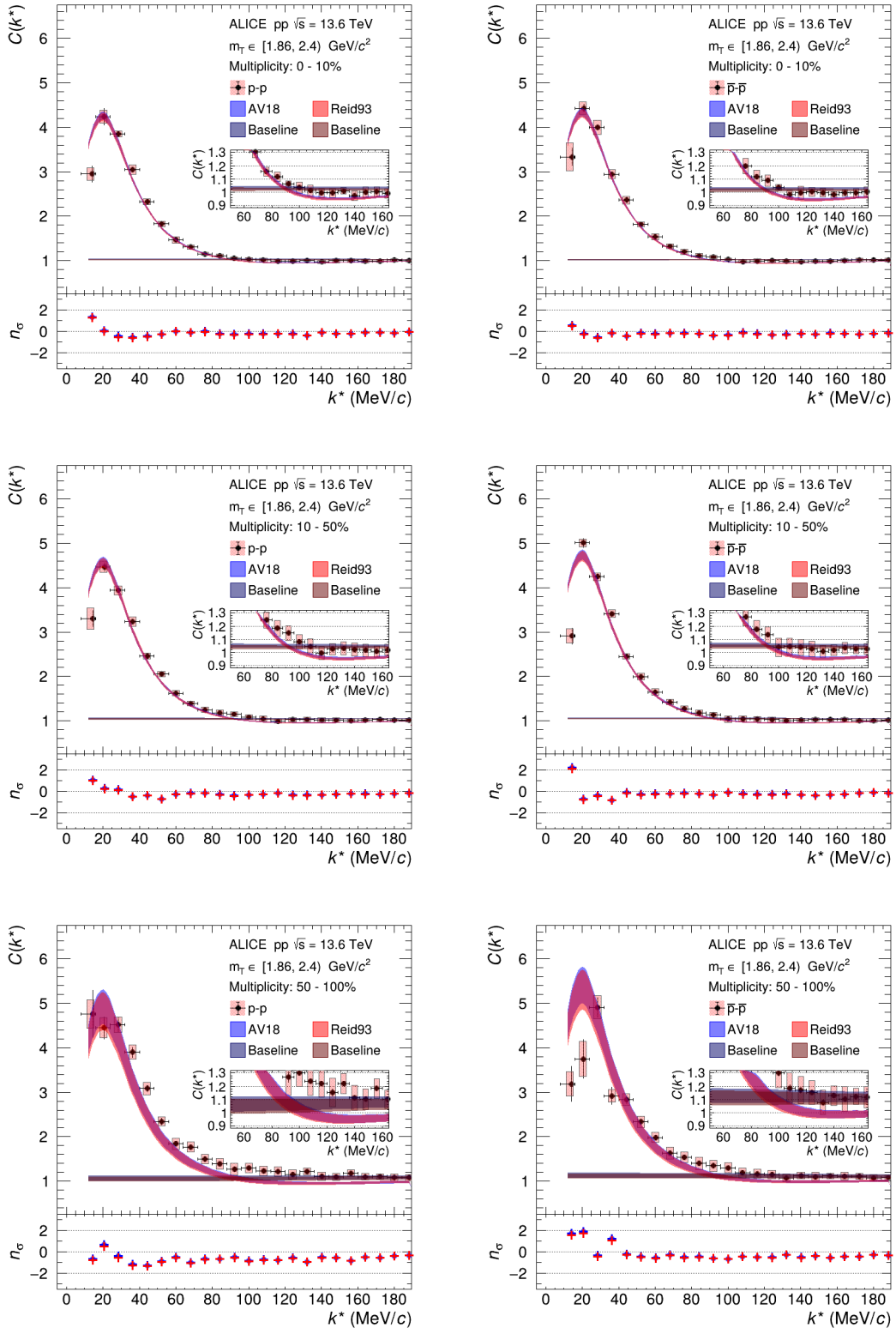

Figure 9.33: Comparison of the simultaneous fits to the p–p and $\overline{\text{p}}$–$\overline{\text{p}}$ correlation functions with the Argonne v_{18} and the Reid93 potential in the m_{T} range of [1.86, 2.40) GeV/c^2.

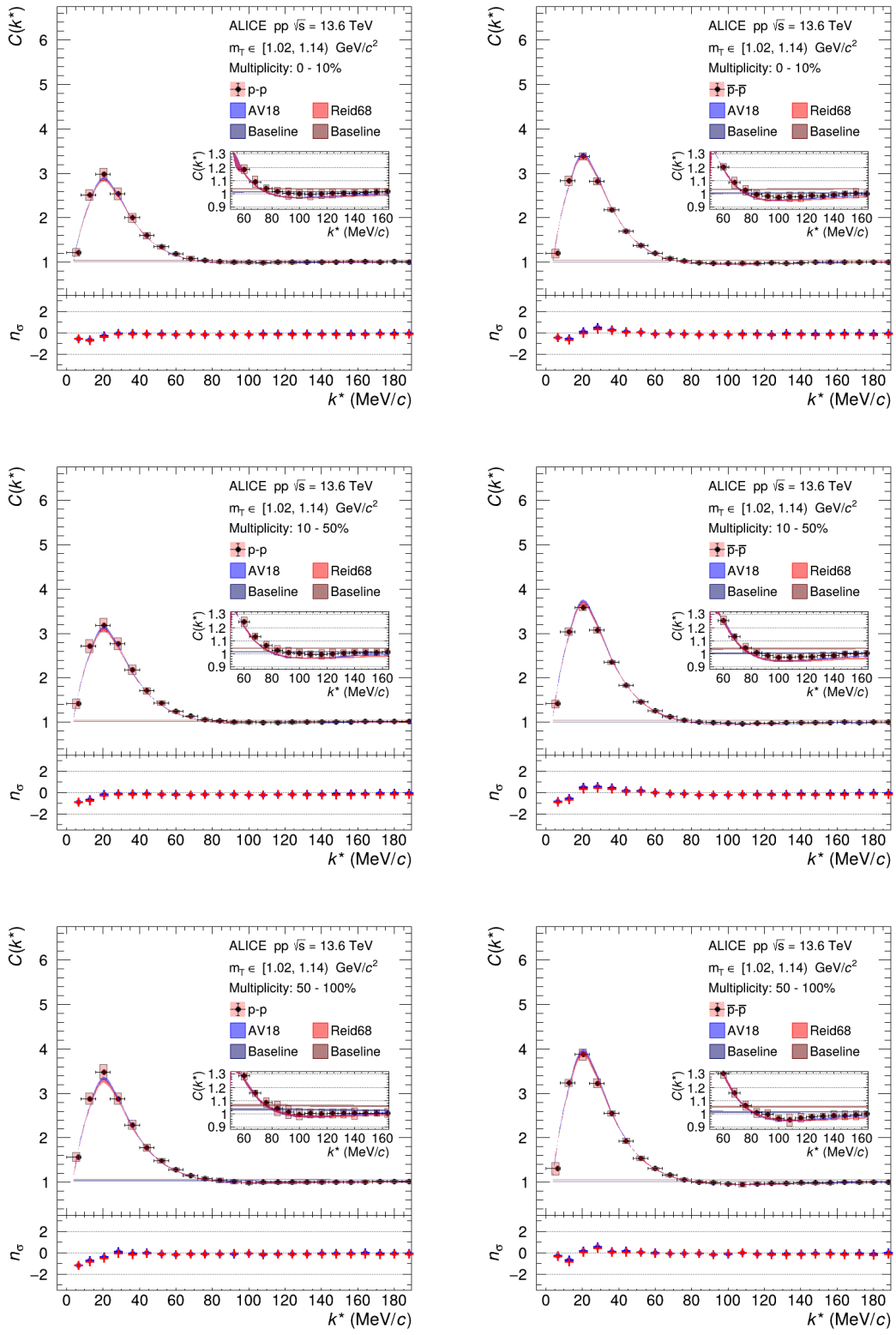

Figure 9.34: Comparison of the simultaneous fits to the p–p and $\overline{\text{p}}$–$\overline{\text{p}}$ correlation functions with the Argonne v_{18} and the Reid68 potential in the m_{T} range of [1.02, 1.14) GeV/c^2.

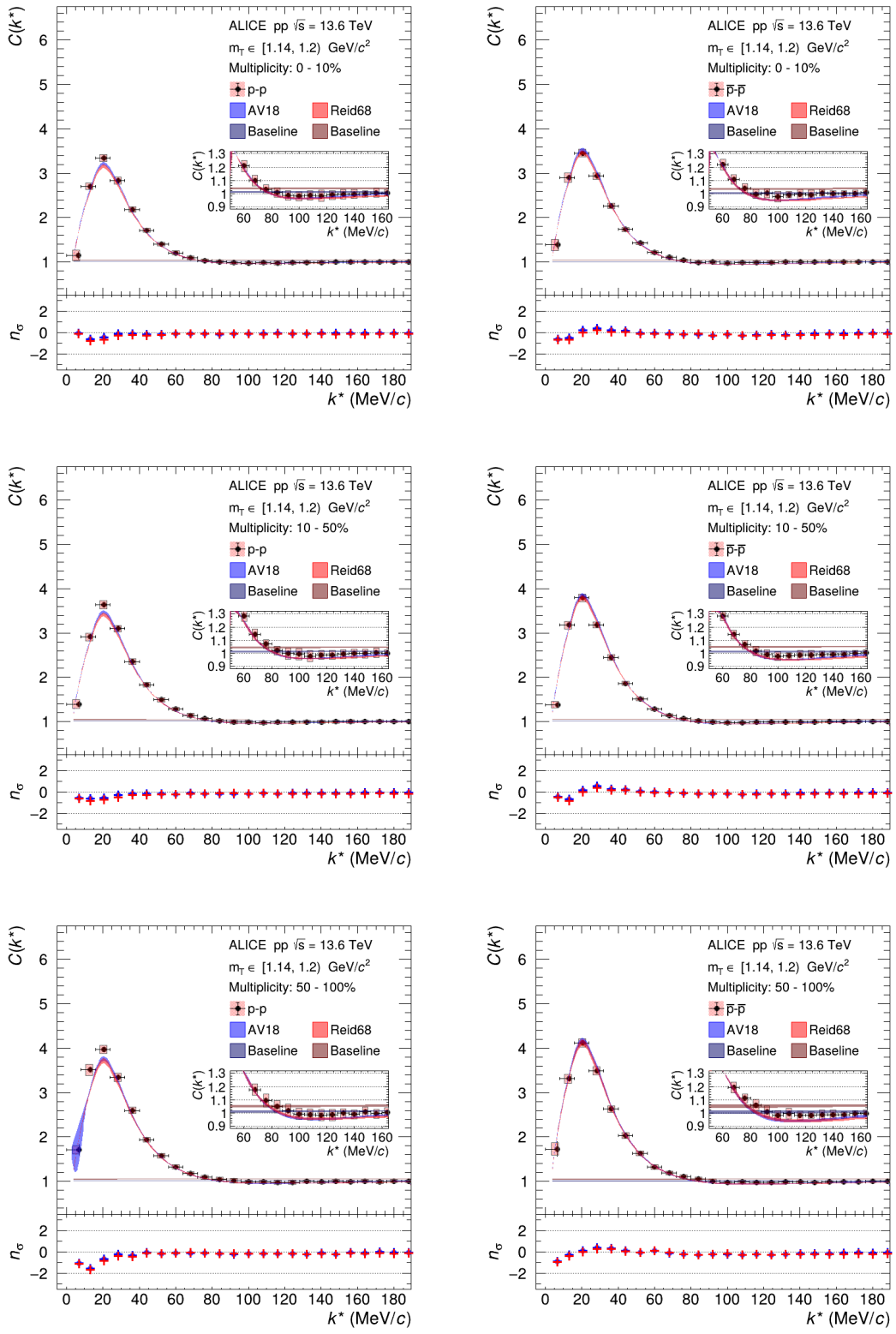

Figure 9.35: Comparison of the simultaneous fits to the p–p and $\overline{\text{p}}$–$\overline{\text{p}}$ correlation functions with the Argonne v_{18} and the Reid68 potential in the m_{T} range of [1.14, 1.20) GeV/c^2.

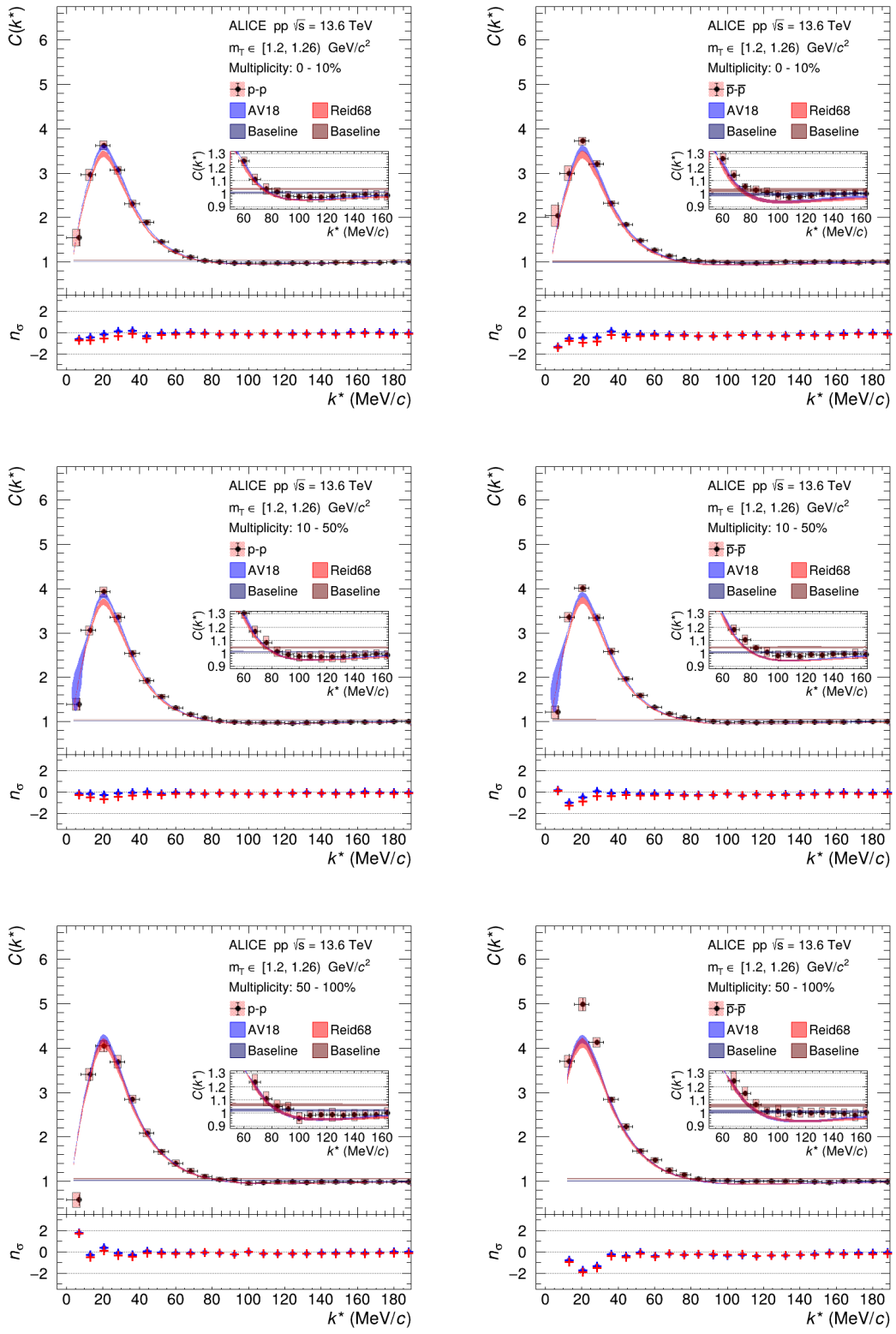

Figure 9.36: Comparison of the simultaneous fits to the p–p and $\overline{\text{p}}$–$\overline{\text{p}}$ correlation functions with the Argonne v_{18} and the Reid68 potential in the m_{T} range of [1.20, 1.26) GeV/c^2.

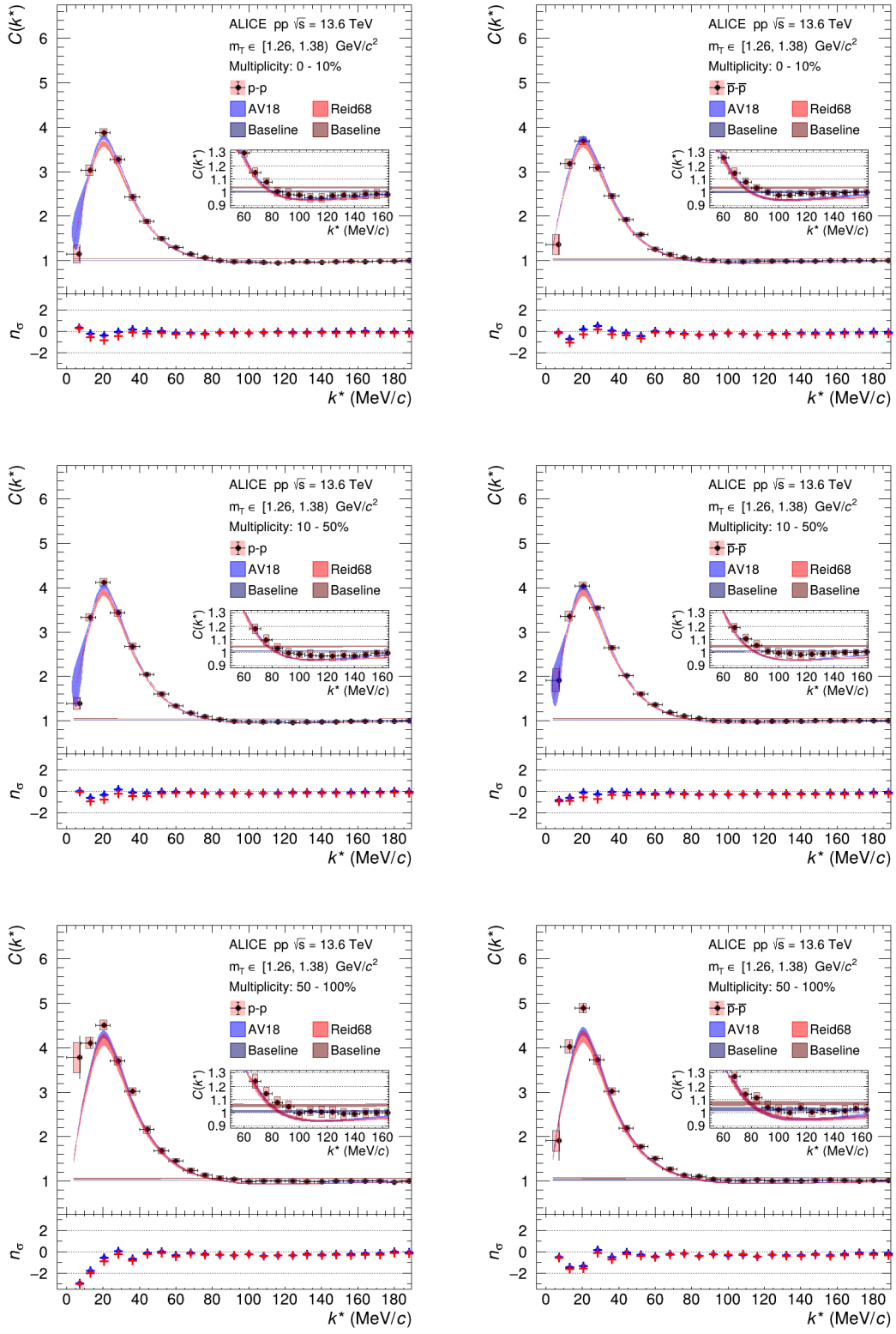

Figure 9.37: Comparison of the simultaneous fits to the p–p and $\overline{\text{p}}$–$\overline{\text{p}}$ correlation functions with the Argonne v_{18} and the Reid68 potential in the m_{T} range of [1.26, 1.38) GeV/c^2.

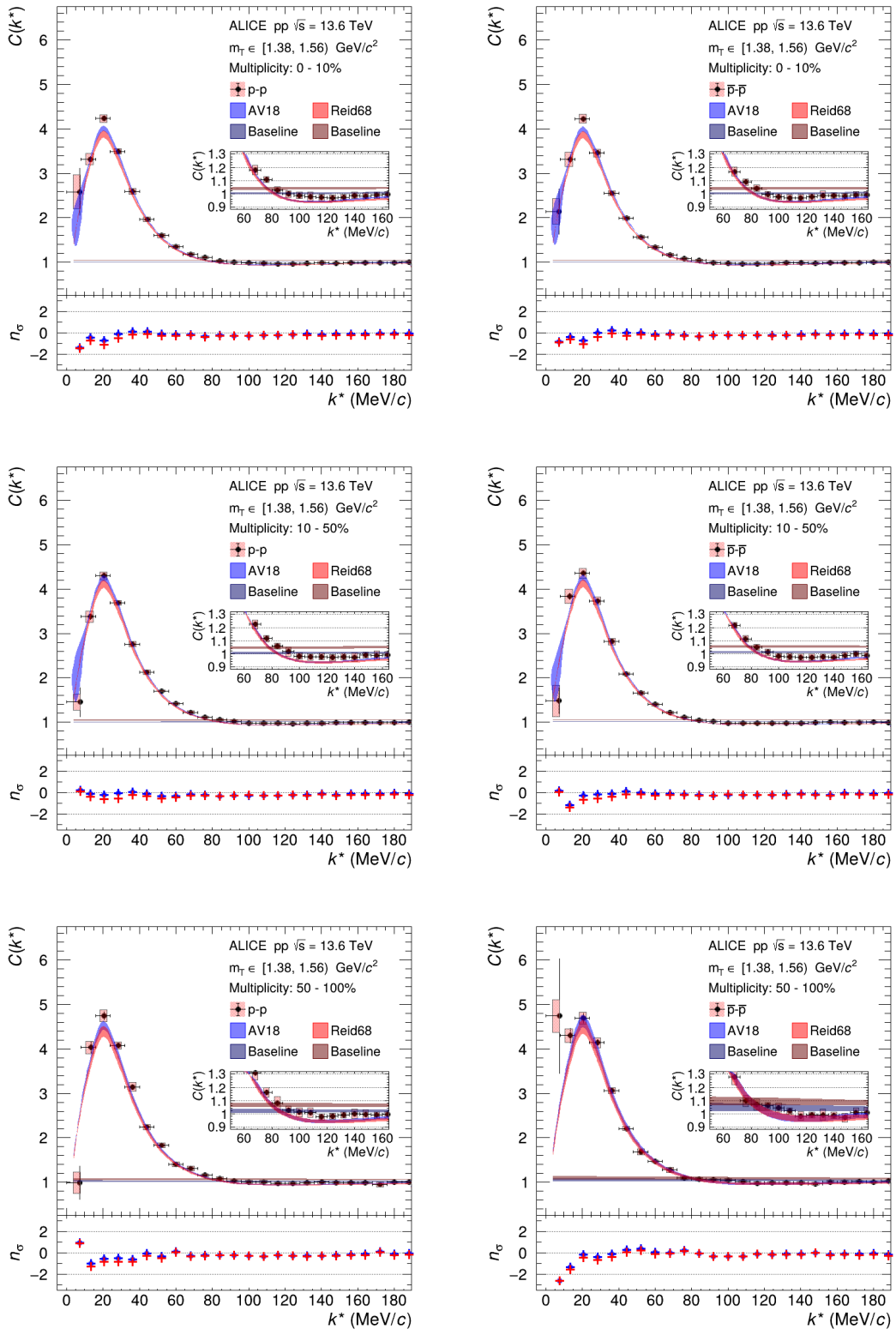

Figure 9.38: Comparison of the simultaneous fits to the p–p and $\overline{\text{p}}$–$\overline{\text{p}}$ correlation functions with the Argonne v_{18} and the Reid68 potential in the m_{T} range of [1.38, 1.56) GeV/c^2.

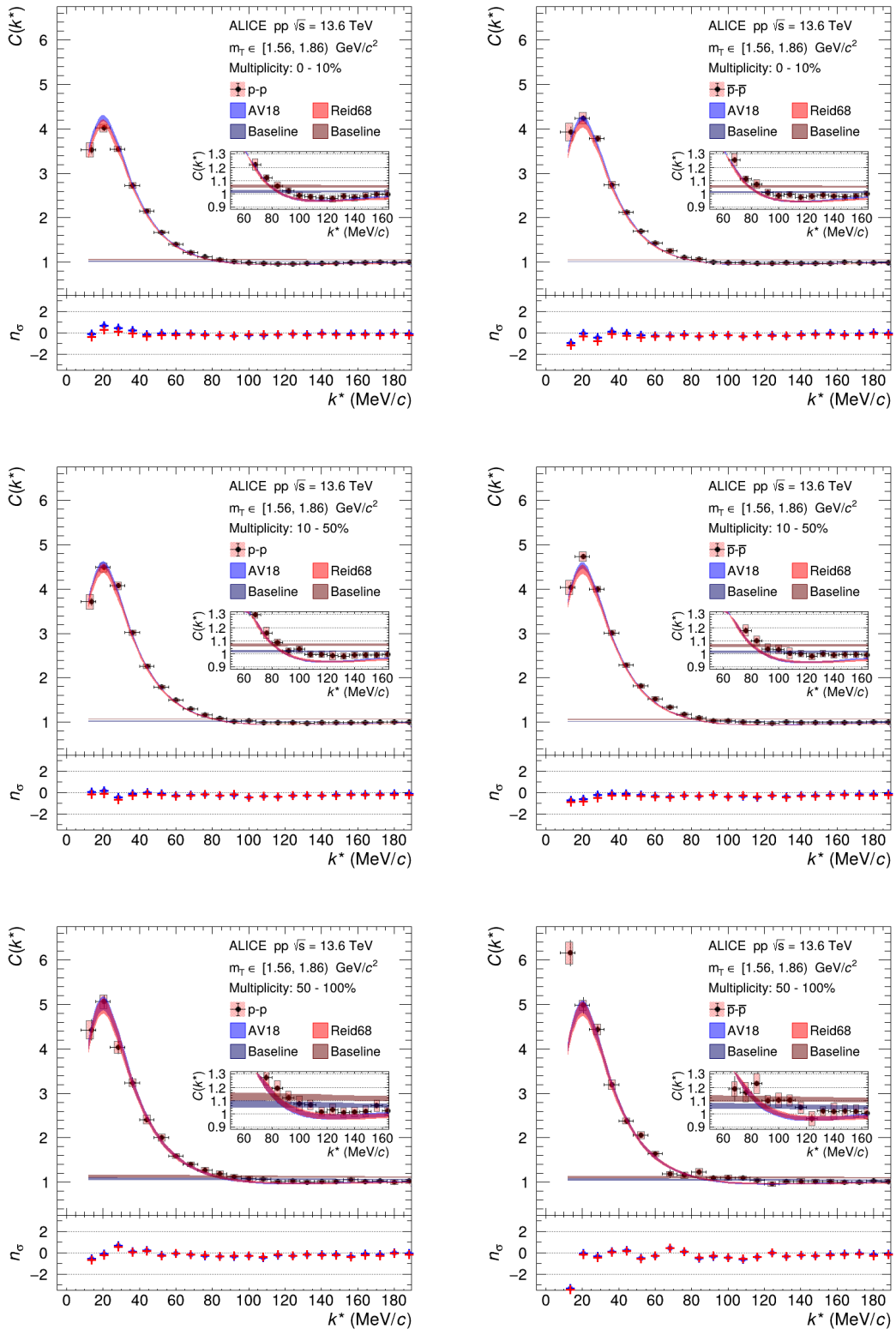

Figure 9.39: Comparison of the simultaneous fits to the p–p and $\overline{\text{p}}$–$\overline{\text{p}}$ correlation functions with the Argonne v_{18} and the Reid68 potential in the m_{T} range of [1.56, 1.86) GeV/c^2.

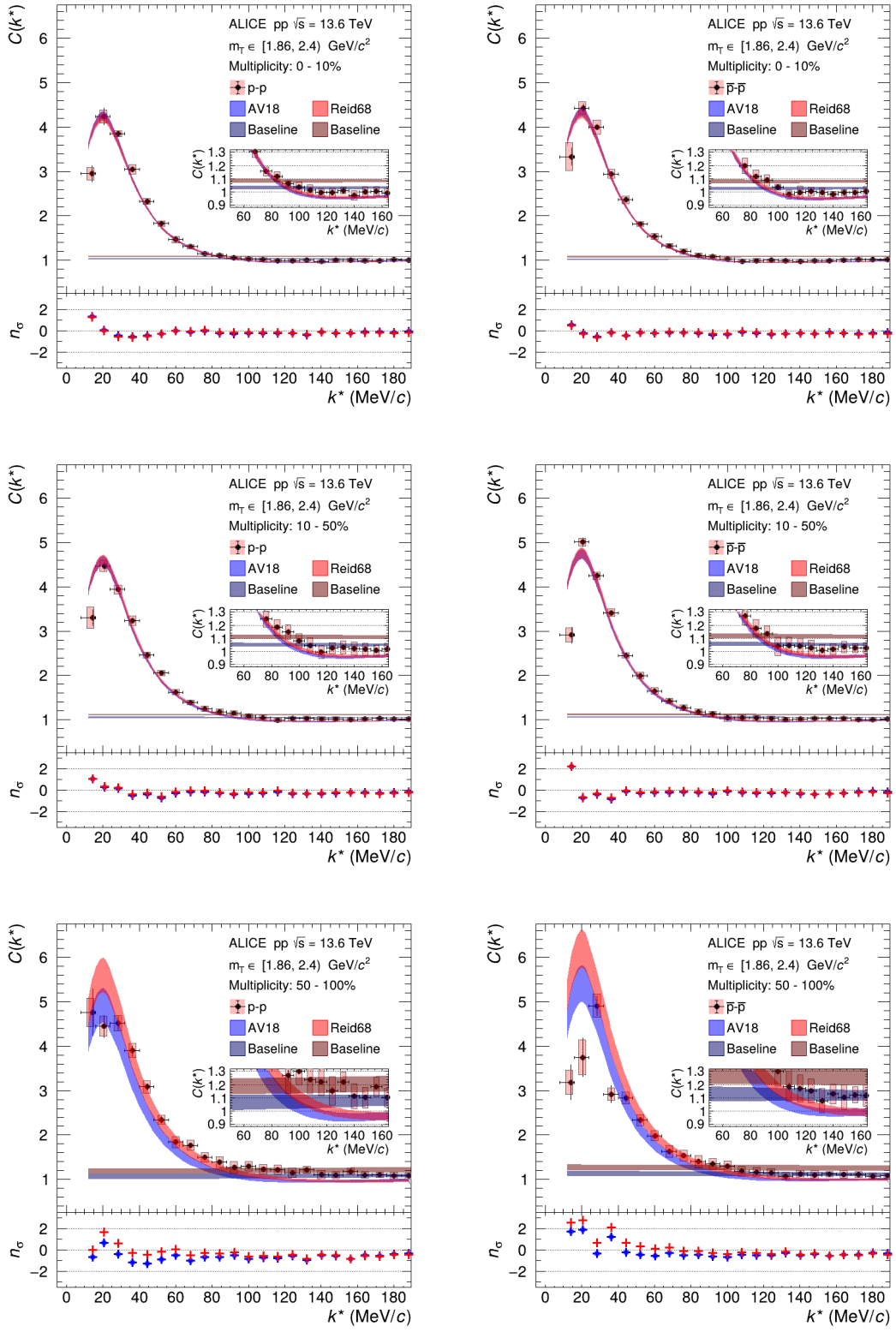

Figure 9.40: Comparison of the simultaneous fits to the p–p and $\overline{\text{p}}$–$\overline{\text{p}}$ correlation functions with the Argonne v_{18} and the Reid68 potential in the m_{T} range of [1.86, 2.40) GeV/c^2.

Acknowledgments

List of Figures

List of Tables

Bibliography

[1] R. Hanbury Brown and R. Q. Twiss. "A New type of interferometer for use in radio astronomy". In: *Phil. Mag. Ser. 7* 45 (1954), pp. 663–682. DOI: 10.1080/14786440708520475.

[2] G. Goldhaber, S. Goldhaber, W.-Y. Lee, and A. Pais. "Influence of Bose-Einstein statistics on the anti-proton proton annihilation process". In: *Phys. Rev.* 120 (1960). Ed. by R. M. Weiner, pp. 300–312. DOI: 10.1103/PhysRev.120.300.

[3] S. Acharya et al. "The ALICE experiment: a journey through QCD". In: *Eur. Phys. J. C* 84.8 (2024), p. 813. DOI: 10.1140/epjc/s10052-024-12935-y. arXiv: 2211.04384 [nucl-ex].

[4] C. Drischler, J. W. Holt, and C. Wellenhofer. "Chiral Effective Field Theory and the High-Density Nuclear Equation of State". In: *Ann. Rev. Nucl. Part. Sci.* 71 (2021), pp. 403–432. DOI: 10.1146/annurev-nucl-102419-041903. arXiv: 2101.01709 [nucl-th].

[5] J. Antoniadis et al. "A Massive Pulsar in a Compact Relativistic Binary". In: *Science* 340 (2013), p. 6131. DOI: 10.1126/science.1233232. arXiv: 1304.6875 [astro-ph.HE].

[6] H. T. Cromartie et al. "Relativistic Shapiro delay measurements of an extremely massive millisecond pulsar". In: *Nature Astron.* 4.1 (2019), pp. 72–76. DOI: 10.1038/s41550-019-0880-2. arXiv: 1904.06759 [astro-ph.HE].

[7] M. Prakash, I. Bombaci, M. Prakash, P. J. Ellis, J. M. Lattimer, and R. Knorren. "Composition and structure of protoneutron stars". In: *Physics Reports* 280.1 (1997), pp. 1–77. ISSN: 0370-1573. DOI: https://doi.org/10.1016/S0370-1573(96)00023-3. URL: https://www.sciencedirect.com/science/article/pii/S0370157396000233.

[8] S. Acharya et al. "p-p, p-Λ and Λ-Λ correlations studied via femtoscopy in pp reactions at $\sqrt{s}$ = 7 TeV". In: *Phys. Rev. C* 99.2 (2019), p. 024001. DOI: 10.1103/PhysRevC.99.024001. arXiv: 1805.12455 [nucl-ex].

[9] S. Acharya et al. "Search for a common baryon source in high-multiplicity pp collisions at the LHC". In: *Phys. Lett. B* 811 (2020), p. 135849. DOI: 10.1016/j.physletb.2020.135849. arXiv: 2004.08018 [nucl-ex].

[10] L. Fabbietti, V. Mantovani Sarti, and O. Vazquez Doce. "Study of the Strong Interaction Among Hadrons with Correlations at the LHC". In: *Ann. Rev. Nucl. Part. Sci.* 71 (2021), pp. 377–402. DOI: 10.1146/annurev-nucl-102419-034438. arXiv: 2012.09806 [nucl-ex].

[11] M. A. Lisa, S. Pratt, R. Soltz, and U. Wiedemann. "Femtoscopy in relativistic heavy ion collisions". In: *Ann. Rev. Nucl. Part. Sci.* 55 (2005), pp. 357–402. DOI: 10.1146/annurev.nucl.55.090704.151533. arXiv: nucl-ex/0505014.

[12] R. B. Wiringa, V. G. J. Stoks, and R. Schiavilla. "Accurate nucleon-nucleon potential with charge-independence breaking". In: *Phys. Rev. C* 51 (1 Jan. 1995), pp. 38–51. DOI: 10.1103/PhysRevC.51.38. URL: https://link.aps.org/doi/10.1103/PhysRevC.51.38.

[13] S. E. Koonin. "Proton pictures of high-energy nuclear collisions". In: *Physics Letters B* 70.1 (1977), pp. 43–47. ISSN: 0370-2693. DOI: https://doi.org/10.1016/0370-2693(77)90340-9. URL: https://www.sciencedirect.com/science/article/pii/0370269377903409.

[14] E. Lopienska. "The CERN accelerator complex, layout in 2022. Complexe des accélérateurs du CERN en janvier 2022". In: (2022). General Photo. URL: https://cds.cern.ch/record/2800984.

[15] K. Aamodt et al. "The ALICE experiment at the CERN LHC". In: *JINST* 3 (2008), S08002. DOI: 10.1088/1748-0221/3/08/S08002.

[16] S. Acharya et al. "ALICE upgrades during the LHC Long Shutdown 2". In: *JINST* 19.05 (2024), P05062. DOI: 10.1088/1748-0221/19/05/P05062. arXiv: 2302.01238 [physics.ins-det].

[17] J. Alme et al. "The ALICE TPC, a large 3-dimensional tracking device with fast readout for ultra-high multiplicity events". In: *Nucl. Instrum. Meth. A* 622 (2010), pp. 316–367. DOI: 10.1016/j.nima.2010.04.042. arXiv: 1001.1950 [physics.ins-det].

[18] P. Cortese. *ALICE Time-Of Flight system (TOF): addendum to the Technical Design Report*. Technical design report. ALICE. Geneva: CERN, 2002. URL: https://cds.cern.ch/record/545834.

[19] F. Carnesecchi. "Performance of the ALICE Time-Of-Flight detector at the LHC". In: *Journal of Instrumentation* 14.06 (Jan. 2019), p. C06023. DOI: 10.1088/1748-0221/14/06/C06023. URL: https://dx.doi.org/10.1088/1748-0221/14/06/C06023.

[20] Y. Melikyan. "Status and performance of the ALICE Fast Interaction Trigger". In: *PoS* ICHEP2024 (2025), p. 921. DOI: 10.22323/1.476.0921. arXiv: 2410.10617 [physics.ins-det].

[21] AliceO2Group. *O2 Physics Framework*. URL: https://github.com/AliceO2Group/O2Physics.

[22] P. Buncic, M. Krzewicki, and P. Vande Vyvre. *Technical Design Report for the Upgrade of the Online-Offline Computing System*. Tech. rep. 2015. URL: https://cds.cern.ch/record/2011297.

[23] R. Brun and F. Rademakers. "ROOT—An object oriented data analysis framework". In: *Nuclear Instruments and Methods in Physics Research Section A: Accelerators, Spectrometers, Detectors and Associated Equipment* 389.1-2 (1997), pp. 81–86.

[24] AliceO2Group. *O2 Physics Framework - FemtoDream*. URL: https://github.com/AliceO2Group/O2Physics/tree/master/PWGCF/FemtoDream.

[25] D. L. Mihaylov. "Analysis techniques for femtoscopy and correlation studies in small collision systems and their applications to the investigation of p–Λ and Λ–Λ interactions with ALICE". Other thesis. 2021-02-16, Munich, Tech. U., Feb. 2021.

[26] G. Mantzaridis. *First Multiplicity and m_T Dependent Measurement of the Size of the Emission Source in pp Collisions at $\sqrt{s}$ = 13.6 TeV with ALICE*. URL: https://www.das.ktas.ph.tum.de/DasDocs/Public/Master_Theses/GeorgiosMantzaridis_MasterThesis.pdf (visited on 06/20/2025).

[27] S. Acharya et al. "Common femtoscopic hadron-emission source in pp collisions at the LHC". In: *Eur. Phys. J. C* 85.2 (2025), p. 198. DOI: 10.1140/epjc/s10052-025-13793-y. arXiv: 2311.14527 [hep-ph].

[28] F. Becattini, P. Castorina, A. Milov, and H. Satz. "Predictions of hadron abundances in pp collisions at the LHC". In: *Journal of Physics G: Nuclear and Particle Physics* 38.2 (Jan. 2011), p. 025002. DOI: 10.1088/0954-3899/38/2/025002. URL: https://dx.doi.org/10.1088/0954-3899/38/2/025002.

[29] T. Pierog, I. Karpenko, J. M. Katzy, E. Yatsenko, and K. Werner. "EPOS LHC: Test of collective hadronization with data measured at the CERN Large Hadron Collider". In: *Phys. Rev. C* 92 (3 Sept. 2015), p. 034906. DOI: 10.1103/PhysRevC.92.034906. URL: https://link.aps.org/doi/10.1103/PhysRevC.92.034906.

[30] D. L. Mihaylov, V. Mantovani Sarti, O. W. Arnold, L. Fabbietti, B. Hohlweger, and A. M. Mathis. "A femtoscopic correlation analysis tool using the Schrödinger equation (CATS)". In: *The European Physical Journal C* 78.5 (May 2018). ISSN: 1434-6052. DOI: 10.1140/epjc/s10052-018-5859-0. URL: http://dx.doi.org/10.1140/epjc/s10052-018-5859-0.

[31] J. Haidenbauer, S. Petschauer, N. Kaiser, U.-G. Meißner, A. Nogga, and W. Weise. "Hyperon–nucleon interaction at next-to-leading order in chiral effective field theory". In: *Nuclear Physics A* 915 (2013), pp. 24–58. ISSN: 0375-9474. DOI: https://doi.org/10.1016/j.nuclphysa.2013.06.008. URL: https://www.sciencedirect.com/science/article/pii/S0375947413006167.

[32] R. V. Reid. "Local phenomenological nucleon-nucleon potentials". In: *Annals of Physics* 50.3 (1968), pp. 411–448. ISSN: 0003-4916. DOI: https://doi.org/10.1016/0003-4916(68)90126-7. URL: https://www.sciencedirect.com/science/article/pii/0003491668901267.

[33] V. G. J. Stoks, R. A. M. Klomp, C. P. F. Terheggen, and J. J. de Swart. "Construction of high-qualityNNpotential models". In: *Physical Review C* 49.6 (June 1994), pp. 2950–2962. ISSN: 1089-490X. DOI: 10.1103/physrevc.49.2950. URL: http://dx.doi.org/10.1103/PhysRevC.49.2950.